Graphene Electronics for High Frequency, Scalable Applications

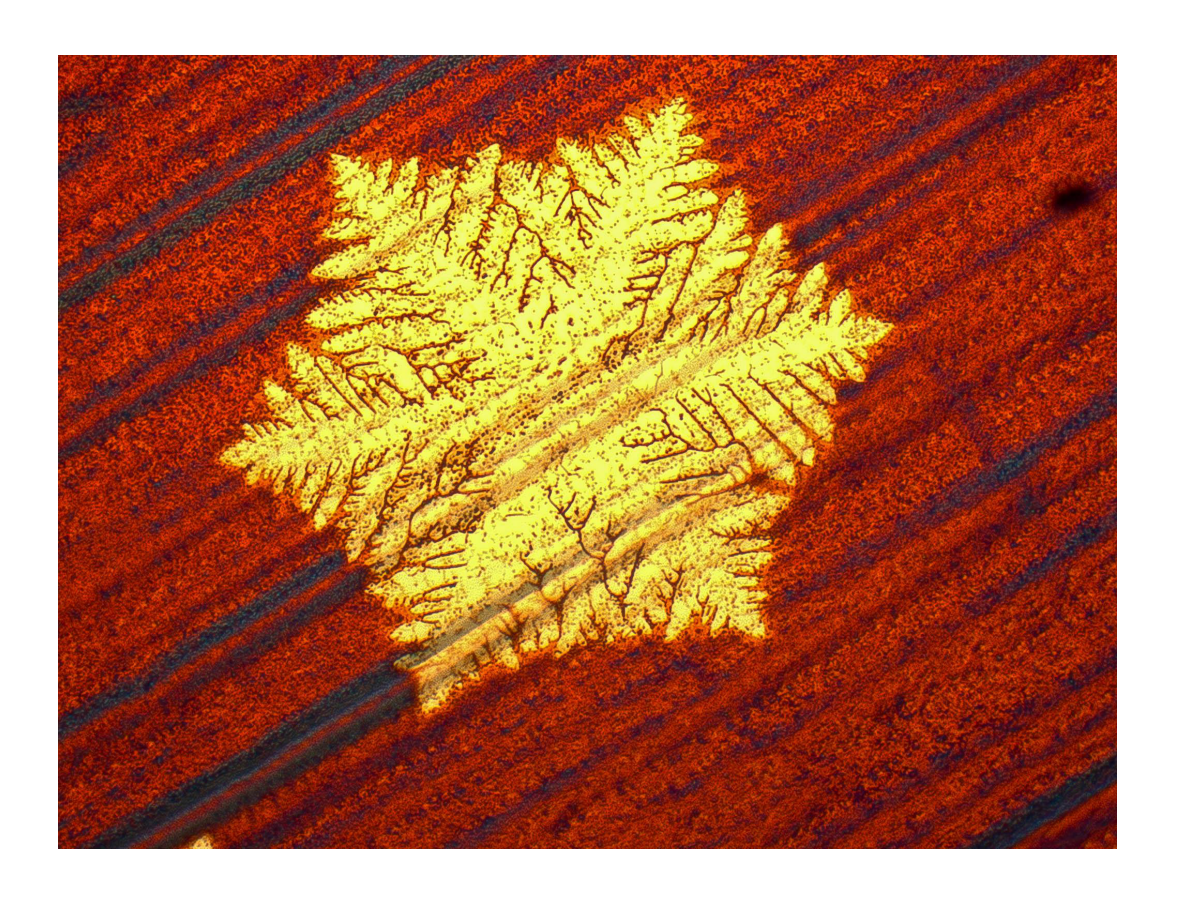
Mathieu Massicotte

Centre for the Physics of Materials
Department of Physics
McGill University
Montréal, Québec
Canada

A Thesis submitted to the Faculty of Graduate Studies and Research in partial fulfillment of the requirements for the degree of Master of Science

Le secret de la diversité réside dans l'action d'une force en un contexte de déséquilibre.

Hubert Reeves



Acknowledgments

This research project would not have been possible without the support of many people. First, I would like to express my gratitude to my supervisor, Prof. Michael Hilke for his invaluable assistance and for the the stimulating discussions, both scientific and non-scientific. Many thanks to Victor Yu and Eric Whiteway for sharing ideas and showing me the ins and outs of CVD graphene. Merci à Robert Gagnon et Richard Talbot pour leur support technique, en particulier pour la conception de la sonde micro-onde. Thanks to the staff of the McGill Nanotools Microfab for the many trainings. Thank you to my colleagues Alexandre Robitaille, Yuning Zhang, David Liu and Ben Harack. I also want to thank Dina Edelshtein for proofreading this thesis. Special thanks to my friends James Hedberg and Robert Welch for the great time in- and outside the lab. Finalement, je voudrais remercier mes parents, ma soeur et mes amis pour leur amour et amitié.

Abstract

The advent of large-scale graphene grown by chemical vapor deposition (CVD) offers a viable route towards high-frequency (HF) graphene-based analogue electronics. A significant challenge, however, is to synthesize and fabricate HF graphene-based devices with high carrier mobility. Here, we report our efforts to understand and control the CVD growth mechanism of graphene on copper, to characterize the synthesized film, and to fabricate graphene transistors and HF devices. In parallel, we describe the synthesis of large pristine dendritic graphene flakes that we name graphlocons. The electronic transport properties and magnetoresistance were assessed from 300 K to 100 mK and mobility up to $460 \text{ cm}^2/\text{Vs}$ was obtained with a residual charge carrier density of $1.6 \text{x} 10^{12} \text{ cm}^{-2}$. HF scattering parameters were measured from 0.04 to 20 GHz but they showed no dependence on temperature and magnetic field. This work provides a starting point for improving the structural and electronic properties of CVD graphene, and for exploring new phenomena in the GHz frequency range.

Résumé

L'avènement du graphène produit à grande-échelle par dépôt chimique en phase vapeur (CVD) ouvre une voie vers l'électronique haute-fréquence (HF) à base de graphène. Synthétiser du graphène possédant une grande mobilité des porteurs de charge et l'incorporer à des dispositifs HF constitue cependant un important défi. Nous présentons ici le fruit de nos efforts pour comprendre et contrôler le mécanisme de croissance CVD du graphène sur le cuivre, caractériser les films ainsi produits, et fabriquer des transistors et dispositifs HF à base de graphène. Parallèlement, nous décrivons la synthèse de grands flocons dendritiques de graphène que nous appelons graphlocons. Les propriétés électroniques et la magnetorésistance de ces échantillons ont été mesurées de 300 K à 100 mK et la mobilité la plus élevée obtenue est de 460 cm²/Vs avec une densité de porteurs de charge résiduels de 1.6x10¹² cm⁻². Les paramètres S de haute fréquence ont été mesurés de 0.04 à 20 GHz mais aucune dépendance en température ou champ magnétique n'a été observée. Ce travail fourni un point de départ pour améliorer les propriétés structurales et électroniques du graphène produit par CVD, et pour explorer de nouveaux phénomènes dans le domaine des GHz. .

Contents

	Ac	knowle	edgments	iv
	Ab	stract		\mathbf{v}
	Ré	sumé		vi
-				-1
T		roduct		1
	1.1		ical summary	1
	1.2	Motiva	ation and Thesis Organization	3
2	Εle	ectroni	c Properties of Graphene	5
	2.1	Atomi	c and Electronic Band Structure	5
	2.2	Transp	port Properties	8
		2.2.1	Charge Carrier Density	8
		2.2.2	Transport equation	9
		2.2.3	Mobility	10
	2.3	Magne	etotransport	12
		2.3.1	Hall Effect	12
		2.3.2	Weak Localization	14
	2.4	Non-li	near High-frequency Response	15
ય	Ch	emical	Vapor Deposition Growth of Graphene on Copper	18
J	3.1		The Mechanism	19
	9.1	3.1.1	Thermodynamics	20
		3.1.2	Kinetics	20
	3.2	_	imental method	22
	9.2	3.2.1	CVD System	22
		3.2.1		23
	3.3		Growth Procedure	25 25
	0.0	3.3.1	Effect of the Gas Ratio	26
		3.3.2	Effect of the Substrate Morphology	27
		3.3.3	Effect of the Gas Kinetics	28
	3.4		fer Method	30
	0.4	Transi	IGI 1VIGUIIUU	UG

viii Contents

4 Cl	haracte	rization and Device Fabrication	34
4.1	Chara	cterization	34
	4.1.1	Raman Spectroscopy	34
	4.1.2	Spectrophotometry	36
	4.1.3	Transmission Electron Microscopy	38
4.2	Fabric	ation of Graphene Field Effect Transistors	41
	4.2.1	Graphene Hall Bar	41
	4.2.2	Graphlocon Transistors	48
	4.2.3	Wire bonding	49
5 Tr	ranspor	t Measurements	51
5.1	Exper	imental method	52
	5.1.1	Measurement setup	52
	5.1.2	Measurement Techniques	53
5.2	Result	s and Discussion	54
	5.2.1	Field Effect Mobility	54
	5.2.2	Magnetotransport	59
6 H	igh Fred	quency Measurements	64
6.1	Exper	imental Setup	65
	6.1.1	4-Kelvin Microwave Probe	65
	6.1.2	High Frequency Graphene Device	67
6.2	Result	s and Discussion	73
	6.2.1	High Frequency Transmission Through Graphene	73
	6.2.2	Frequency-dependent DC Resistance	75
	6.2.3	Effect of Magnetic Field at Low Temperature	78
7 C	onclusio	on	81
Re	eference	es	83

List of Figures

1.1	Scientific publications on carbon allotropes throughout modern history	2
2.1	Direct and reciprocal lattice of graphene	6
2.2	Electronic band structure of graphene	7
2.3	Magnetotransport measurement	13
2.4	Comparison between the weak anti-localization and weak localization	
	regimes	15
2.5	Survey of plasmon, MP and EMP in graphene	17
3.1	Thermodynamic and kinetic models for the CVD-growth of graphene	
	on Cu	21
3.2	Schematic of the CVD system	24
3.3	Typical CVD growth of graphene on copper	26
3.4	Graphene on Cu at various gas ratios χ	28
3.5	Influence of the substrate topography	29
3.6	Growth of graphlocons in a copper enclosure	31
3.7	Schematic of the graphene transfer	32
3.8	Graphlocon and a graphene layer transferred on $\mathrm{SiO}_2/\mathrm{Si}$	33
4.1	Raman spectroscopy in graphene	36
4.2	Characterization of graphene by broadband spectrophotometry	38
4.3	TEM-XRD-EDS analysis	40
4.4	Schematic of the Hall bar fabrication process	42
4.5	Comparison between photolithography	45
4.6	Graphene etching by RIE	46
4.7	Graphene lift-off and laser patterning	48
4.8	Fabrication process of two graphlocon transistors	50
4.9	Wire-bonded graphene device	50
5.1	Schematic of the electrical measurement setup for a Hall bar device .	53
5.2	Measurement of the gate-dependent sheet resistance at various tem-	
	peratures	55

x List of Figures

5.3	Measurement of the gate-dependent sheet resistance at various tem-	
	peratures	56
5.4	Fit of gate-dependent 2-terminal resistance for the Hall bar device and	
	the graphlocon transistor	59
5.5	Magnetoresistance of the Hall bar at 100 mK	61
5.6	Normalized MR of sub-micron Hall bar and a 1.5 mm size graphene	
	sample	62
6.1	Schematic of the high frequency measurement setup using the 4-K	
	microwave probe	66
6.2	Schematic of the 4-K microwave probe	68
6.3	Schematic of a coplanar waveguide as simulated by AppCAD	69
6.4	Schematic of a typical high frequency graphene device	70
6.5	Pictures of the CPW graphene device	71
6.6	Characterization of the probe	72
6.7	Contribution of graphene to the high frequency transmission spectrum	74
6.8	Measured and calculated microwave transmission through graphene .	75
6.9	Frequency dependence of the 4T DC resistance of graphene at 77 and	
	300 K	77
6.10	Microwave heating of graphene	78
6.11	Microwave measurements at 100 mK	80

Introduction

1.1 Historical summary

From polymer chains to human beings, everything that grows is made out of carbon atoms. These building blocks of nature possess unique properties that we are continuing to discover and use for our own needs. Among the carbon allotropes, three-dimensional (3D) materials such as graphite and diamond have been known for millennia. During the four last decades an increasing amount of effort has been devoted to study lower-dimensional carbon nanostructures. Fig. 1.1 shows that besides a few publications on graphite intercalation compounds (GICs), the field of carbon nanostructures was practically non-existent before the late 1980s. Many publications followed the discovery of zero-dimensional (0D) fullerenes in 1985, which was rapidly followed by that of one-dimensional (1D) carbon nanotube (CNT) in 1992 [1]. At that time, the two-dimensional (2D), one-atom thick carbon nanostructure known as graphene was not a very popular topic. Yet, the concept of graphene had been discussed since at least 1947, when Wallace [2] published his work on the electronic band structure of graphene as an approximation for the one of graphite. Later in 1962, Boehm reported the first observation of single and few-layer graphene and coined the term as a combination of graphite and the suffix ene [3]. Because the characterization tools at the time were rudimentary, Boehms research did not lead immediately to further investigation. The study of graphene was partly deterred by Mermin-Wagner's theorem which states that there should be no long-range order in two-dimensions [4]. $oldsymbol{1}$ Introduction

It was assumed by many that 2D crystals were not thermodynamically stable without the presence of ripples and dislocations [5].

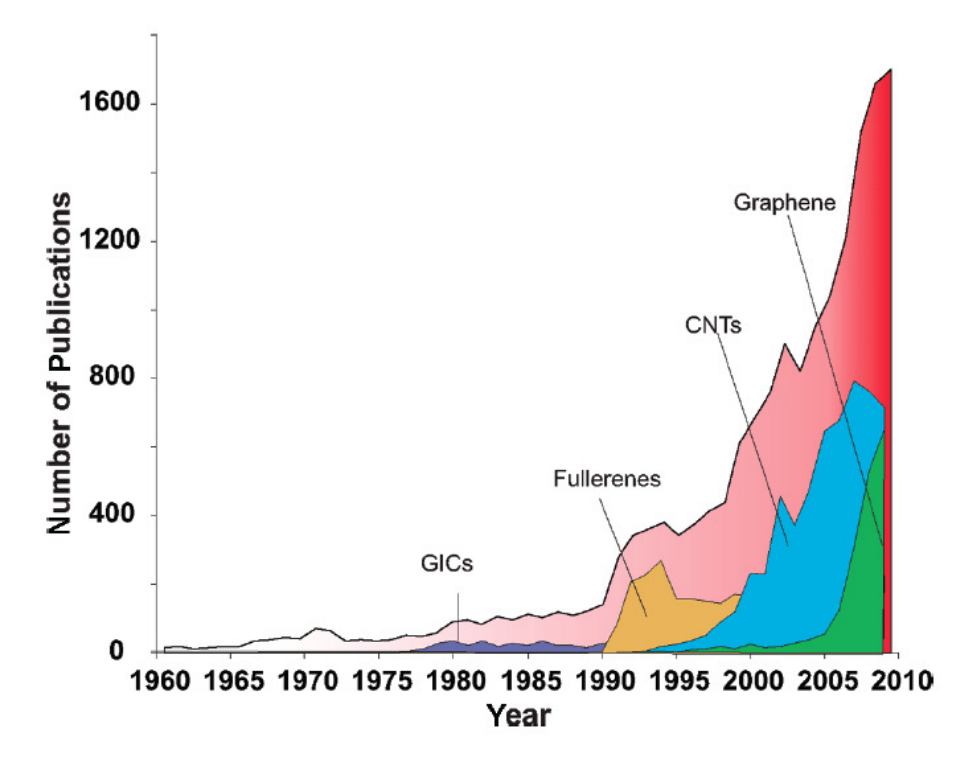


Figure 1.1: Scientific publications on carbon allotropes throughout modern history. Reproduced from [1].

This situation changed drastically in 2004 when Geim and Novoselov isolated micrometer-size graphene flakes and probed their extraordinary electrical properties [6]. Their crafty technique consisted of using adhesive tape to mechanically exfoliate a one-atom thick carbon flake from bulk graphite and transfer it to a substrate via Van der Waals forces. The simplicity of this method combined with ground-breaking physical measurements [6, 7] attracted a great deal of attention, whereupon the number of publications on graphene exploded (Fig. 1.1). Geim and Novoselov were awarded the 2010 Nobel prize in physics for their seminal work, and since then the interest for this remarkable material shows no sign of abating. The high intrinsic carrier mobility [8, 9, 10], superior thermal conductivity [11], low optical absorption [12], and great tensile strength [13] make graphene a promising material for numerous applica-

tions in electronics [14, 15, 16, 17, 18], optoelectronics [19, 20, 21, 22], chemical and biological sensing [23, 24]. However, in order for graphene technologies to be viable, methods to mass-produce high-quality graphene on large-scale are crucial. Recently, many synthesis methods have been proposed and developed including thermal decomposition of SiC [25, 26], reduction of graphene oxide [27, 28] and chemical vapor deposition (CVD) on transition metals [22, 29, 30, 31, 32, 33, 34, 35, 36]. Among them, the growth of graphene by CVD on copper has emerged as one of the most promising due to the scalability, affordability, compatibility with silicon technology and quality of the synthesized film. However, the electronic properties of CVD-grown graphene still do not match up to those of exfoliated graphene.

1.2 Motivation and Thesis Organization

On the road to practical graphene electronics, many scientific and technical challenges must be addressed. From a physics point of view, understanding the growth mechanism of CVD graphene, the mechanisms limiting the mobility of charge carriers in this material and its intrinsic response to high frequency (HF) are major drives in the graphene research community. On the technical side, synthesizing reproducible high-quality graphene film, transferring it onto insulating substrates and fabricating electrical devices without lowering the film quality are the main challenges faced by scientists and industries. In order to tackle these problems, a logical approach consists in studying the microstructure-property relationship in graphene. In practical terms, this entails investigating and controlling the growth of CVD graphene, developing clean device fabrication procedures and assessing the film quality with standard characterization instruments as well as electronic transport and high frequency measurements, from high to low temperature.

This thesis presents our endeavour to improve the quality of graphene grown by CVD on Cu, as well as our study of its transport and high frequency properties. In the next chapter we provide a theoretical and experimental background on the electric and magnetic properties of graphene. In Chapter 3 we briefly review the

 $oldsymbol{1}$ Introduction

growth mechanism of CVD-graphene, describe our synthesis procedure and discuss some issues and results. In Chapter 4, we characterize our samples using standard instruments and we detail the fabrication process for making graphene-based electrical devices. Chapter 5 contains the results and discussion of our study on electronic transport and magnetotransport. Chapter 6 is dedicated to the method and results of our investigation on graphene's high frequency response.

Electronic Properties of Graphene

Since Geim's and Novoselov's seminal work [6], much ink has been spilled about graphenes unique electronic properties. In this chapter, we review the main concepts and theories which are relevant to understanding the experimental results presented in the following chapters.

2.1 Atomic and Electronic Band Structure

Graphene is a monolayer of sp^2 -bonded carbon atoms arranged in a honeycomb crystal lattice (Fig. 2.1). Each atom shares an in-plan σ bond with its three nearest neighbours, which are separated by a=1.42 Å. The remaining valence electron forms an out-of-plan π -bond which is delocalized and gives rise to the π and π^* bands. These bands are respectively the so-called valence and conduction bands and are responsible for the exceptional electronic properties of graphene.

The hexagonal lattice contains two carbon atoms per unit cell, each forming a triangular sublattice as depicted in Fig. 2.1a. In the reciprocal space, the corresponding Brillouin zone is a hexagonal cell with high symmetry points identified by the letters Γ , M, K and K'(Fig. 2.1b). For reasons that will become clearer later, the K and K'are known as the Dirac points and they play a fundamental role in the peculiar electronic transport of graphene. The importance of the Dirac points in graphene can easily be compared to that of the Γ point in direct band-gap semiconductors. It is worth noting that the non-equivalence of the K and K'points gives rise to a valley degeneracy of $g_v = 2$.

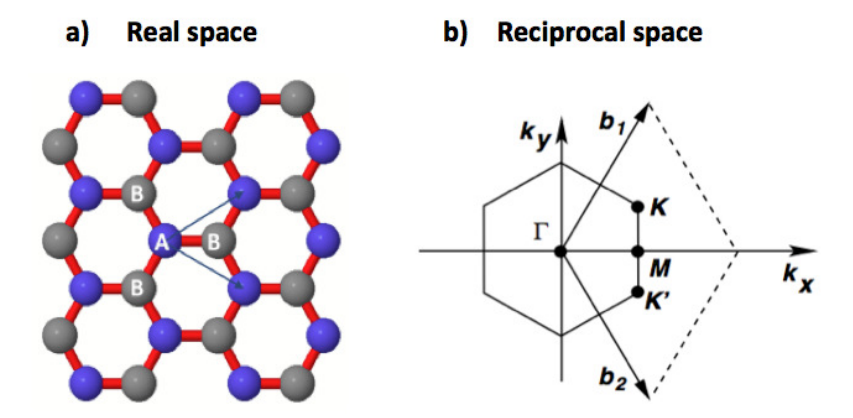


Figure 2.1: Direct and reciprocal lattice of graphene. a) Triangular sublattices (A and B) in real space. Reproduced from [37]. b) First Brillouin zone with high symmetry points. Reproduced from [38].

To calculate the band structure of graphene, Wallace [2] employed a tight-binding approximation which assumes that electrons can tunnel or "hop" only to one of the first nearest-neighbors. Examining Fig. 2.1a, this means that an electron on a carbon atom of the sublattice A can only tunnel to an atom of the sublattice B, and viceversa. The dispersion relation of graphene using this model has the form

$$E(\vec{\mathbf{k}}) = \pm \Delta \sqrt{3 + 2\cos(\sqrt{3}ak_x) + 4\cos(\frac{\sqrt{3}}{2}ak_x)\cos(\frac{3}{2}ak_y)}$$
 (2.1)

where $\vec{\mathbf{k}}$ is the two-dimensional wave vector and $\Delta \approx 2.7$ eV is the nearest neighbor hopping energy. The band structure given by Eq. (2.1) is plotted in Fig. 2.2a, where the minus sign (lower band) and plus sign (upper band) correspond to the valence π -band and conduction π *-band, respectively. These bands form conical structures at the 6 Dirac points (K and K'), their tips meeting at E = 0 (Fig. 2.2b). Most interestingly, the energy goes linearly with small perturbations $|\vec{\mathbf{q}}| = |\vec{\mathbf{k}} - \mathbf{K}| \ll |\mathbf{K}|$ around these 6 points. Using Maclaurin's expansion on Eq. (2.1), the dispersion relation can be written $E(\vec{\mathbf{q}}) = \pm \hbar \nu_F |\vec{\mathbf{q}}|$, where $\nu_F = \frac{3\Delta a}{2\hbar} \approx 10^6$ m/s is the Fermi velocity. This feature is essentially what makes the electronic properties of graphene so unique. Indeed, charge carriers in typical semiconductors are usually described by a non-relativistic, parabolic Schrödinger equation. In graphene, they are best

described by a Dirac-like Hamiltonian of the form:

$$\hat{H} = \hbar \nu_F \begin{pmatrix} 0 & q_x - iq_y \\ q_x + iq_y & 0 \end{pmatrix} = \hbar \nu_F \vec{\sigma} \cdot \vec{q}$$
 (2.2)

where $\vec{\sigma}$ are the 2D Pauli matrices. By interchanging the Fermi velocity ν_F with the speed of light c, Eq. (2.2) is identical to the Dirac equation with massless relativistic fermions. Strictly speaking, since ν_F is approximately $1/300^{th}$ of the speed of light in vacuum, the motion of electrons in graphene is not relativistic but it obeys the same Hamiltonian as massless relativistic particles. This similarity attracted a huge amount of attention coming from both theoreticians and experimentalists [5]. The fact that graphene has a gapless band structure also generated a lot of interest because it allows to continuously tune the type of charge carriers between holes and electrons [6, 39]. As we will discuss in the following section, this can be done simply by moving the Fermi level (E_F) up or down with a gate voltage. For common semiconductors, the charge carriers can only be changed significantly by chemical doping.

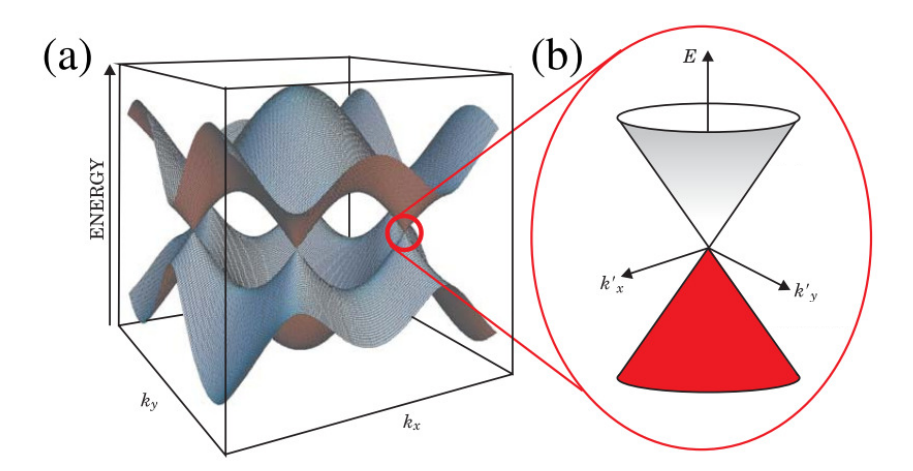


Figure 2.2: Electronic band structure of graphene a) as calculated by Eq. (2.1) and b) enlargement of the conical band structure close to K or K'point. Reproduced from [40].

2.2 Transport Properties

2.2.1 Charge Carrier Density

A direct consequence of the linear dispersion relation of graphene is that the density of states D is proportional to the energy

$$D(E) = \frac{g_s g_v}{2\pi (\hbar \nu_F)^2} |E| \tag{2.3}$$

where $g_s = 2$ is the spin degeneracy. The integral of the density of states up to the Fermi level yields the charge carrier density

$$n(E_F) = \frac{E_F^2}{\pi (\hbar \nu_F)^2}$$
 (2.4)

This relationship implies that varying the position of the Fermi energy correspondingly changes the carrier density. For $E_F > 0$, the charge carriers are electrons whereas for for $E_F < 0$, they are holes. The Fermi energy, and hence the carrier density, can be modulated by applying an external electric field. To do so, graphene is usually separated from a conductive gate by a thin dielectric, thus forming a field-effect device. Applying a voltage V_G between the gate electrode and the graphene layer induces a charge density

$$n_{VG} = p - n = -C_{ox}V_{G0}/e (2.5)$$

where p and n are hole and electron density, C_{ox} is the capacitance per unit area of the dielectric, e is the elementary charge and $V_{G0} = V_G - V_0$ is the difference between the applied gate voltage V_G and the minimum conductivity (Dirac point) voltage V_0 .

According to Eq. (2.4), the charge carrier density n should theoretically vanish at the Dirac point ($E_F = 0$). However, in practice, the minimum charge density is limited by thermally generated carriers (n_{th}) and electrostatic spatial inhomogeneity (n^*) [41, 42]. At $E_F = 0$ and T = 300 K, the thermal carrier density is $n_{th} \approx 9 \times 10^{10}$ cm⁻² [43]. The latter type of charge carriers account for the spatial charge inhomogeneity (puddles) caused by charged impurities on the graphene layer and at

the graphene/substrate interface [44]. These charged impurities also act like dopants and are responsible for the shift of the Fermi level away from the Dirac point. In contrast, for a pristine graphene layer without charged impurities, no shift would occur and $V_0 = 0$ V. Finally, according to Drogan *et al.* [42], the electron and hole density can be expressed approximately as follows:

$$n, p \approx \frac{1}{2} [\pm n_{VG} + \sqrt{n_{VG}^2 + 4n_0^2}]$$
 (2.6)

where $n_0 = \sqrt{(n^*/2)^2 + n_{th}^2}$ is the residual carrier density at the Dirac point.

2.2.2 Transport equation

(The two following subsections are adapted from the section of a published review article [37] that I cowrote in the course of my Master's degree.)

In contrast with the ideal, theoretical graphene, experimental graphene contains defects [45] and impurities [46, 44], grain boundaries [47], interacts with the substrate [10], has edges and ripples [48] and is affected by phonons [49]. These perturbations alter the electronic properties of a perfect graphene sheet first by introducing spatial inhomogeneities in the carrier density and, second, by acting as scattering sources which reduce the electron mean free path [43].

The impact of these perturbations on the transport properties has been subjected to intensive and ongoing investigations, on both the theoretical and experimental sides. From a theoretical point of view, two transport regimes are often considered depending on the mean free path length l and the graphene length L. When l > L, transport is said to be ballistic since carriers can travel at ν_F from one electrode to the other without scattering. On the other hand, when l < L, carriers undergo elastic and inelastic collisions and transport enters the diffusive regime. In this case, transport can be described by the semiclassical Boltzmann transport theory [40] and the conductivity σ is expressed by the Einstein relation:

$$\sigma = \frac{e^2 \nu_F^2}{2} D(E_F) \tau(E_F) \tag{2.7}$$

where the transport scattering time (or relaxation time) τ is related to the carrier mean free path by $l = \nu_F \tau$. Using Eq. (2.3) and Eq. (2.4), the following expression for the dependence of σ on the n and τ is obtained:

$$\sigma = \frac{e^2 \nu_F \tau}{\hbar} \sqrt{\frac{n}{\pi}} \tag{2.8}$$

This equation describes the diffusive motion of carriers scattering independently off various impurities. The relaxation time depends on the scattering mechanism dominating the carrier transport or a combination thereof.

In this thesis, we focus primarily on Coulomb scattering which stems from longrange variations in the electrostatic potential caused by the presence of charged impurities close to the graphene sheet. Assuming random distribution of charged impurities with density n_{imp} and employing a semiclassical approach, it was predicted [50] that the charged-impurity scattering time is proportional to \sqrt{n}/n_{imp} . At high carrier density $(n > n_0)$ the conductivity given by Eq. (2.8) becomes:

$$\sigma = \frac{Ce^2}{h} \frac{n}{n_{imp}} \tag{2.9}$$

where C is a dimensionless parameter related to the scattering strength. Adam et al. [50] found a theoretical relationship between the residual carrier density n_0 and the charged impurity density n_{imp} for graphene on silicon dioxide (SiO₂) substrate. For dirty graphene samples $(n_{imp} \sim 4 \times 10^{12} \text{cm}^{-2})$, their model predicts that $n_0 \approx 0.2 n_{imp}$. Considering the random phase approximation and the dielectric screening from the SiO₂ substrate, it was predicted that $C \approx 20$. This result was confirmed experimentally [46, 51].

2.2.3 Mobility

In a graphene electronic device, all of the scattering mechanisms mentioned above come into play and limit the mobility of the charge carriers. The latter is related to the conductivity and charge carrier density as

$$\mu = \frac{\sigma}{en} \tag{2.10}$$

From a technological point of view, determining the exact nature of the scattering that limits the mobility is essential in order to develop high-speed electronic devices. To do so, one must also take into account the effect of the underlying substrate on the electronic transport. Chen et al. [10] showed that for exfoliated graphene on SiO₂ at room temperature, surface polar phonons (SPP) of the SiO₂ and charge impurities are the two main factors detrimental to the mobility. To improve the mobility, one approach consists of etching the underlying SiO₂ substrate to fabricate a suspended graphene device. Mobility as high as 200 000 cm²/Vs can be obtained in these devices using exfoliated graphene [8]. Although suspended graphene shows impressive transport properties, this geometry imposes evident constraints on the device architecture. To overcome this problem, boron nitride (BN) was proposed as a substrate [52] and mobility about three times higher than that of exfoliated graphene on SiO₂ were obtained. However, graphene/BN devices are difficult to fabricate and are thus not ideal for industrial applications.

Currently, large area graphene synthesized by CVD or thermal segregation is the most promising material for technological applications since it can be produced on a wafer scale [30, 29]. Depending on the technique, large scale graphene typically shows mobilities lower than 5 000 cm²/Vs on SiO₂ [53] and 13 000 m²/Vs on BN [54]. The scattering mechanisms responsible for this reduced mobility are still under investigation. Preliminary studies suggested that grain boundaries [55, 47], roughness of the growth substrate [56, 57], and chemical impurities introduced and defect created during the graphene transfer [58, 59, 60] could be the main factors limiting the mobility. Table 2.1 compares the carrier mobility of graphene produced by different techniques and on different substrates.

Substrate	Production	μ	Ref.
	technique	$(\times 10^3 \text{ cm}^2/\text{Vs})$	
-SiO ₂ /Si	Exfoliation	10-15	a
Boron nitride	Exfoliation	25-140	b
Suspended	Exfoliation	120-200	c
SiC	Thermal-SiC	1-5	d
$\mathrm{SiO}_{2}/\mathrm{Si}$	Ni-CVD	1-5	e
$\mathrm{SiO}_2/\mathrm{Si}$	Cu-CVD	1-16	f
Boron nitride	Cu-CVD	8-13	g

Table 2.1: Mobility range (μ) of graphene produced by different techniques and deposited on different substrates. a: [6], b: [52], c: [8], d: [26], e: [29], f: [31], g: [54]

2.3 Magnetotransport

Measuring the tensorial resistivity $\rho = \sigma^{-1}$ of materials in an external perpendicular magnetic field (B) also provides a lot of insight into its electronic properties. The longitudinal resistance R_{XX} and Hall resistance R_{XY} are defined as the ratio of the longitudinal voltage V_{XX} and transverse voltage V_{XY} to the current, respectively (Fig. 2.3a). For well-defined sample geometries, the longitudinal resistivity ρ_{XX} is simply obtained by multiplying R_{XX} by the aspect ratio W/L of the sample, where W is its width and L is its length. It is worth noting that the Hall resistivity ρ_{XY} is identical to R_{XY} and that the sheet resistance R_S (defined as ρ /thickness for 3D materials) is usually considered equivalent to ρ for graphene.

2.3.1 Hall Effect

Applying a weak B-field allows to determine the type of charge carriers (holes or electrons) and to independently and directly measure the Hall charge carrier density n_H , thus avoiding the need for a model for $n(V_G)$ as the one discussed above. According to the Drude model [61], R_{XY} is related to the B-field by $R_{XY} = R_H B$, where $R_H = 1/en_H$ is the Hall coefficient. Novoselov *et al.* [7] measured the linear relation between $1/R_H$ and V_{G0} (Fig. 2.3b). This measurement also proves that charge

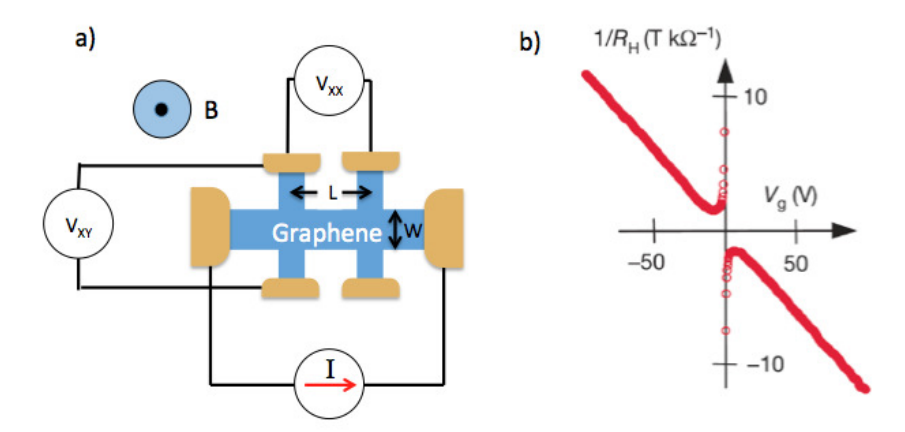


Figure 2.3: Magnetotransport measurement. a) Schematic of a Hall bar configuration and b) gate-voltage dependence of the conventional Hall resistance in graphene at B=2T (Reproduced from [7].

carriers are holes for $V_{G0} < 0$, and electron for $V_{G0} > 0$.

As the magnetic field increases and the temperature decreases, the quantum nature of the charge carriers emerges and the Hall resistance becomes quantized. This quantization is due to the formation of discrete and highly degenerate energy levels called Landau levels. It can be shown that charge carriers in the first Landau level have a cyclotron resonance frequency of $\omega_c = \operatorname{sgn}(n_L)\nu_F\sqrt{2e\hbar B|n_L|}$, with $n_L = 0,\pm 1,\pm 2,...$ [39] In their seminal article [7], Geim and Novoselov showed that these carriers have a cyclotron mass defined as

$$m_c = E/\nu_F^2 = \sqrt{h^2 n/4\pi \nu_F^2}$$
 (2.11)

To enter the regime where the quantum Hall effect (QHE) is observable, two main conditions must be satisfied. Firstly, the spacing between the Landau levels ($\hbar\omega_c$ between $n_L = 0$ and ± 1) must be much larger than the thermal energy k_BT . A simple way this can be achieved is by cooling down the material. Secondly, the charge carriers in cyclotron motion need to complete a few orbits before losing their momentum due to scattering: $\tau \gg \omega_c^{-1}$. This criterion can be rewritten $\mu \gg B^{-1}$, which means that a dirty and low mobility sample requires higher B-field in order to

exhibit QHE. Since the mobility in exfoliated graphene is usually 2 or 3 times higher than that in large area graphene (Table 2.1), it is no surprise that QHE appears typically at $B\sim3$ T [7] for the former and ~8 T [29] for the latter.

2.3.2 Weak Localization

Besides QHE, one can also investigate the quantum properties of charge carriers in low-mobility samples by studying the variation of resistivity in the presence of a low B-field. This effect, called weak localization (WL), can be observed when the transport is in the diffusive regime and the phase-relaxation time τ_{ϕ} is of the same order of magnitude or larger than the scattering time (or momentum relation time) τ . The latter requirement can be satisfied at low temperature since τ_{ϕ} increases as temperature decreases. In these conditions, carriers behave like quantum mechanical waves which scatter off many impurities without loosing there phase. The interference resulting from these scattering events leads to an increase in resistivity ρ_{XX} compared to the classical Drude model; this is the weak localization regime. By applying a small B-field, charge carriers acquire an additional phase as they move. This suppresses the interference effect and thus reduces the electrical resistance.

McCann *et al.* [62] have developed the leading theory of WL in graphene and their model predicts the following magnetoresistivity:

$$\rho(B) = \rho(0) - \frac{\rho^2 e^2}{\pi h} (F(B_\phi) - F(B_\phi + 2B_i) - 2F(B_\phi + B_i + B_\star))$$
 (2.12)

where $F(z) = \psi(0.5 + z/B) - \ln(z/B)$, ψ is the digamma function and the values of B_{σ} (with $\sigma = \phi, i, \star$) are related to their respective scattering time τ_{σ} by $B_{\sigma}^{-1} = 2e\nu_F^2\tau\tau_{\sigma}/\hbar$. The intravalley elastic scattering time τ_{\star} is mainly influenced by the presence of short range scatterers, like defects and cracks, who do not conserve the valley isospin. τ_i represents the intervalley elastic scattering time, which is limited mainly by long range scatterers (e.g. Coulomb) who conserve the valley isospin. According to McCann's model, we can distinguish two localization regimes depending on the value of τ_{\star}/τ_i . If this ratio is small, carriers are weakly localized

and the magnetoresistance decreases by applying a B-field. At larger ratio τ_{\star}/τ_{i} , this effect reverses and the so-called weak anti-localization (WAL) occurs. This crossover between WL and WAL is depicted in Fig. 2.4.

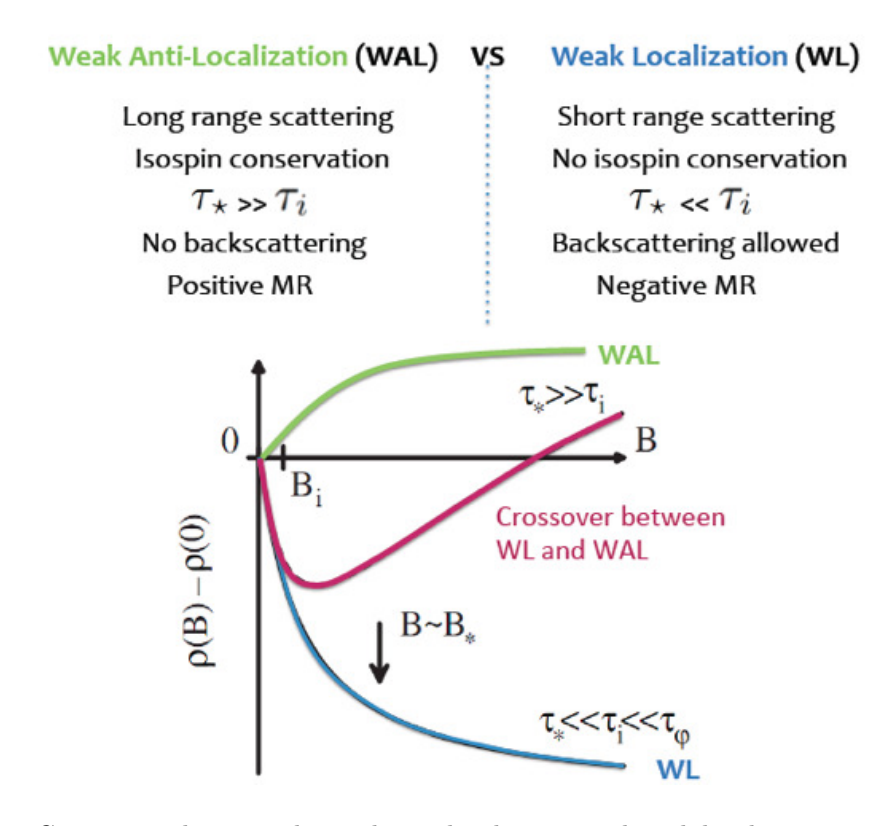


Figure 2.4: Comparison between the weak anti-localization and weak localization regimes. (Inspired by [62])

2.4 Non-linear High-frequency Response

Applying an external, time-dependent electromagnetic (EM) field to a material can give rise to a wealth of electronic phenomena, from the basic joule heating to complex non-linear effects. In the following section, we briefly review the possible plasmonic effects that can be observed in graphene and discuss the conditions that need to be fulfilled in order to do so.

Plasmons are collective oscillations of the charge carrier density arising from the interparticle Coulomb interaction [61]. To propagate without damping, the EM field must have a frequency ω much larger than the scattering rate: $\omega \gg 1/\tau$. Using the

classical law of motion, it can be shown that these plasma waves have approximately the following dispersion relation [63]:

$$\omega_p^2(q) = \frac{2\pi ne^2}{m\kappa}|q| \tag{2.13}$$

where ω_p is the plasma frequency, κ the dielectric constant and m the carrier mass. In graphene, this mass corresponds to the cyclotron mass defined in Eq. (2.11) [40]. For a finite size system of length L, the wavevector is $q = 2\pi/L$.

In the presence of a B-field, the plasmon oscillations couple with the cyclotron motion of the charge carriers and the dispersion relation becomes $\omega_{mp}^2 = \omega_p^2 + \omega_c^2$. These excitations are called magnetoplasmons (MP). Like in the case of plamons, the damping of MPs is small only when $\omega_{mp} \gg 1/\tau$.

This situation contrasts the one for edge magnetoplasmon (EMP), which can be described as MPs propagating along the edge of a two-dimensional electron system. A rough estimate of the EMP frequency can be obtained using Ohms law. This model yields the following dispersion relation

$$\omega_{emp}^2 = \frac{2\pi ne}{\kappa LB} \tag{2.14}$$

It turns out that the EMP damping can be very small, even if $\omega_{emp} \ll 1/\tau$, when the magnetic field is strong enough to achieve $\rho_{XY} \gg \rho_{XX}$. Fig. 2.5 displays the carrier density dependence of the plasmon, MP and EMP frequency $f = 2\pi\omega$ for L =1 cm (lower curve) and L=1 μ m (upper curve) for B=8 T. This figure will be particularly useful when analyzing the results of our investigation at high frequency.

On the experimental side, very few observations of the plasmon in graphene have been made. They have been investigated by infrared spectroscopy [64, 65] and, very recently, two studies simultaneously reported the direct observation of propagating plasmon using near-field scattering microscopy [66, 67]. Until very recently, neither MP and EMP had been detected in graphene. In fact, observations of such phenomena were reported as we were writing this thesis [68, 69, 70]. In Fig. 2.5, we indicate the charge carrier density and frequency range for which plasmonic effects were observed.

In this thesis, we aim at detecting these effects in the microwave frequency range where EMPs can be created.

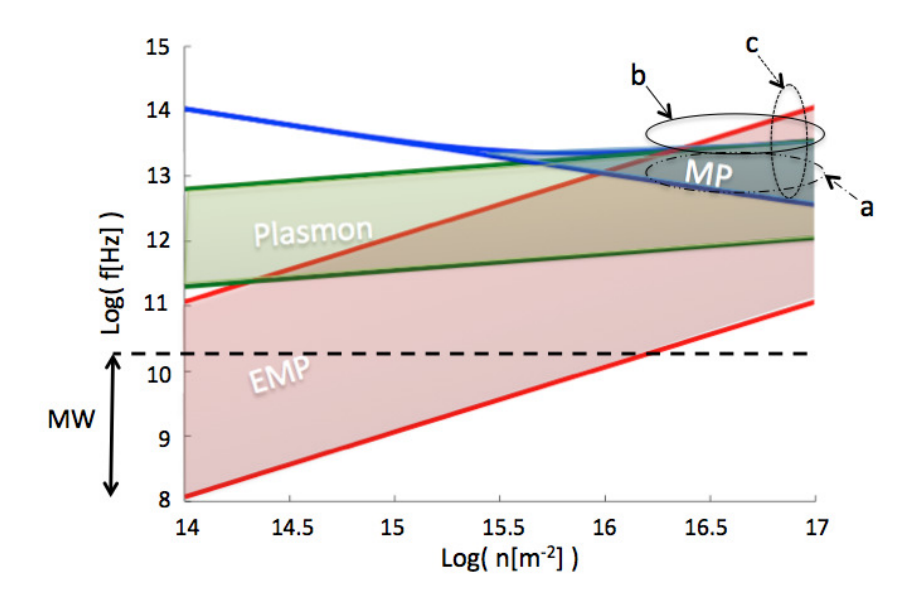


Figure 2.5: Survey of plasmon (green), MP (blue) and EMP (red) in graphene as a function of charge carrier density n. For each plasmonic effect, the colored region corresponds to the plasmon frequency range for sample of length L=1 μm (upper curve) to L=1 cm (lower curve). Regions where plasmons were observed by [64],[66] and [69] are indicated by circles a, b and c, respectively.

Chemical Vapor Deposition Growth of Graphene on Copper

Half a decade ago, growing large-sized graphene was considered a baffling problem. In his 2009 review article on graphene [71], Geim optimistically wrote: "Whichever way one now looks at the prospects for graphene production in bulk and wafer-scale quantities, those challenges that looked so daunting just two years ago have suddenly shrunk, if not evaporated, thanks to the recent advances in growth, transfer, and cleavage techniques". At that time, the main methods of growing large-scale graphene were thermal decomposition of silicon carbide (SiC) [26, 25] and chemical vapour deposition (CVD) on nickel [29, 72]. During the last three years, multiple methods to grow large-sized graphene layers have been proposed and demonstrated, the vast majority being CVD variants. Different transition metals such as copper [22, 30, 31, 32], iron [73], Iridium [73] and platinum [74] were employed as catalytic substrates. The carbon sources also varied from gases such as methane [22, 30, 31] and acetylene [75], to solids such as PMMA [76], sucrose [77] and even dog feces [78].

In this chapter, we focus on the more widely spread method of CVD on Cu with methane, which we employed to grow the graphene for our electrical devices. Despite the many studies on this synthesis technique, some aspects of the growth mechanism, such as the nucleation and kinetics, still remain obscure. In the following, we will review the latest advances on this topic, describe our experimental procedure and interpret our results in light of the current understanding. The technique used to transfer graphene layers from metallic to insulating substrates will be detailed.

3.1 Growth Mechanism

In general terms, chemical vapour deposition is a process where a volatile compound of a material to be deposited chemically reacts with other gases to form a thin solid film on a suitably placed substrate [79]. In the case that interests us, the precursors are methane (CH₄) and hydrogen (H₂) and their chemical reactions, which are promoted by heat, result in the deposition of thin carbon layer on the copper substrate.

Transition metals like copper are well known for their catalytic power which stems from their capacity to form bonds with their partially filled d and s-orbitals and the reactant molecules [32]. This results in a higher concentration of reactants at the catalyst surface and it lowers the activation energy of their reactions. Copper distinguishes itself from most transition metals because it has a filled 3d-shell and can only form soft bonds with carbon via its empty 4s state. As a result, copper has the lowest affinity to carbon and a very low carbon solubility (0.008 weight% at $\sim 1050^{\circ}$ C [80]). For graphene synthesis, this property constitutes a major advantage because it ensures that graphene grows by surface adsorption while for most transition metals, carbon mixes and then segregates at the surface [81]. The carbon segregation often results in a multilayer graphene film whereas the growth by carbon adsorption tends to generate a single layer graphene. Indeed, once the catalytic copper substrate is fully covered by carbon, the growth of a second layer is thermodynamically unfavorable and the growth terminates; it is a self-limited process.

CVD processes are very complex because they involve a series of physicochemical steps and surface reactions which are rarely achieved under chemical equilibrium [82]. Additional factors such as temperature and concentration gradients, geometric effects, and gas flow patterns depend mainly on the reactor being used and make the exact kinetic analysis extremely difficult. A logical approach to this problem is to determine 1) the driving force and feasibility of the process by a thermodynamic analysis and 2) the step that limits the growth rate with a basic kinetic model.

3.1.1 Thermodynamics

Thermodynamic models help predict the influence of the thermodynamic variables such as temperature, total and partial pressure on the deposition efficiency and nucleation process. Zhang et al. [83] developed a model based on the electronic structure calculation of carbon atoms adsorbed on Cu and the minimisation of Gibbs free energy. First, they showed that the dehydrogenation of methane on Cu was thermodynamically unfavorable, suggesting that graphene grows from nucleation of small hydrogenated carbon species, such as CH_x , rather than from atomic carbon. To understand the thermodynamics of the nucleation process, they proposed a relation between the chemical potential of carbon μ_C and the one of hydrogen μ_H (or equivalently its partial pressure P_{H_2}), as shown in Figure 1a. The chemical potential of an adsorbed atomic carbon (C_1) and hexagonal carbon clusters (C_n) are represented by horizontal lines. Carbon structures in the vellow region are stable, whereas those in the white area are unstable and react with H₂. In this case, hydrogen acts as an etching reagent. In Fig. 3.1a, graphene clearly has a lower chemical potential than that of the source gases for most experimentally accessible pressures (blue rectangle); this is the thermodynamic force to grow graphene. Atomic carbons, however are unstable for these pressures. This means that graphene will nucleate from small carbon clusters whose size depend on P_{H_2} and the partial pressure ratio $\chi = P_{CH_4}/P_{H_2}$. For a given hydrogen pressure, a high ratio such as $\chi=20$ (blue line) will generate smaller nucleation seeds than a low ratio such as $\chi=1/20$ (red line).

3.1.2 Kinetics

During a normal CVD process, the equilibrium that thermodynamic models assume is rarely achieved and the growth results from the non-linear kinetics of elementary processes. In CVD-graphene, the overall reaction $CH_4 + H_2 \rightarrow C + 3H_2$ can be divided in the following basic physicochemical steps [82, 84, 85]:

- 1. Mass transport of the reactants (CH₄, H₂) to the Cu substrate
- 2. Adsorption of the reactants to the Cu substrate

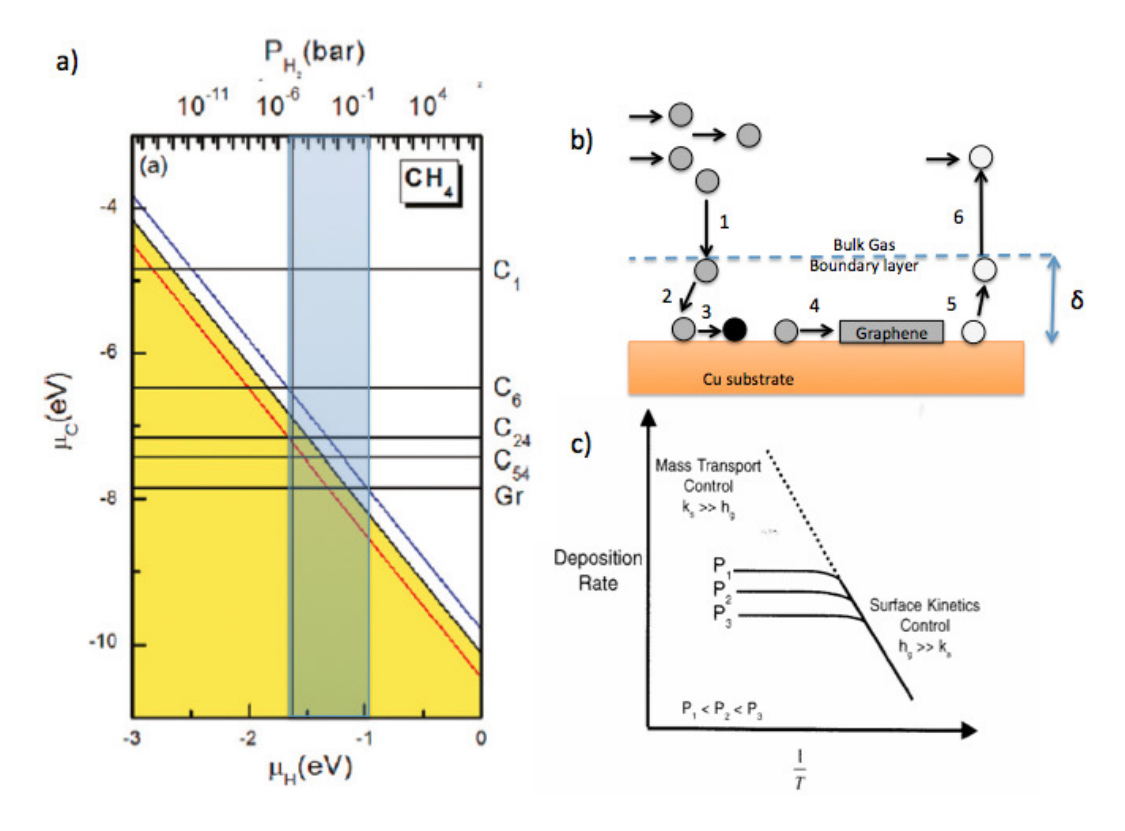


Figure 3.1: Thermodynamic and kinetic models for the CVD-growth of graphene on Cu. a) Thermodynamic relation between μ_C and μ_H at 1300 K. Black, blue and red lines stand for $\chi=1$, 20 and 1/20, respectively. (Reproduced from [83]). b) Schematic of the physicochemical processes involved in a CVD growth. C) Diagram illustrating the effect of temperature and pressure on the growth rate in the two kinetic regimes (Reproduced from [82])

- 3. Single or multi-step reactions at the Cu surface
- 4. Diffusion of the carbon species on the surface to form the graphene lattice
- 5. Desorption of the inactive species (such as hydrogen)
- 6. Mass transport of the inactive species away from the surface

These processes, illustrated in Fig. 3.1b, can be classified into two categories: mass transport (1 and 6) and surface reaction steps (2 to 5). To determine how they couple, the presence of a stagnant boundary layer due to steady state gas flow is often assumed [86]. In this boundary layer of thickness δ , the reactant concentration varies from the bulk gas concentration C_g to the surface concentration C_s . Assuming

a linear concentration gradient, the flux of reactants through the boundary layer J_{mt} can be described by Fick's law:

$$J_{mt} = \frac{D(C_g - C_s)}{\delta} \tag{3.1}$$

where D is the diffusivity coefficient. The rate at which the reactants are consumed J_{sr} at the surface to form graphene can be approximated to first order by

$$J_{sr} = k_s C_s \tag{3.2}$$

where k_s is the surface reaction constant. In steady state conditions, the total flux can be written

$$J_{tot} = C_g \frac{k_s D/\delta}{k_s + D/\delta} \tag{3.3}$$

Depending on which one of the two processes is the slowest, the growth is said to be mass transport or surface reaction limited. In the regime where $D/\delta \gg k_s$, the surface reactions control the growth rate which increases exponentially with the substrate temperature according to the Arrhenius equation. In the regime where $k_s \gg D/\delta$, the mass transport is the rate-limiting process and the growth rate is nearly independent of temperature (Fig. 3.1c).

Bhaviripudi et al. [84] investigated the growth of graphene by low pressure CVD (LPCVD) and atmospheric pressure CVD (APCVD), and they argued that APCVD growth was mass transport limited whereas LPCVD growth was a surface kinetic controlled process. Indeed, since $D \propto 1/P_{tot}$, the mass transfer coefficient D/δ increases at low pressure and becomes larger than k_s . This regime of transition by pressure variation is illustrated in Fig. 3.1c.

3.2 Experimental method

3.2.1 CVD System

For the purpose of our research, a low pressure thermal CVD system, shown in Fig. 3.2, was used to synthesized graphene. Each part of the system allows to control

a specific growth parameter, namely: a) the precursors used, b) their ratio, c) the growth temperature and d) the total gas pressure.

The methane and hydrogen precursors (a) are contained in two separate gas tanks equipped with a regulator to adjust the outlet gas pressure. The gas bottles are connected to copper tubes of 1/4-inch diameter which input the gases in their respective flow meter. The flow meters allow to adjust the partial pressure of each gas and their ratio (b) in the reaction chamber. Two sorts of flow meters were used in the course of our research: variable area flow meters (Matheson FM-1050) and mass flow controllers (AALBORG GFC). Unless specified, all growths mentioned below were realized using the first type of flow meters. It is worth mentioning that the calibration was later found to be incorrect insofar as the actual flows were systematically overestimated. The flows reported below have been corrected a posteriori, based on measurements with the mass flow controllers. The gases coming out of the flow meters are mixed with a cross connector and are conducted in the reaction chamber by flexible stainless steel tubing. A venting valve is connected to the extra port on the cross connector.

The reaction chamber consists of a closed end quartz tube with a diameter of 1 inch. The tube is inserted vertically in a resistance furnace whose temperature (c) can be adjusted by a microcontroller. The total pressure (d) in the quartz tube is measured by a Pirani gauge placed at the end of stainless steel tube and displayed on a controller. When no gas is flowing, the whole system can be pumped to a base pressure of 1 mTorr with a rotary pump. The pressure can be manually increased by partially closing the valve before the pump.

3.2.2 Growth Procedure

The complete synthesis process involves three main steps. The first consists in cleaning the quartz tube and the copper substrate in order to decrease the amount of contaminants that might inhibit the growth. The quartz tube is cleaned using concentrated nitric acid, rinsed in de-ionized water and then heated up to 1100°C until it dries. A scanning electron microscope (SEM) picture of the copper substrate, a 25 micron-thick polycrystalline Cu foil (Alfa Aesar #13382) is shown in Fig. 3.3a.

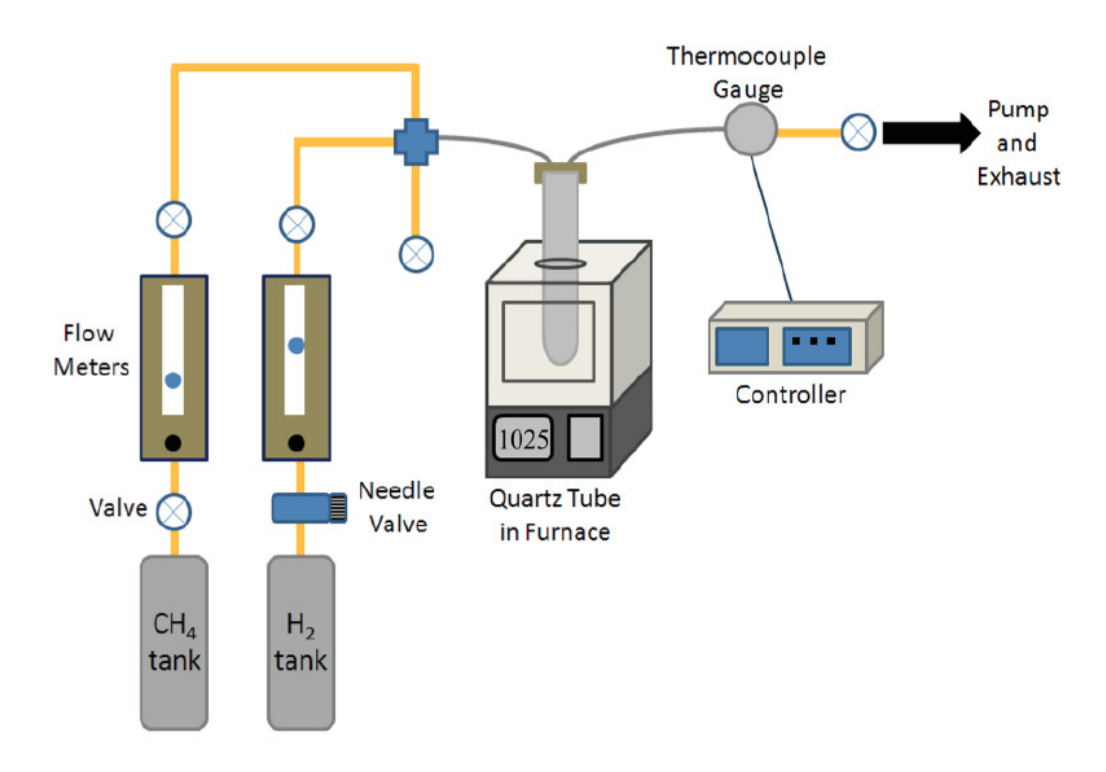


Figure 3.2: Schematic of the CVD system (Reproduced from [87]).

The vertical grooves come from the manufacturing of the foil and the white dots are impurities. The foil is cleaned by dipping it successively in acetone (10 s), water (10 s), acetic acid (10 mins), water (10 s), acetone (10 s) and isopropanol alcohol (10 s). It is then blow-dried with a nitrogen gas gun. The role of acetic acid in this cleaning procedure is to remove the native Cu oxide layer [32].

The Cu foil is further cleaned during the second step of the synthesis, the annealing. First, the Cu foil which dimensions are typically 1×2 inches are inserted at the bottom of the quartz tube. The CVD system is pumped down to its base pressure (1 mTorr). Then the flow of H_2 is set to 1-2 sccm with a low pressure (~40 mTorr). The tube is introduced in the furnace which gradually heats up to ~1030 °C. Once this temperature is reached, the Cu foil is annealed in these conditions for an extra 30 minutes. Fig. 3.3b shows the surface of an annealed copper foil with a grain boundary in the middle. Annealing plays a double role. It helps to remove the surface contaminants and copper oxides. It also changes the surface morphology and increases

copper grain size [32]. As we will discuss later, the surface roughness, grain boundary, defects and impurities play a significant role during the growth process but the exact effect of annealing on the morphology is difficult to predict.

Particular attention was given to the final step, the growth itself, since it is by far the most critical of the synthesis process. The CH₄ and H₂ flows are adjusted to obtain a certain ratio χ and if necessary, the total pressure is increased by partially closing the pump valve. Unless specified, all growths were realized at P=1Torr. These conditions are maintained for a definite growth time (usually ~30 minutes), then both gas flows are stopped and the quartz tube is cooled to room temperature. This is usually done by simply taking the tube out of the furnace and immersing it in water. The resulting Cu foil is coated with a graphene films as it can be seen on Fig. 3.3c and d. In Fig. 3.3c, the growth was not terminated in order to show the difference between Cu and graphene. Graphene appears in dark gray and Cu in light gray. The ripples seen in graphene can be attributed to the Cu steps underneath [88]. Fig. 3.3d shows a complete growth with the presence of small bilayer regions and wrinkles associated with the thermal expansion coefficient difference between Cu and graphene.

3.3 Results and discussion

Much has been written about the effect of the growth parameters on the graphene synthesis but some contradictory interpretations are still being debated. This doubtfulness probably arises from the fact that there are many uncontrolled variables (gas flow pattern, temperature gradient, etc) so that no two CVD systems are identical. Therefore, one must be careful when reading the literature and comparing results. The main goal of our investigation was to synthesize a high quality graphene film with low defect and contaminant density, as well as large grain size (low grain density). In what follows, we discuss some observations which can be interpreted using the models described above.

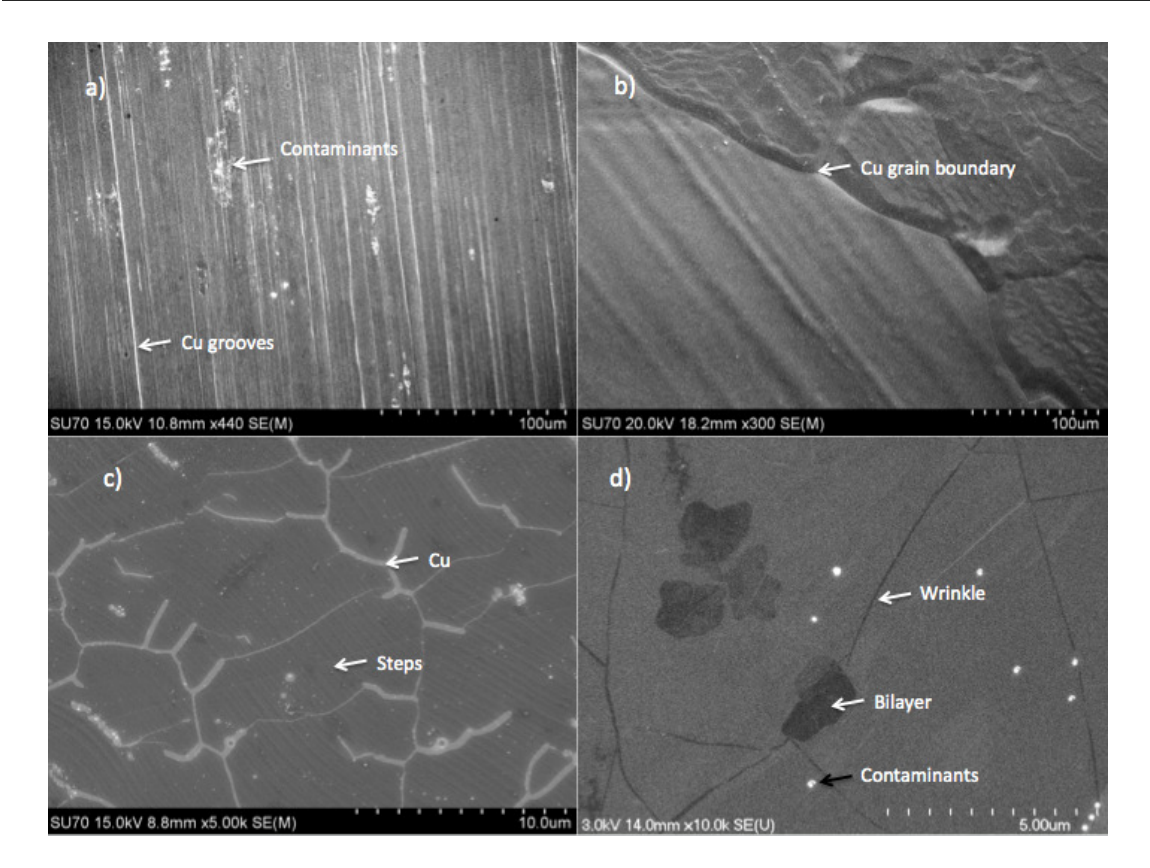


Figure 3.3: Typical CVD growth of graphene on copper. SEM pictures of (a) the copper foil before the process, (b) the copper foil after annealing, (c and d) graphene on copper.

3.3.1 Effect of the Gas Ratio

We first considered the effect of changing the gas ratio χ used during the growth. Following the seminal work of Li et al. [30], we first realized growths at high ratio $(\chi \approx 5)$. As it can be seen on Fig. 3.4a, the resulting graphene film contained many bilayer regions (darker spots). In comparison, the growths at low ratio (~ 0.7), as the one shown in b, created much fewer bilayers. Many groups [84, 85, 89] reported the increase of bilayer density at high ratio χ but none gave a satisfactory explanation, partly because the growth mechanism of the bilayer was not well understood. However, according to recent a study [90], bilayers grow underneath the first layer during the nucleation stage. Thus, a high bilayer density indicates a high grain density, or equivalently a small nucleation size. This result is consistent with the thermodynamic model illustrated by Fig. 3.1a which predicts that the nucleation size decreases when

 χ increases (and/or P_{H_2} decreases). Therefore, to obtain high quality graphene film with low bilayer density and large grain size, the growth must be realized at small gas ratio χ .

The thermodynamic model however stipulates that there is a lower limit for χ (or P_{H_2}) beyond which the growth is not possible. In this regime, the concentration of H_2 is so high that it effectively etches the graphene. Vlassiouk *et al.* [85] proposed the following etching reaction: H_s + graphene \Leftrightarrow (graphene-C) + $(CH_x)_s$

In c), the growth was performed at $\chi=0.3$ and no bilayer can be seen. However, the presence of black lines seems to indicate that the grains did not coalesce entirely. We impute this observation to the high H_2 concentration. The etching power of the hydrogen was also observed when at high ratio ($\chi=5$) graphene was cooled down very slowly in a H_2 atmosphere. As d) shows, the bilayer density is very high, but most notably, large areas of the Cu foil are visible. Similar results where reported [85, 91] and the holes in the graphene film were attributed to the etching action of hydrogen.

3.3.2 Effect of the Substrate Morphology

Throughout our investigation, we observed what appeared to be the influence of the substrate on the growth several times. Since it is difficult to control the surface morphology of the Cu foil, we are constrained to analyse the results a posteriori. The effects we observed can be divided into two categories. In the first one, the copper roughness seemed to impede on the growth process. This effect can be seen in Fig. 3.5a and b where the white spots correspond to the bare copper. In Fig. 3.5a, these spots are clearly aligned along the grooves of the manufactured Cu foil (see Fig. 3.3a). In Fig. 3.5b, the copper spots appear at the tip of the copper steps. These observations indicate that high substrate roughness is detrimental to the growth.

However, we also observed the opposite effect where the copper defects acted as nucleation sites. Fig. 3.5c is an optical microscope image of small white graphene flakes (discussed in the next section) on Cu. This image reveals that the flakes were formed along the large and curvy copper groove. Fig. 3.5d also shows that bilayers (in

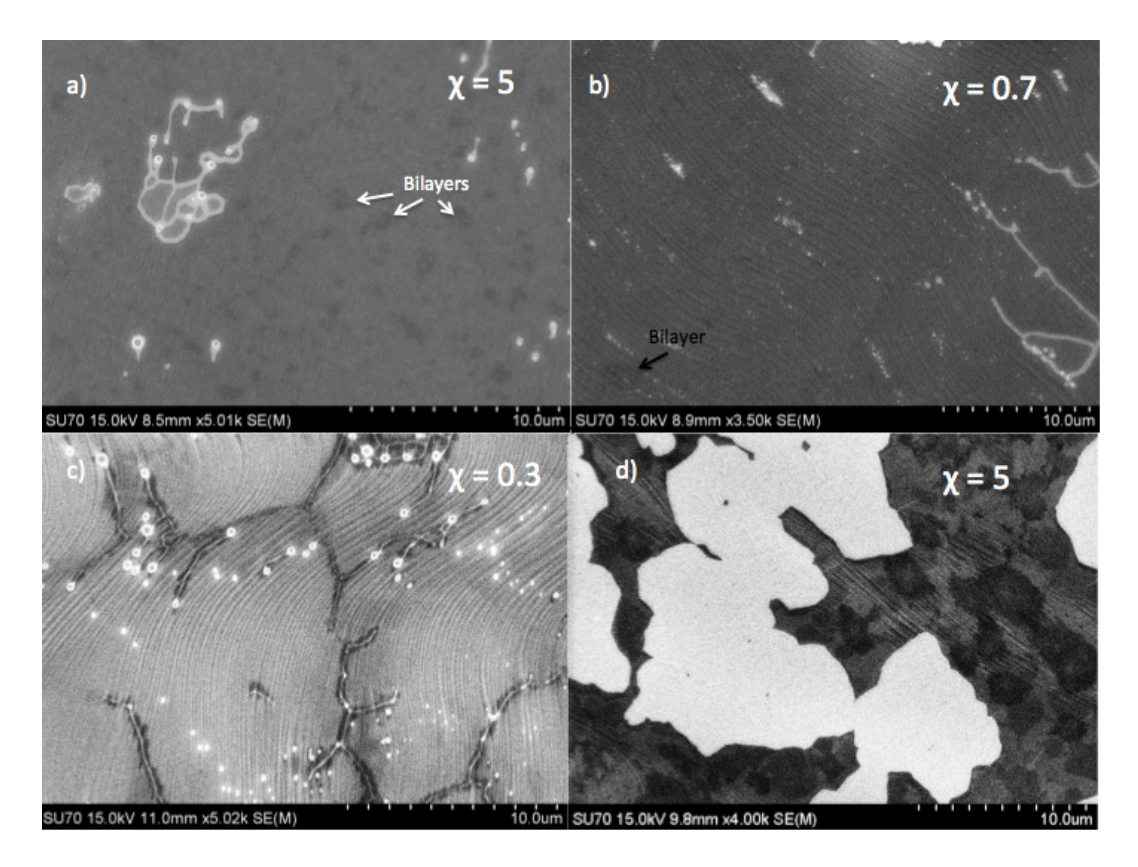


Figure 3.4: SEM pictures of graphene on Cu at various gas ratios χ . Growth shown in a), b) and c) were cooled down rapidly whereas the one in d) was cooled down very slow in an H₂ atmosphere.

black) are formed around the white defects, suggesting that these defects act as seeds during the nucleation stage. Many experimental studies[92, 93] reported this effect and theoretical works [94, 83] showed that the defects and steps significantly reduce the nucleation barrier. Therefore, a flat Cu surface is needed in order to reduce the nucleation density. This can be done by using a chemical polishing method [93] or by extending the annealing time for 3 hours [92]. With this method, Wang et al. recently managed to grow graphene domains up to 0.4×0.4 mm² by using an extremely low gas ratio ($\chi \approx 0.001$).

3.3.3 Effect of the Gas Kinetics

Besides using a flat Cu substrate and a low gas ratio, Li et al. [95] showed that another way to reduce the nucleation density and growth rate is to use a copper-foil enclosure (Fig. 3.6a). This can be done by bending the copper foil and crimping the

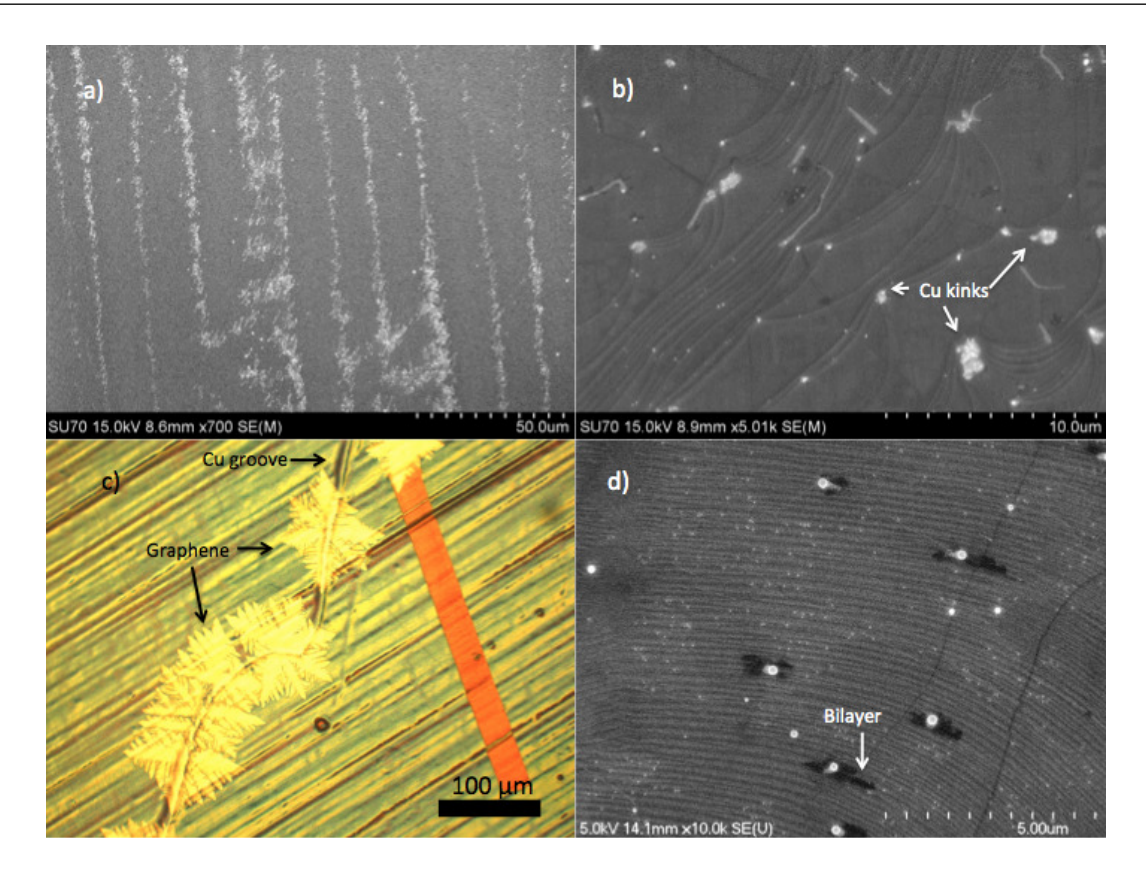


Figure 3.5: Influence of the substrate topography. Sharp copper features can hinder the growth (SEM pictures a and b) or favor graphene nucleation (optical image c) and bilayer formation (SEM picture d)

edges. Using similar conditions ($\chi=0.7$), the graphene film on the outside showed the same characteristics as those reported above, but the growth on the inside of the enclosure was totally different. We found a low density of dendritic graphene flakes that we named graphlocons due to their resemblance to snowflakes (flocons de neige in French). We measured the fractal dimension of typical graphlocon (Fig. 3.6b) with a box counting method [96]. First, the fractal image was converted in a black or white figure and divided a 2D lattice with square of size R. A program counted the number N of boxes containing a black fractal area. This operation was repeated for different values of R and the results were plotted as in Fig. 3.6c. The Minkowski-Bouligand dimension of the fractal (also known as box-counting dimension) was calculated as $d=-\log(N)/\log(R)$. By excluding the data point at large size R in Fig. 3.6c, we found slope corresponding to a dimension d=1.77±0.03. In comparison, the Sier-

pinski hexagon has a dimension of ~ 1.771 [97]. Fig. 3.6d, which shows the center of a graphlocon, gives more evidence to the idea that impurities (in white) serve as nucleation centers for single and multilayer graphene. Depending on the growth, the graphlocons had a total diameter of between 30 and 200 μ m. By comparison, Li *et al.* [95] found domains of up to 0.5 mm in size with much less fractal shapes. They were however unable to provide a rational explanation for the growth mechanism of these large domains.

We believe that the low nucleation density can be explained by considering the kinetic model described in section 3.1.2. Indeed, in LPCVD, the growth is known to be limited by the surface reaction kinetics [84]. By closing the Cu foil, we strongly impede on the mass transport to the surface so that the growth becomes mass transport limited. In this regime, the diffusion coefficient D is the parameter that governs the growth, and its value differs for the two precursors. A very simple approximation using the kinetic theory of gases reveals that the diffusion ratio is $D_{CH_4}/D_{H_2} = \sqrt{M_{H_2}/M_{CH_4}} = 0.35$ where M is the molecular weight. This suggests that the methane concentration inside the copper enclosure would be lower than the one outside. In these conditions, the thermodynamic model predicts larger nucleation size and lower nuclei density. This conclusion is also consistent with the results of Wang et al. [92] mentioned above. However, this model does not explain the fractal shape of the graphlocons.

3.4 Transfer Method

In order to probe its electronic properties, graphene must be transferred from the metallic copper catalyst onto a insulating substrate, such as glass, quartz and oxidized silicon wafers (SiO₂/Si). The later is particularly convenient for optical imaging [98] and, as will be discussed in the next chapter, for the fabrication of electronic devices. Many techniques using transfer layers such as thermal release tape [22] and PDMS [99, 60] have been proposed, but the most common and straightforward method employs a sacrificial PMMA layer. This technique, as we will show, generally yields good results,

3.4 Transfer Method 31

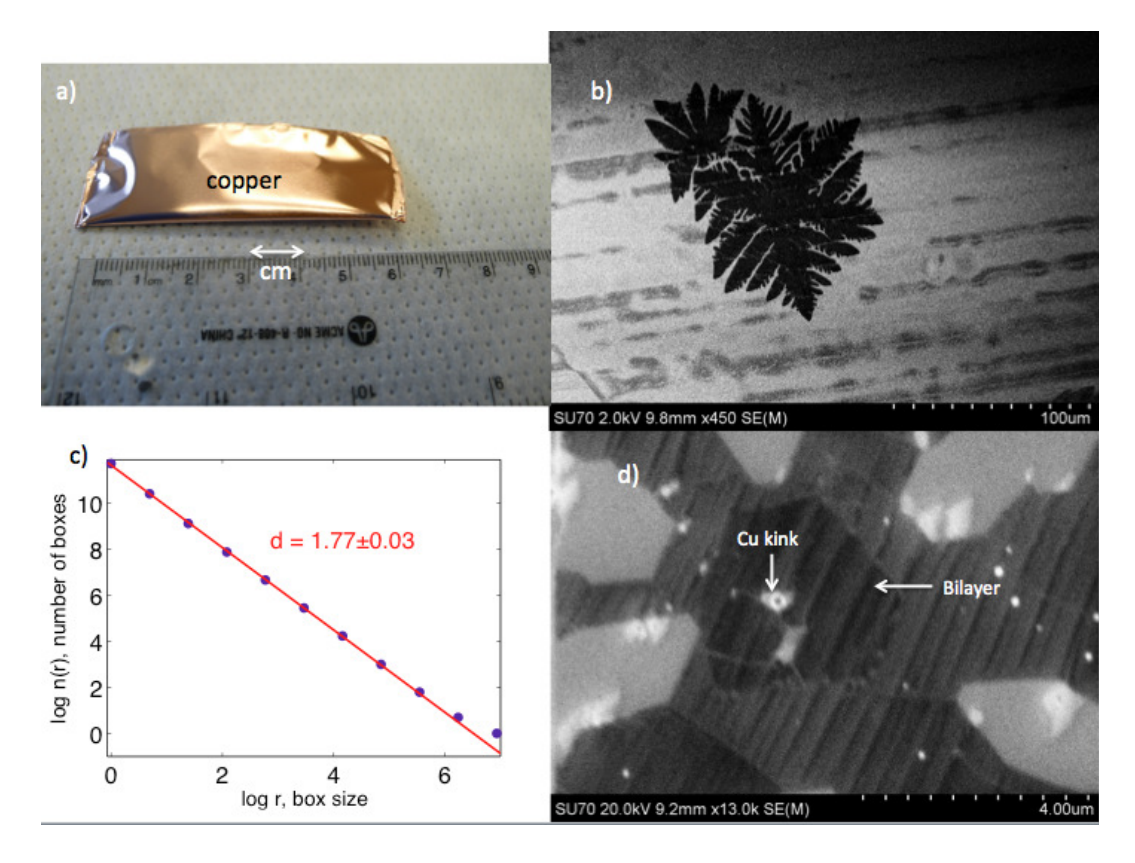


Figure 3.6: Growth of *graphlocons* in a copper enclosure (a). b) SEM image of a graphlocon on copper and (c) an estimation of its fractal dimension by the box-counting method. d) SEM image of the center of a graphlocon.

although it still requires some optimization. It is worth mentioning that direct transfer methods have been reported [100], but they usually involve complicated processes or have low yield.

For the purpose of our research, we used an optimized variant of the technique proposed by Li et al. [30]. A schematic of the transfer process is illustrated in Fig. 3.7. Firstly, PMMA A2 is spin coated at 1000 rpm during 45 s on one side of the graphene/copper foil. In order to spin coat on a flat foil, this step was sometimes preceded by the lamination of the foil with a stiff thermal release tape. This made the spin coat process easier and the PMMA layer more uniform. To release the tape, a quick bake (5 s at 120°C) is needed. The copper is then etched away by an oxidizing solution of 0.1 M ammonium persulfate (NH₄S₂O₈). The floating PMMA/graphene layer is transferred in DI water using a dipper. The film is transferred on the desired

substrate either by scooping it or by using a funnel which auto-aligns the film on the substrate lying at the bottom. As reported by Liang et al. [60], we observed that using a hydrophilic substrate improved the transfer quality. Hydrophilic surfaces spread the water more evenly during the transfer and create less folds in the PMMA/graphene stack. SiO₂ surfaces become more hydrophilic after a brief dip in HF (50:1 DI/HF). As the water between the graphene and the substrate dries, the film is dragged into contact with the substrate and colors appear. However, sometimes water gets trapped in the gaps between the graphene and the substrate. The water can be dried by baking the substrate on a hot plate at around 150°C for one minute, as shown in Fig. 3.7b.

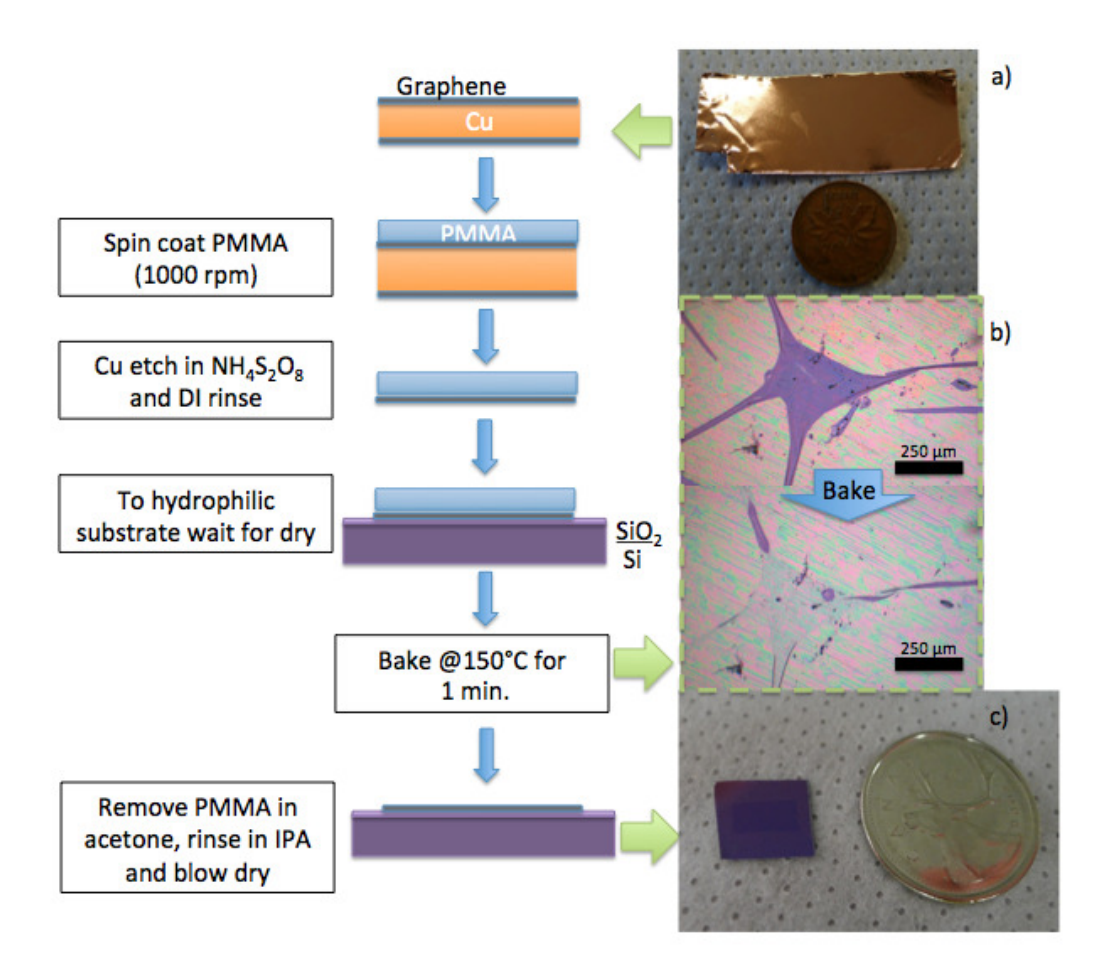


Figure 3.7: Schematic of the transfer of graphene from copper (a) to SiO_2 (c). b) Optical images of large folds containing water before and after baking at 150° C.

The PMMA layer can then be removed by dipping the sample in acetone. Unfor-

3.4 Transfer Method 33

tunately, PMMA residues were often found on the graphene. This problem can be partially addressed by using warm acetone ($\sim 40^{\circ}$ C), but by doing so, cracks on the graphene might also form. Finally, the sample is rinsed in IPA and blow-dried. Using this transfer process, we managed to transfer clean graphene film up to 5×5 mm² (Fig. 3.7c and Fig. 3.8a). This technique was also employed to transfer graphlocons (Fig. 3.8b).

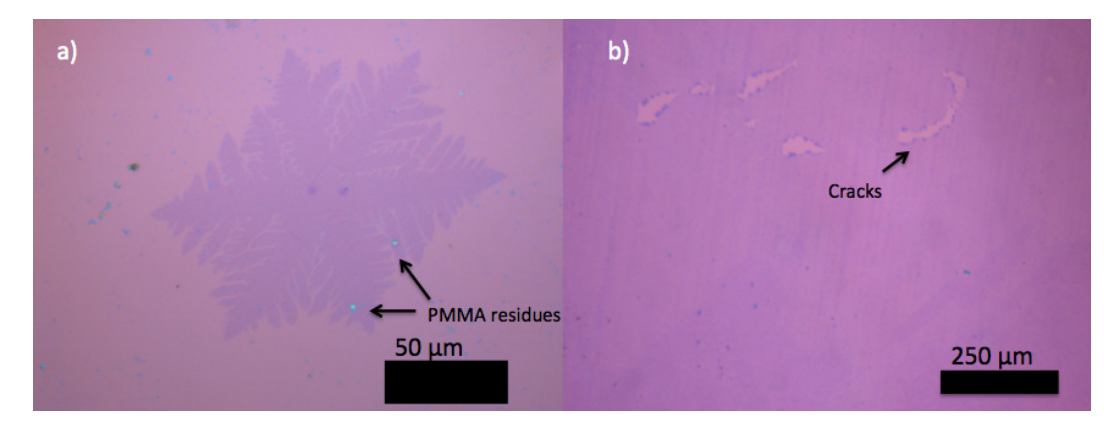


Figure 3.8: Optical image of a graphlocon (a) and a graphene layer (b) transferred on $\mathrm{SiO}_2/\mathrm{Si}$.

Characterization and Device Fabrication

Once graphene has been synthesjzed and transferred, the next step toward the fabrication of graphene electronic devices consists in characterizing the quality of the film. Optical microscopy and SEM imaging allow for a rapid qualitative inspection of the graphene film but sometimes their interpretation can be equivocal and rather imprecise. Even a characteristic as explicit as the number of layers can be error-prone. Hence, other characterization techniques which are more accurate and quantitative are required. In the following chapter, we present three methods we employed to characterize our CVD-grown graphene; namely, Raman spectroscopy, spectrophotometry and transmission electron microscopy (TEM). In the second part of this chapter, we describe the various steps involved in the fabrication of a Hall bar and graphlocon transistor.

4.1 Characterization

4.1.1 Raman Spectroscopy

Raman spectroscopy has proven to be one of the most reliable and straightforward ways to characterize graphene. In this method, information is extracted by measuring the inelastic scattering (Raman shift) of a monochromatic light, usually a laser, shone on the substance under study. For solid state material, the inelastic scattering involves the annihilation of the incoming photon and the creation of a phonon and Stokes photon. The Raman spectrum is representative of certain regions of the phonon as well as electron band structures of graphene which vary significantly with the number

4.1 Characterization 35

of layers [38]. Thus, Raman spectroscopy allows to unambiguously determine the number of graphene layers [101]. It also gives a good estimate of the defect density [101].

For the purpose of our study, we used a Renishaw System 1000 Raman microprobe, which consists of an argon-ion laser (514.5 nm), a holographic spectrometer and an Olympus BH-2 microscope equipped with 50× objective. This system, which is located in the Department of Mining and Material Engineering (McGill), has a spatial resolution of 2 μ m and wavenumber resolution of 1 cm⁻¹. The magnified Raman spectrum in Fig. 4.1a was obtained using the maximum laser power (25 mW) and 5 consecutive acquirements on a monolayer similar to the one shown in Fig. 3.8b. Among the many peaks that are identified, the three most significant are the G-peak $(\sim 1589 \text{ cm}^{-1})$, the D-peak $(\sim 1347 \text{ cm}^{-1})$ and the 2D-peak $(\sim 2690 \text{ cm}^{-1})$. The Gband results from a first-order Raman scattering process involving in-plane transverse optical (iTO and longitudinal optical (LO) phonons at the Γ point (Fig. 4.1b) [102]. On the other hand, the 2D-band arises from a second-order process where two iTO phonons are created near the K/K'points. This double resonance process is particularly prominent in graphene and is significantly affected by the number of layers [101]. Finally, the D-band is also a second-order process: one elastic scattering event with a crystal defect and one inelastic scattering event by creating or absorbing an iTO phonon near the K/K'point (Fig. 4.1b). Therefore, the intensity ratio of the G and D peak can be used to estimate the amount of disorder or defects in a sample.

The intensity ratio between the 2D and G peak (I_{2D}/I_G), as well as the full width at half maximum (fwhm) of the 2D-peak are very good indicators of the number of layers [101]. These features are well illustrated by Fig. 4.1c which displays two Raman spectra taken on a graphlocon transferred onto a SiO_2/Si substrate (Fig. 3.8a). The top spectrum was obtained by directing the laser on the dark central region (bilayer), whereas the lower one was measured with the laser aiming in the middle of one of the branches (monolayer). The latter spectrum shows a ratio $I_{2D}/I_G \approx 2$ and a 2D-peak fwhm of ~ 35 cm⁻¹. The bilayer region, however, yields a much smaller I_{2D}/I_G ratio

 (~ 0.7) and a 2D-peak twice as broad (fwhm $\approx 63~{\rm cm}^{-1}$). This confirms the presence of a bilayer/multilayer in the center of the graphlocon. We also notice that in both spectra the defect-induced D-peak is very weak, indicating the high quality of the graphlocon.

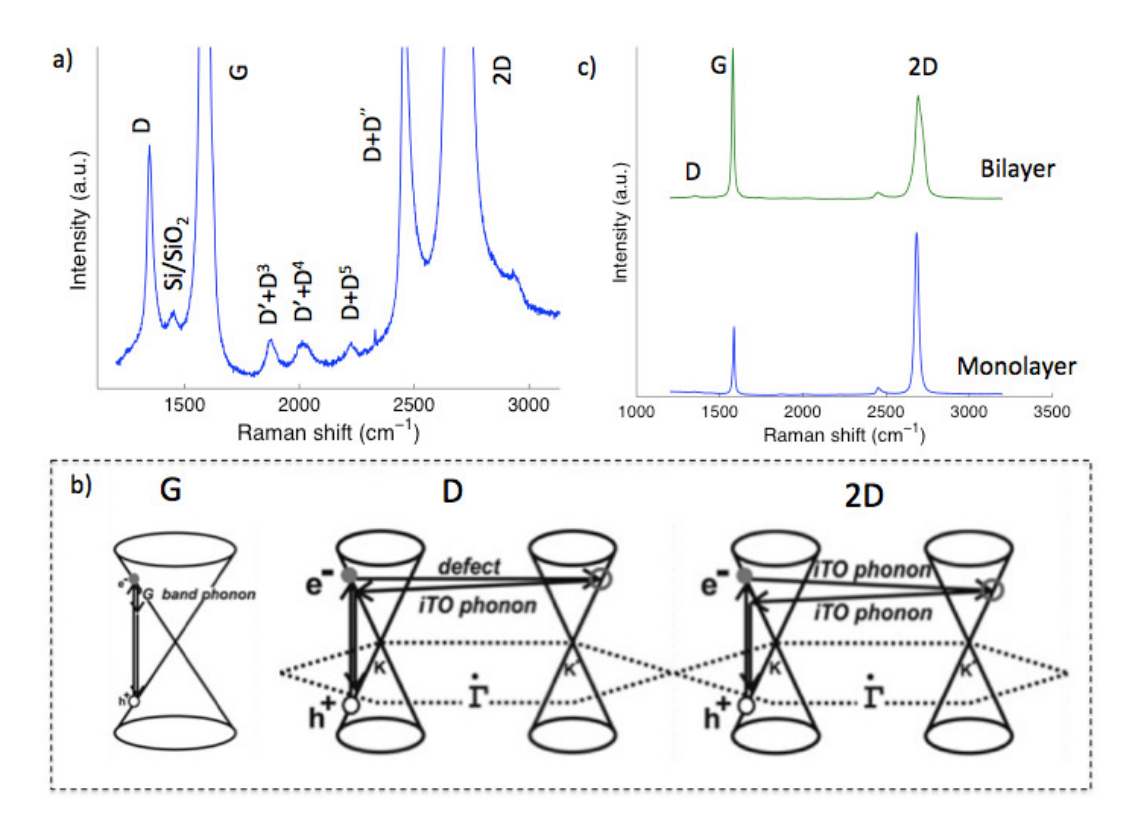


Figure 4.1: Raman spectroscopy in graphene. a) Typical spectrum of large-scale CVD-graphene. Raman peaks were identified based on [103]. B) First-order G-band process around the K/K point (left), second-order D (center) and 2D (right) process between the K and K point. (taken from [102]). C) Raman spectra of a graphlocon branch (monolayer) and center (bilayer).

4.1.2 Spectrophotometry

The electronic band structure of graphene can also be probed by measuring the absorbtion of light at different energies. Indeed, to be absorbed, an incident photon must have an energy greater than the band gap so that an electron from the valence band can be promoted to the conduction band. The absorption efficiency depends on the density of the initial and final states. Since graphene has a gapless linear dispersion curve at low energy, its spectral absorbance is finite and constant for a large

4.1 Characterization 37

range of low energy photons. It was predicted and measured to be $A \approx \pi \alpha \approx 2.3\%$, where α is the fine structure constant [12]. At higher energy, the dispersion relation curves (Fig. 2.2a) and absorption reaches a peak at 4.6 eV. This excitonic peak was predicted [104] and measured experimentally [105].

The absorbance spectrum of graphene is far from being as rich, precise and local as the one obtained by Raman spectroscopy, however, it allows to characterize the quality of large graphene samples and identify the number of stacked layers. The spectrum can be measured using a spectrophotometer, which is basically made of a light source, a monochromator and a photodetector. For our experiment, we used a Cary 5000 UV-Vis-NIR spectrophotometer located in the Department of Chemistry (McGill). This instrument has a wavelength spectrum ranging from 175 nm to 3300 nm and a beam size of about 5 mm. The absorption is measured by taking the difference between the intensity I_0 of a reference beam and the intensity I of the beam passing through the sample. Therefore, for this measurement, graphene must be transferred onto a transparent substrate. We transferred two graphene layers on quartz such that there were regions with one and two layers (Fig. 4.2a). It is worth specifying that the two layers mentioned here were not equivalent to the CVD-grown bilayer mentioned previously. They were simply the result of transferring one monolayer over another.

By subtracting the absorption contribution of the quartz plate, we obtained the two spectra shown in Fig. 4.2b. As one could expect, the absorbance of the two layers is approximately twice that of the monolayer. It must, however, be noted that in both cases, the absorption in the flat, constant frequency range is slightly larger than that of the theoretical value (2.3% and 4.6%, respectively). We attribute this larger absorbance to the transfer layer residue that remained on the graphene after transfer. Nevertheless, the two main features of the spectrum are clearly visible: a constant absorption at low frequency and a peak around 272 nm (~4.6 eV), as predicted. In Fig. 4.2c, we compare our measurement to the theoretical spectrum[104] and to another experimental spectrum [105]. One can see that all curves have a similar general behavior, with an absorption peak around 4.6 eV. The spectrum we measured

resembles the other experimental spectrum, with a slight offset possibly due to light absorbing residue. However, for both experimental curves, the absorption peak is less asymmetrical than the one predicted. The reason for this discrepancy is yet to be revealed.

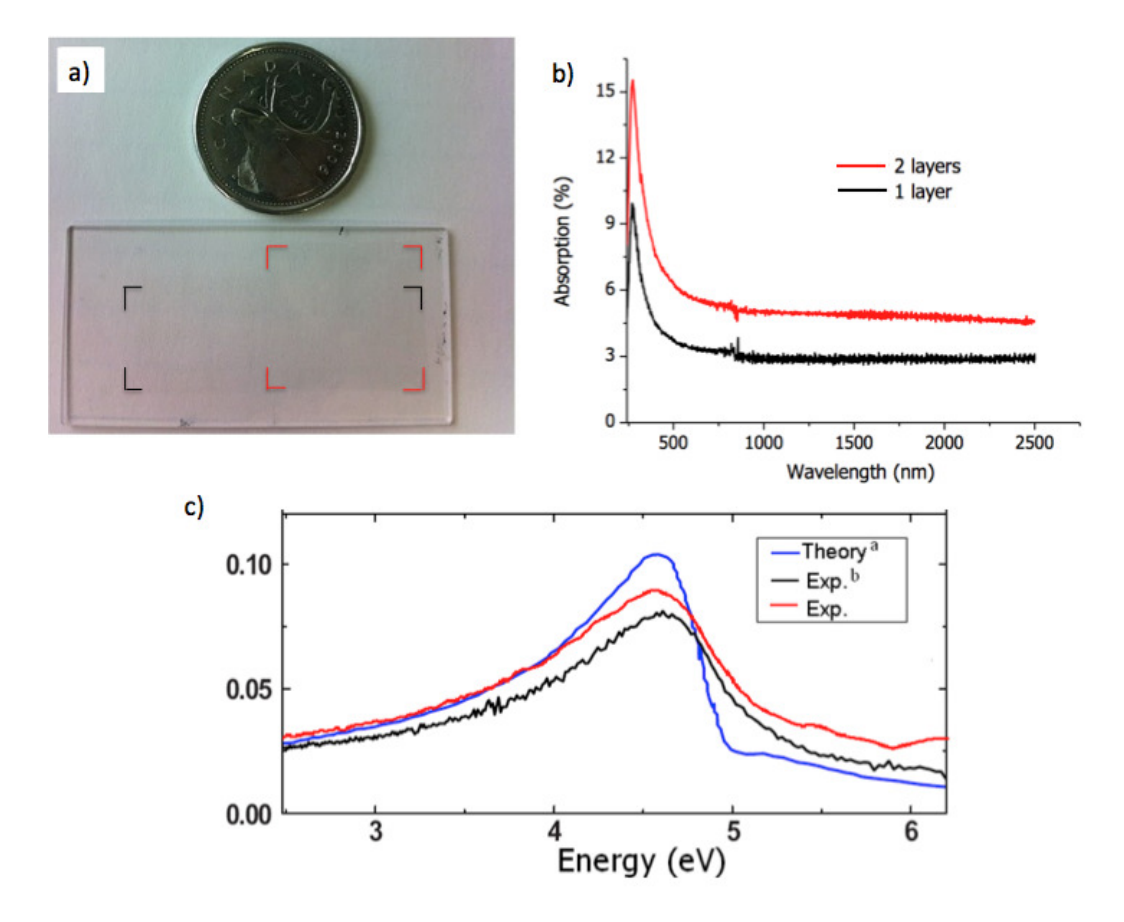


Figure 4.2: Characterization of graphene by broadband spectrophotometry. a) Optical image of two graphene layers on a quartz plate. b) Absorption spectra of one and two graphene layers. c) Absorption spectra of graphene (red curve) compared to a theoretical calculation (blue curve a:[104]) and another experimental curve (black curve, b:[105]).

4.1.3 Transmission Electron Microscopy

Raman spectroscopy and spectrophotometry provide indirect information on the graphene quality and the number of layers, both on the microscopic and macroscopic scale. For a direct observation of graphene at the atomic scale, one uses transmission electron microscopy, a technique in which images are formed from the interaction

4.1 Characterization 39

of an electron beam transmitted through the sample. Therefore, in order to obtain TEM images, the graphene sheet must be suspended on a porous substrate. We used silicon nitride membrane windows perforated with $\sim 2~\mu m$ holes (provided by Professor Reisner's group). Fig. 4.3a shows a TEM image of such a hole with a graphene film on top. The round mark is a charge accumulation artifact that was created when TEM was zoomed in that region. The TEM imaging was performed with a Philips CM200 located in the Department of Physics at McGill (Fig. 4.3a and d) and with a JEOL JEL-2100F available at Ecole Polytechnique Montreal (Fig. 4.3b and c). Both TEM were operated at 200 kV.

Fig. 4.3b shows a typical TEM image of graphene as transferred, before annealing. We generally observed a uniform amorphous structure studded with small crystalline particles. These observations resemble those made by Lin et al. [106] which attributed the amorphous features to a residual PMMA layer attached to the graphene film. The crystal particles, found in higher concentration on the dirtier samples, are probably copper residue remaining from the etching process. This interpretation is supported by the Energy-dispersive X-ray spectroscopy (EDS) spectrum shown in Fig. 4.3e. Besides the large silicon line coming from the substrate and the expected carbon line due to graphene, many copper lines and a sulphur line can be seen and attributed to etching residue. The large oxygen line is consistent with the presence of PMMA whose molecular formula is $(C_5O_2H_8)_n$, but the origin of the calcium lines is unknown. In any case, this analysis suggests that the transfer process is far from being clean as it introduces many microscopic impurities. Despite the fact that we did not observe the crystalline structure of graphene, the X-ray diffraction imaging (XRD) clearly showed the characteristic hexagonal diffraction pattern of graphene for some regions (Fig. 4.3c).

Lin et al. [106] proposed a method to partially remove PMMA residue which consists in annealing the sample in air at high temperature. Fig. 4.3d shows a TEM image of a sample after a 1 hour annealing in air at 200°C. The sample was partially destroyed after this process, leaving a large hole on half the suspended area. The

image of Fig. 4.3d was taken near that hole. We attribute the different gray contrast level to the folding of the graphene film. At the edge of these folds, the atomic structure of graphene seems to appear more clearly, but further investigation is needed to confirm that interpretation. Even after annealing, amorphous PMMA residue appeared to uniformly cover the graphene film. More work is required in order to find a cleaner transfer process or a post-transferred process that would effectively clean the graphene.

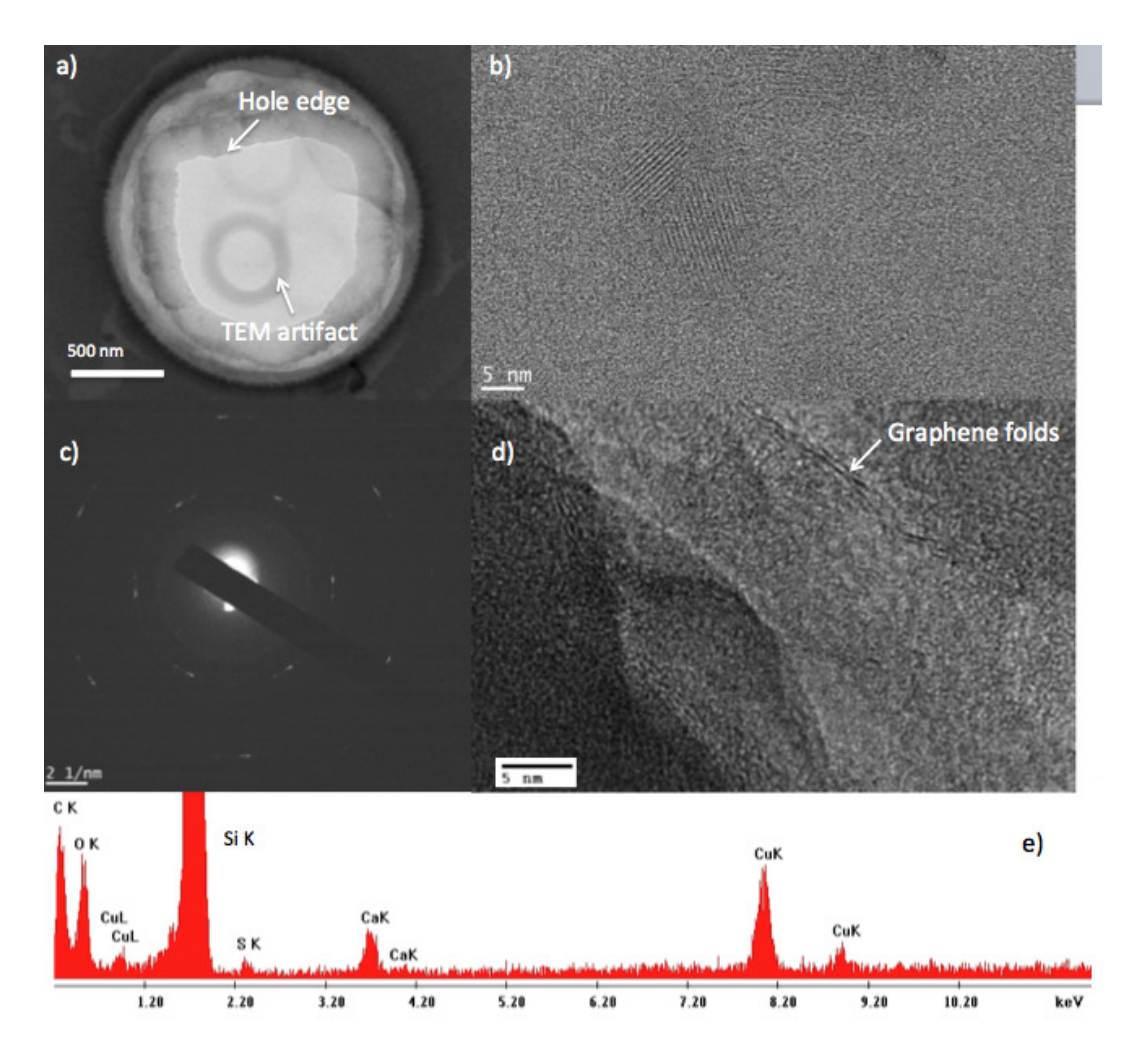


Figure 4.3: TEM-XRD-EDS analysis. a)Low-magnification TEM image of graphene suspended over a hole in the silicon nitride membrane. b) Typical high-magnification TEM image of graphene showing crystalline regions. c) XRD image showing an hexagonal pattern. d) High-magnification TEM image of graphene folds after annealing. e) EDS spectrum of graphene in a region similar to b).

4.2 Fabrication of Graphene Field Effect Transistors

Once a CVD-grown graphene sample has been properly characterized, its electronic transport properties, which are one of the main focus of this thesis, can be investigated. A useful electronic device for this purpose is the graphene field effect transistor (GFET) which, in its most basic form, is composed of a source, a drain and a gate. As we mentioned in Chapter 2, the gate acts as a planar capacitor with a thin dielectric separating the graphene sheet from the gate electrode. To fabricate such gate, we transferred graphene on a highly-doped (n^{++}) <100> silicon wafer on top of which a dry chlorinated thermal oxide of 285 nm was grown (University Wafer). Fabrication of the drains and sources, as well as the channel that links them will be the subject of the following sections.

4.2.1 Graphene Hall Bar

A convenient and widespread electrode configuration for measuring the magnetore-sistance of a material is the Hall bar, which we briefly introduced in Chapter 2 (Fig. 2.3a). This type of configuration consists of 6 ohmic contacts disposed along a graphene channel. Some comments must be made regarding the size of this channel. As we realized in Chapter 3 and in the first part of the current chapter, large scale CVD-grown graphene contains a fair amount of impurities and defects that are detrimental to its great electrical properties. One way to circumvent these extrinsic imperfections is to probe graphene locally, at a microscopic level, where the effect of macroscopic defects is less significant. Therefore, a small, micron-size channel to assess the intrinsic properties of graphene is desirable.

Fig. 4.4 illustrates the microfabrication process we developed in order to obtain GFETs with a Hall bar configuration. This process has the advantage of being scalable so that many devices can be produced on the same graphene/SiO₂/Si wafer. It consists of two main steps: Hall bar patterning and metal deposition. During the process development, the order of these steps was permuted and in what follows, we describe the sequence with the highest yield.

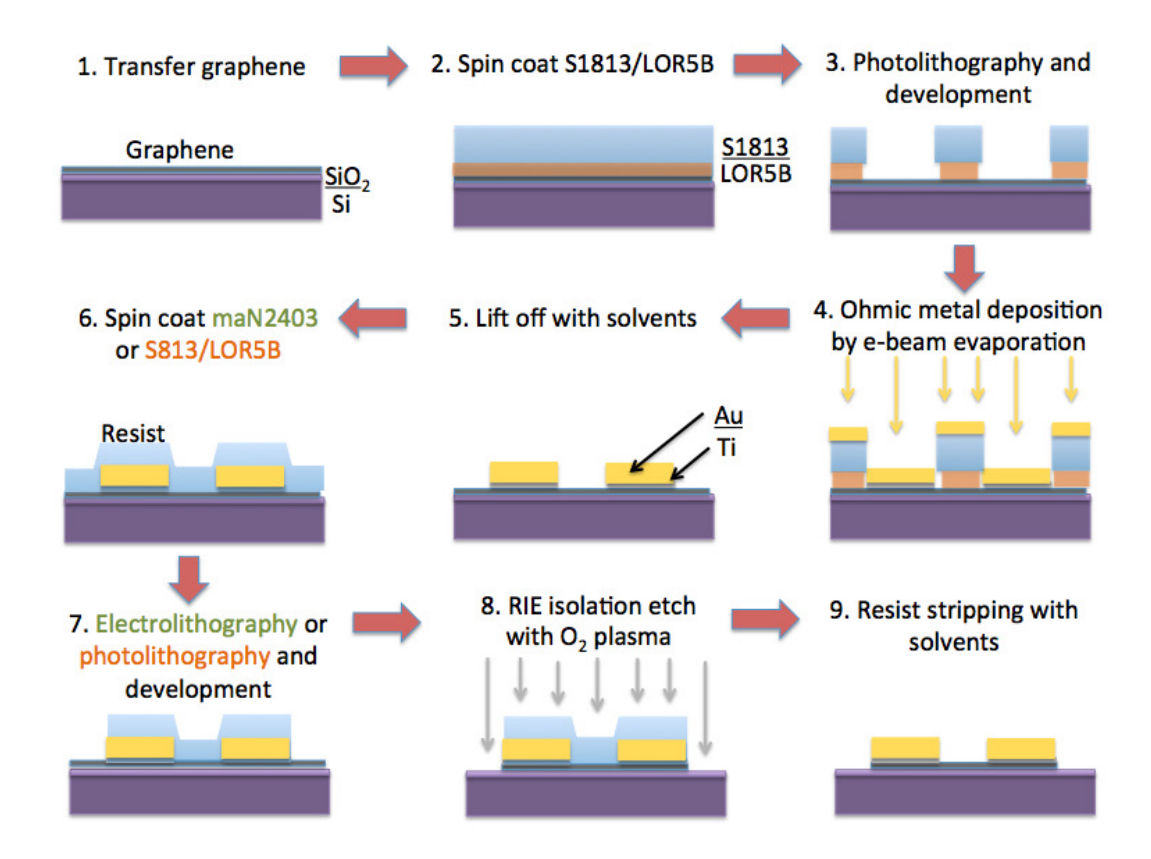


Figure 4.4: Schematic of the Hall bar fabrication process.

Electrode Deposition

The fabrication begins with the deposition of the metal contacts by a lift-off process (steps 2 to 5 in Fig. 4.4). First, the graphene/SiO₂/Si wafer is spin coated with two successive photoresists, LOR5B at and S1813. This step starts with the spin coat of the LOR5B for 5 s at 500 rpm and 45 s at 5000 rpm, followed by a soft bake at 200°C for 5 mins. The S1813 is then spin coated on top for 5 s at 500 rpm and 30 s at 4000 rpm. Then the sample is soft baked at 115°C for 1 min. The resulting LOR5B and S1813 coatings are respectively \sim 300 nm and 1.4 μ m thick. The geometrical pattern of the ohmic contacts is then produced by photolithography. In this process (step 3), the patterns of a 3-inch photomask (labelled McGill 57917 from FineLine Imaging) are transferred onto the photoresist using UV light. This can be done using one of the two mask aligners available in the McGill NanoTools Microfab (EVG620 and OAI aligner) although, at this point of the process, the precise

alignment of the photomask is not critical. The photomask contains multiple arrays of 6 individual bond pads converging in the center, where the graphene channel will later be patterned. The photoresist is exposed with a dosage of 80 mJ/cm² and then developed for 45 s in MF-319.

The next step (step 4) consists of depositing the metal contacts using an electron beam evaporator. For most of our devices, we first evaporated 10 nm of titanium to form an adhesive layer, followed by 100 nm of gold. Studies [107, 108] suggest that other metals could also be used, such as Al, Ni and Pd. The sample is finally immersed into a bath of N-methyl-2-pyrrolidone (Remover PG) at 40°C for 5 mins for the final lift-off (step 5). The success of this step relies mainly on the presence of an undercut in the LOR5B layer. This undercut allows the solvent to access and remove the resist on the edge of the metal contact, thus allowing an optimal lift-off. The resulting electrodes can be seen in Fig. 4.5.

Hall Bar Patterning

At this point of the process, all the electrodes are interconnected by a uniform graphene film. The rest of the fabrication process (steps 6 to 9) aims at isolating the Hall bar devices and defining a channel through which charge carriers will flow in each device. Considerable time and effort was devoted to develop an efficient patterning process. Many methods were investigated but two clearly showed better yield: photolithography and electrolithography.

Photolithography vs. electrolithography

For the first alternative, the photolithography, we employed a procedure very similar to the one described above. Here, the use of the LOR5B is not necessary because no undercut is needed, but this resist seems to leave very little residue on the graphene surface. Contrary to the photolithography for the contacts, the one for the channel necessitates a precise alignment of the photomask. This can be achieved with the proper use of one of the mask aligners. The smallest channel width on the photomask (McGill 57917) is 5 microns. The width can be made smaller by overexposing

or overdeveloping the photoresist. Typically, an exposure dose of 90mJ/cm² (or 11 s on the OAI aligner) with development of 45 to 60 s in MF-319 gave good results. Fig. 4.5a shows the patterned photoresists before the etching step. As one can see, the features are quite round, which is most likely due to the overexposure or overdevelopment. After the complete fabrication process (Fig. 4.5b), these curvy features result in an imprecise channel width. But worse still, most samples are left with photoresist residue after the full process (in blue in Fig. 4.5b). More work is needed in order to develop a residue-free process. Nevertheless, the photolithographic alternative is relatively easy to implement and it allows scalable fabrication.

Compared to photolithography, electrolithography, also known as electron beam lithography (EBL), has a much higher resolution and a more precise alignment system, resulting in well aligned sub-micron channels (Fig. 4.5c). As its name suggests, the EBL uses a focused electron beam to locally expose an electro-sensitive resist. This direct writing, as opposed to the global light exposure, is a very slow process which results in a very low throughput. Despite this limitation, our EBL process allows the fabrication of many devices on the same wafer. The core idea is to use a negative electroresist, which is a first in the McGill Nanotool Microfab. Indeed, since the area we want to protect with resist is very small, using a positive electroresist such as PMMA would lead to everlasting exposure time. Instead, we employed the negative electroresist maN2403 which was kindly provided by the INRS Énergie Matériaux Télécommunications Research Centre. The resist was spin coated on the sample (step 6) for 5 seconds at 500 rpm and for 30 s at 3000 rpm, then soft baked for 1 min at 90°C.

The EBL (step 7) was performed using the Hitachi SU-70 Pattern Generator of the Microfab which consists of a SEM equipped with lithographic capabilities. First, the Hall bar design is drawn in the DesignCad Express software. The channel shown in Fig. 4.5c and d was designed with a length of 1.5 μ m and width of 500 nm. The calibration and lithography procedure we used is similar to the one provided by the McGill Microfab. Briefly, the calibration involves the adjustment of the X-Y focus and

the calculation of the rotation matrix with the NPGS software. For the lithography, we executed arrays of Hall bar pattern, each replica properly aligned in the center of the gold contacts. Since the gold contacts have a known periodicity, only the first Hall bar needs to be aligned manually. We were able to pattern up to 80 Hall bars on one wafer using this technique. For the Hall bar shown in figure 5c and d, we used a magnification of $2000\times$ and an area dose between 80 and 160 μ C/cm². We systematically varied the area dose in order to optimize the resolution; the best results were obtained for $\sim 100 \mu$ C/cm². Finally, the unexposed resist was developed in MF-319 for 70 s.

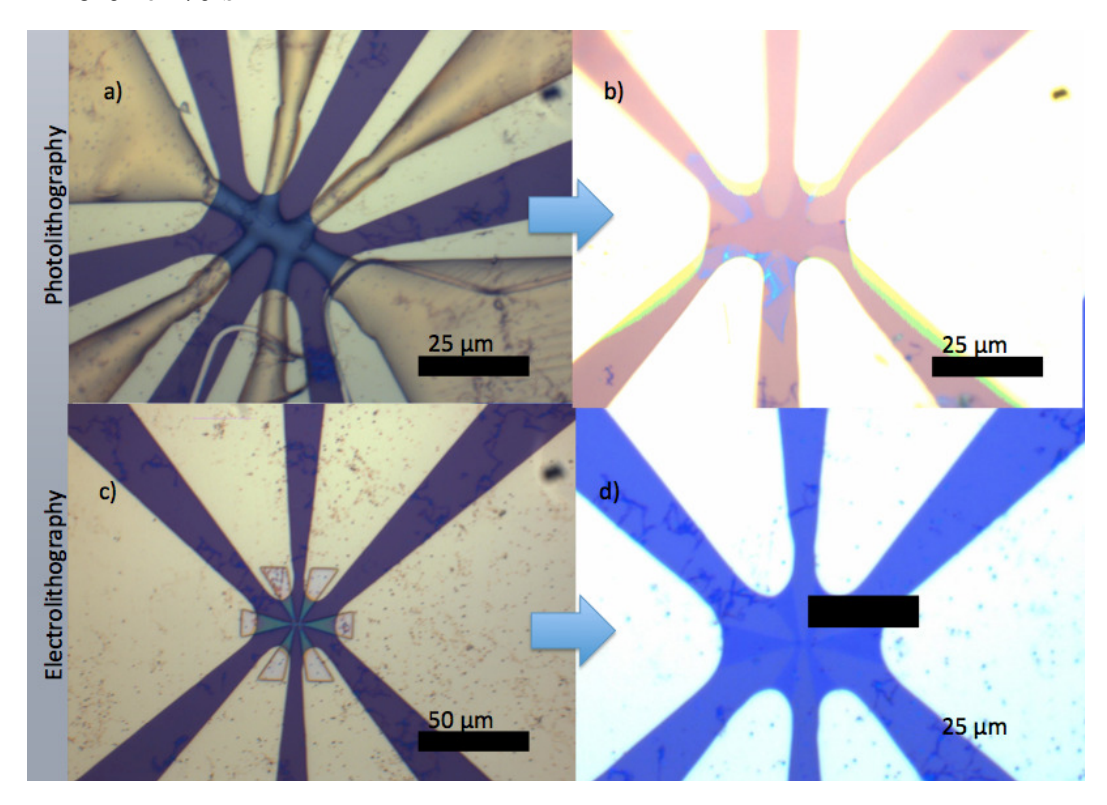


Figure 4.5: Comparison between photolithography (a, b) and electrolithography (c, d) for Hall bar patterning. a) and c) Optical images of patterned resist on graphene and Au (step 7 of Fig. 4.4). B) and d) Optical images of graphene Hall bars connected to Au contacts (step 9 of Fig. 4.4).

Reactive Ion Etching

Following lithography, the uncoated graphene can be efficiently etched away using a low power oxygen plasma. This is performed in a reactive ion etching (RIE) system which is essentially composed of a low pressure chamber where the O_2 gas enters.

Plasma is created by an electromagnetic field and ions attack and react with the wafer surface. Organic compounds are reactive to O₂ plasma, so a short and low power process is sufficient to remove the graphene without affecting the protecting resist too much. For the etching process (step 8), we employed the RIE system available in the Microfab, the MERIE P5000. Our recipe is comprised of three steps. First, the gas enters and the pressure stabilizes for 20 s at a pressure of 200 mT. Then a plasma is generated for 6 s at a power of 50 W and a pressure of 200 mT. The gas is finally expelled from the chamber for 10 s while the system provides 50 W of power. The result of the etching process is then examined with an optical microscope. For various reasons (defects in graphene, multilayers, etc), the etching procedure might have to be repeated a few times until the desired etch is achieved. Lastly, the photoresist or electroresist is stripped away using Remover PG at 40°C or acetone at room temperature, respectively. Fig. 4.6 demonstrates an effective plasma etch of a pre-patterned Hall bar after the stripping of the electroresist.

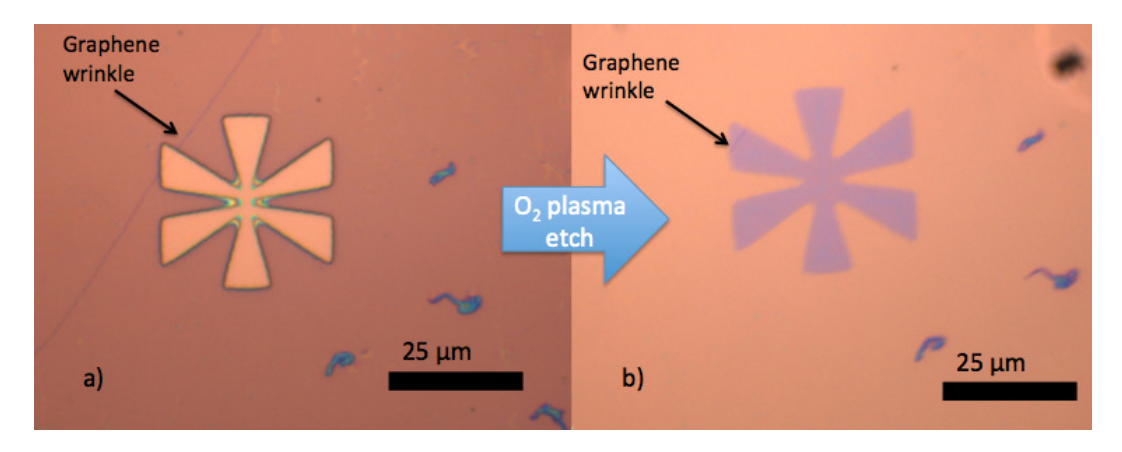


Figure 4.6: Optical images of a Hall bar a) before RIE, with electroresist and b) after RIE and stripping of the electroresist.

Other Patterning Processes

The lithographic processes discussed above have one major drawback; they both are very likely to leave resist residue on the graphene Hall bar. The TEM images presented previously revealed the presence of PMMA residue after transfer. The repeated use of resists during the device fabrication process doubtlessly leaveves more

impurities. To avoid this problem, we explored several uncommon patterning processes such as graphene lift-off, laser patterning and metal etchmask. The two first methods showed interesting results but also serious limitations that prevented their use for device fabrication. In both cases, more work would be required in order to optimize the process.

The graphene lift-off process proposed by Ye et al. [109] is analogous to a metal lift-off. Graphene coated with a PMMA transfer layer is deposited on a pre-patterned resist (Fig. 4.7a). Once the graphene is well bonded to the substrate, the resist is stripped in acetone, thus cutting the graphene layer in the patterned shape (Fig. 4.7b). However, this process was found to create many graphene folds, very rough edges and large defects. We believe that these imperfections are created during the lift-off because the graphene rips imprecisely and unevenly along the resist edge. Following the work of Kalita et al. [110], we also investigated the ablation of graphene by laser as a way to pattern Hall bars. A laser setup located at Ecole Polytechnique Montreal in Professor Michel Meunier's lab was used for this purpose. This setup employs a titanium-saphire laser to generate pulses of 40 fs, with a repetition rate of 1000 Hz and a wavelength of 800 nm. The laser was focused on graphene/SiO₂/Si sample which was installed on motorized stage. Moving the stage in X-Y directions allowed patterning of features with a resolution down to a few microns. The resolution was mainly limited by the size of the laser beam. Fig. 4.7c shows an optical image of the laser-patterned graphene. The main difficulty lies in the fine tuning of the laser power: a low power will not entirely ablate the graphene, but too much power will destroy the underlying silicon oxide (Fig. 4.7d), leading to gate leakage. Some efforts were spent on solving this problem but the low resolution of the in situ video camera impeded any progress. With a better camera in hand, this technique could be extremely advantageous because it is fast, clean (no resist involved), easy to control, and has a good resolution.

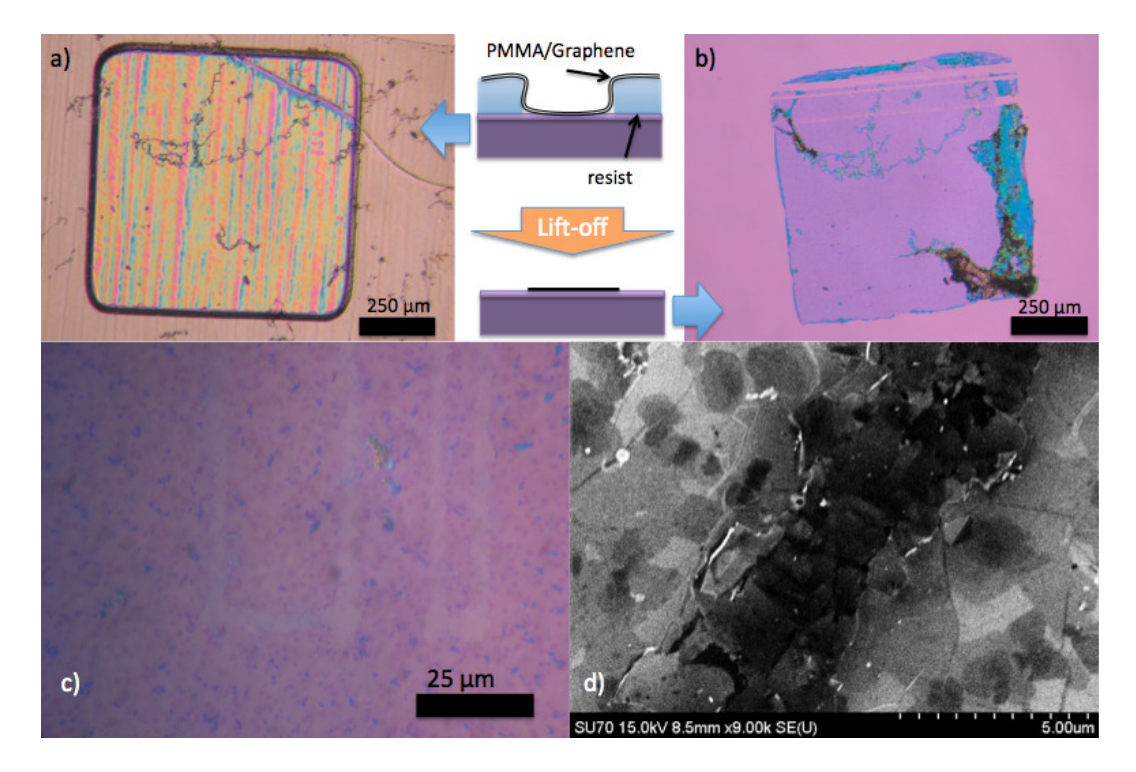


Figure 4.7: Graphene lift-off and laser patterning. Optical images of PMMA/graphene on a patterned photoresist (grey) before (a) and after (b) lift-off in acetone. Optical (c) and SEM (d) images of laser-ablated graphene (pale lines).

4.2.2 Graphlocon Transistors

The random shape and position of graphlocons on the wafer entails a slightly different fabrication process. In this case, electrical contacts must be customized for each graphlocon by EBL and no etching is needed since graphlocons are electrically isolated. The main difficulty of this fabrication process lies in the alignment of the contacts on the graphlocon. To overcome this technical problem, we first spin coated the sample with PMMA A4 (5 s at 500 rpm, 45 s at 4000 rpm and 60 s at 180°C) and patterned alignment marks on the electroresist. These marks are written by EBL with an area dose of 300 μ C/cm² and then developed in 1:3 MIBK:IPA for 45 s. The purpose of these marks is to 1) help locate the graphlocons on the wafer and 2) provide a length scale in X and Y for the calibration of the EBL. Fig. 4.8a shows an optical image of graphlocons covered with patterned PMMA. The alignment mark located at the top of the image is used to define the position of the two graphlocons (in the

lower part of the image) inside the grid formed by the alignment marks. Knowing the distance between the alignment marks, the X and Y distances between the alignment mark and the graphlocons can easily be determined with the microscope's software.

Once the EBL is properly calibrated and aligned using the alignment marks, the contact patterns are drawn by exposing the resist once again with an area dose of 300 μ C/cm². In order to avoid working frame limitations, we employed two lithographic layers: one for the small arms contacting the graphlocons and one for the distant large bonding pads. The latter layer, because of its size, needs to be fractured (see [87] for details on a similar procedure). Optical images of the resulting pattern after development (1:3 MIBK:IPA for 45 s) can be seen in Fig. 4.8b and c. In the second figure, the patterned arms appear well aligned with the branches of the graphlocons.

Finally, Ti/Au contacts are deposited using the same lift-off procedure as the one discussed earlier (steps 4-5 in Fig. 4.4). However, the lift-off process using PMMA A4 without undercutting layer was turned out to be difficult. As one can see in Fig. 4.8d, the gold over the right graphlocon did not lift off properly. Using a EL11 undercutting layer should solve this problem.

4.2.3 Wire bonding

Once the fabrication process is completed, the graphene Hall bar or graphlocon transistor is electrically tested with a probe station. The best devices are cut from the processed wafer and placed on a chip carrier with 14 electrical pins. The metal electrodes of the device are wire-bonded to the pads of the chip carrier with aluminum wires as shown in Fig. 4.9. The gate of the device can be contacted to one of the pads of the chip carrier by dropping a small blob of indium which connects the edge of the Si chip to one of the carrier pad.

The fabrication processes described above typically have a yield of around 30%. Out of the 12 devices that can usually fit in a chip carrier, 3 to 4 of them work (no gate leaking, good ohmic contacts) and 2 can be wire-bonded. The electronic transport properties of these devices are now ready to be investigated.

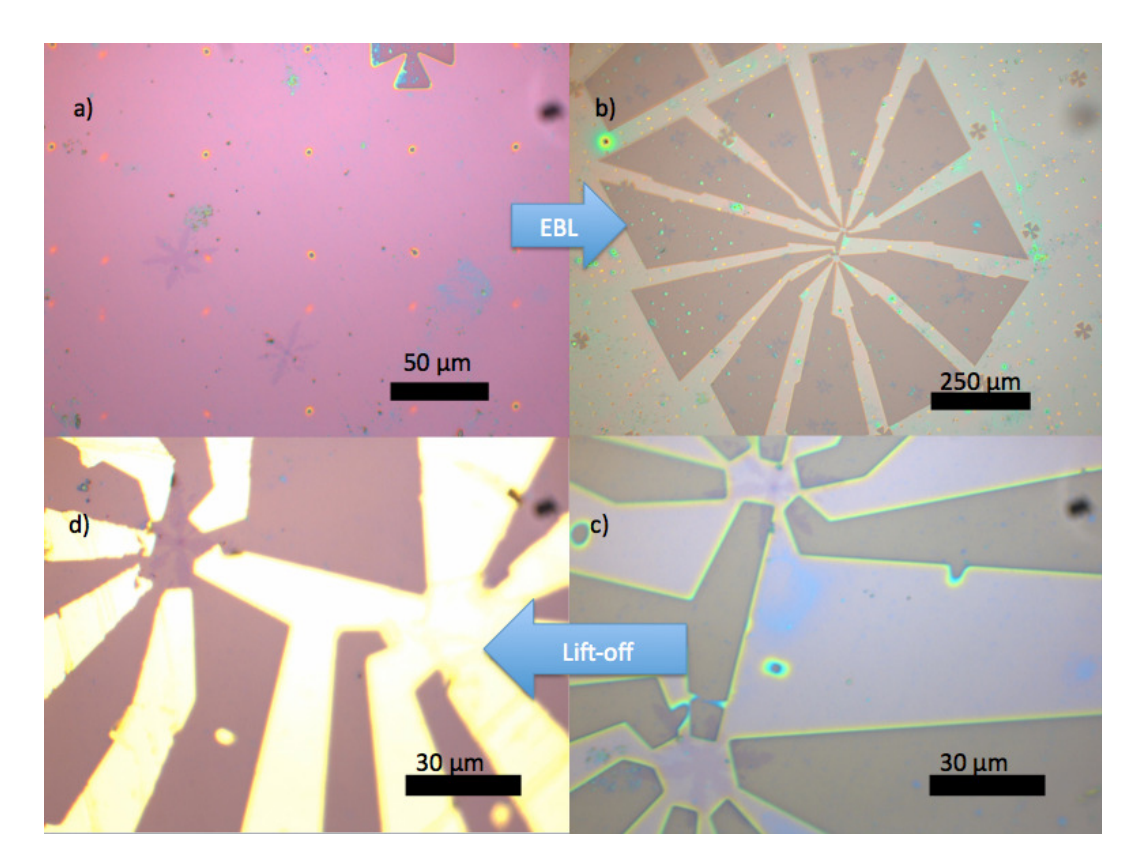


Figure 4.8: Optical images of the fabrication process of two graphlocon transistors. The graphlocons are located under a patterned resist coating (a) and pads are drawn by EBL (b), with each pad connected to a graphlocon branch. d) Resulting device after metal deposition and lift-off.

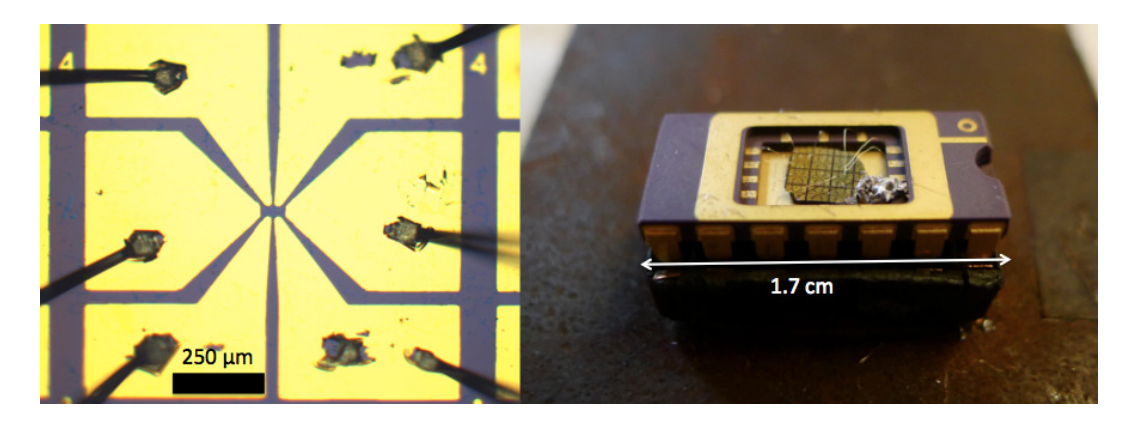


Figure 4.9: Wire-bonded graphene device. Left: Full view of a graphene Hall bar (graphene channel in the middle). Right: Photo of a wire-bonded graphene device on a chip carrier.

Transport Measurements

With a graphene FET in hand, many questions regarding the electronic properties of CVD-grown graphene can be addressed. First, we wish to know what the carrier mobility μ of the sample is. Is it comparable to other values reported in the literature? What is the effect of temperature on the mobility? At the same time, one can assess the cleanliness of the sample by determining the residual charge carriers n_0 possibly induced by charged impurities n_{imp} on the sample or in the SiO₂ substrate. Is the sample clean and homogeneous or is it dominated by defects and impurities? Second, we want to observe the effect of applying a magnetic field to the device. Does it exhibit the characteristic features of the quantum Hall effect? What is the Hall charge density n_H and how does it compare to the charge densities extracted previously? Finally, we wish to study the transport properties when the charge carriers are in the phase-coherent regime, which can be achieved at very low temperature. Can weak localisation be measured? If so, how does it compare to large samples and what is the dominant scattering mechanism?

We will here try to address all these questions by analysing the electrical measurements performed on three graphene devices in a dilution refrigerator. But first, we describe the experimental setup and the measurement techniques we employed.

5.1 Experimental method

5.1.1 Measurement setup

In this experiment, we investigated two Hall bar devices and one graphlocon transistor. These samples were mounted on the dip-sockets of our dilution refrigerator (Leiden Cryogenics, DRS 1000). This cryogenic apparatus exploits the thermodynamics of a He-3 and He-4 mixture to cool samples down to 5 mK. Electrical measurements were performed at room temperature and during the cool down process at 77 K (liquid nitrogen), 4 K (liquid helium) and 100 mK (lowest temperature reached). The dilution refrigerator is equipped with a superconducting magnet which can apply a B-field up to 9 T perpendicularly to the samples. The magnitude of the B-field can be varied using a power supply which is controlled by a LabVIEW program.

Our experimental setup for measuring the electrical resistance is shown in Fig. 5.1. Three Keithley source-meters (model 2400) are employed to apply a DC gate voltage, induce a DC current and measure a DC voltage in various electrical configurations. The configuration shown in Fig. 5.1 allows the measurement of R_{XX} . The gate-voltage Keithley can output voltage from -40 to 40 V, so when higher voltage is needed, a second Keithey was connected in series, thus doubling the voltage range. The drain-source current used typically varied between 1 and 40 μ A. Note that in this setup the ground is floating.

The gate-voltage sweep measurements were controlled and performed using the LabTracer Test Integration Software (Keithley) which was connected to the Keithley source-meters by a GPIB/optic fiber communication system. Typically, the gate voltage was swept from -40 to 40 V with a sweep delay of 100 ms while the induced current, 2-terminal voltage (voltage read by the current source) and 4-terminal voltage were measured. These sweeps were performed at various fixed magnetic fields (0, 4, 6, 7, 8 and 8.5 T). In addition to these gate-voltage sweeps, we measured the resistance as function of the magnetic field for fixed values of gate voltages (0, 38 and 47 V).

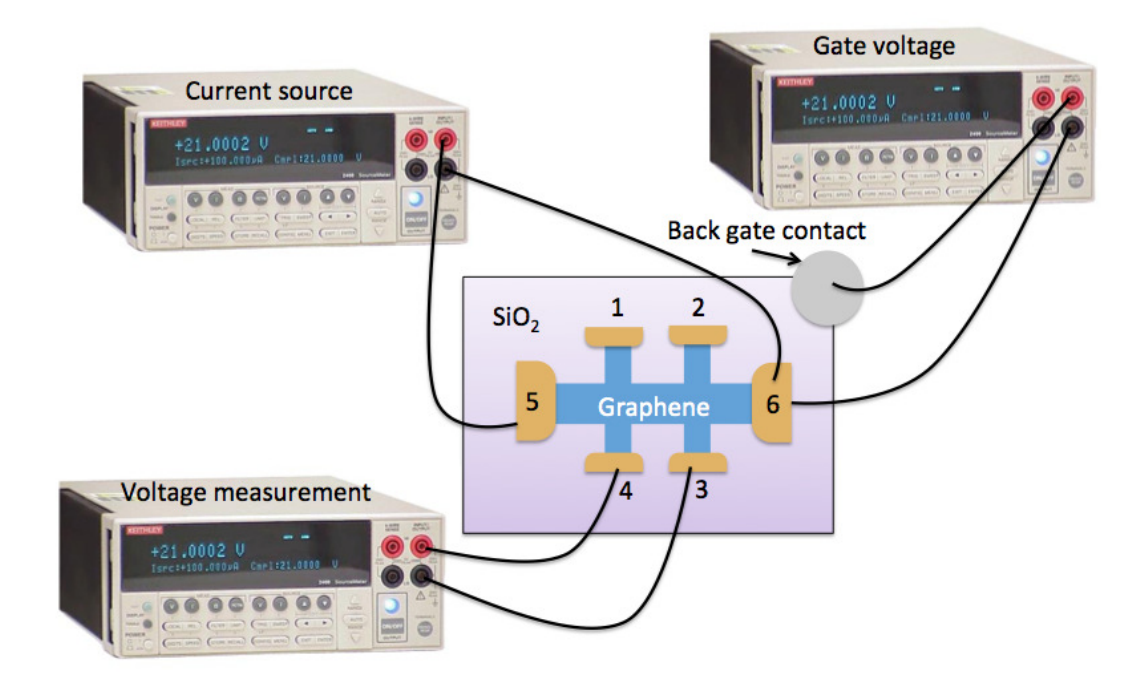


Figure 5.1: Schematic of the electrical measurement setup for a Hall bar device.

5.1.2 Measurement Techniques

During this experiment, we performed two types of 4-terminal measurements. The first type, presented in Section 2.3, takes advantage of the Hall bar configuration in determining the tensorial resistivity. When no B-field is applied, ρ_{XX} corresponds to the sheet resistance R_S . This quantity can also be determined for a homogeneous sample of any arbitrary shape using the Van der Pauw (VDP) method. For this technique, two complementary 4-terminal resistances must be measured, for example $R_{12,34}$ (= V_{12}/I_z 34) and $R_{23,41}$ using the numbering in Fig. 5.1. The sheet resistance R_S is related to these two resistances by the following formula

$$e^{-\pi R_{12,34}/R_S} + e^{-\pi R_{23,41}/R_S} = 1 (5.1)$$

Thus, by measuring two sets of resistances and solving this equation numerically, the sheet resistance can be determined. To obtain the Hall resistance R_{XY} in the VDP configuration (at B=0), a current is induced between two opposite contacts (ex: 1 and 3 in Fig. 5.1) and the voltage on the two other opposite contacts (ex: 2 and

4) is measured. Since the channel is not square (L/W=3), the measured resistance contains contributions from both R_{XX} and R_{XY} . However, one expects R_{XX} to be independent of the sign of the field and R_{XY} to be antisymmetric with respect to the field. Thus, to separate these quantities, it is common to perform symmetrization and antisymmetrization averaging over the magnetic field:

$$R_{XX}^{sym} = \frac{1}{2} [R_{XX}(B) + R_{XX}(-B)] \qquad R_{XY}^{asym} = \frac{1}{2} [R_{XY}(B) - R_{XY}(-B)]$$
 (5.2)

5.2 Results and Discussion

In the following section, we focus on the Hall bar sample on which we performed most measurements. The graphlocon sample was measured with a 2-terminal configuration down to 100 mK but one of the contacts stopped working which prevented us from measuring its magnetic field dependence.

5.2.1 Field Effect Mobility

Based on the theory presented in Chapter 2, mobility can be extracted using two different methods. First, by measuring the field effect resistivity and assuming a certain gate voltage dependence of the charge density $n(V_G)$, one can determine the field effect mobility. This technique is the most commonly employed because it involves simple and straightforward measurements. The second method requires an external magnetic field to measure the Hall carrier density which, combined to the measured resistivity, yields the Hall mobility.

For both techniques, an accurate measurement of the sheet resistance is desired. Fig. 5.2a shows the gate-voltage dependence of the longitudinal resistivity ρ_{XX} (V_{XX}/I_{56}) measured for both $V_{XX}=V_{12}$ and V_{34} at 4 and 77 K. In a homogeneous sample, the two voltage configurations should yield the same resistivity value, which is clearly not the case in Fig. 5.2a. This inhomogeneity introduces a large error on the value of sheet resistance R_S , which we assume to be the average of the two ρ_{XX} . In this case, the relative error associated with R_S is typically 33%. Throughout our analysis, this

error will dominate all other error sources, thus considerably limiting the precision of the extracted values. As the Hall bar was cooled down to base temperature (100 mK), contact 5 stopped working and we were forced to use the VDP method to measure the sheet resistance. Fig. 5.2b shows the gate-voltage dependence of two 4-terminal resistances and the sheet resistance calculated using Eq. (5.1).

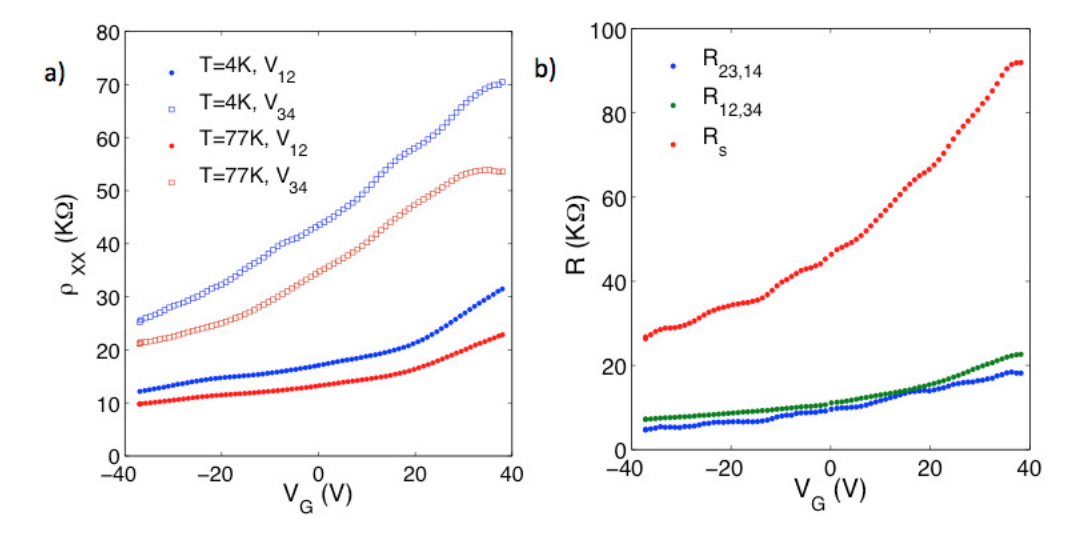


Figure 5.2: Measurement of the gate-dependent sheet resistance R_S . a) At 4, 77 and 300 K (not shown) R_S is the average of ρ_{XX} in the two voltage configurations. b) At 100 mK, R_S is determined with the VDP method for each gate voltage.

The sheet resistance obtained by VDP at 100 mK and those corresponding to the averaged ρ_{XX} at 300, 77 and 4 K are all presented in Fig. 5.3a. It can be seen that the resistance clearly increases as the temperature drops. This behavior has been observed for CVD graphene [111], whereas the opposite effect is reported for exfoliated graphene [10, 49]. We can attribute this difference to the fact that CVD graphene contains many more defects than the pristine exfoliated one. As we will discuss in the next section, for these disordered systems, charge carriers become localized at low temperature, which leads to a significant increase of the resistance. We often notice that the VDP method seems to overestimate the sheet resistance, hence R_S at 100 mK might be lower than what is presented in Fig. 5.3a. Nevertheless, the error induced by VDP is relatively small compared to the one induced by the sample inhomogeneity.

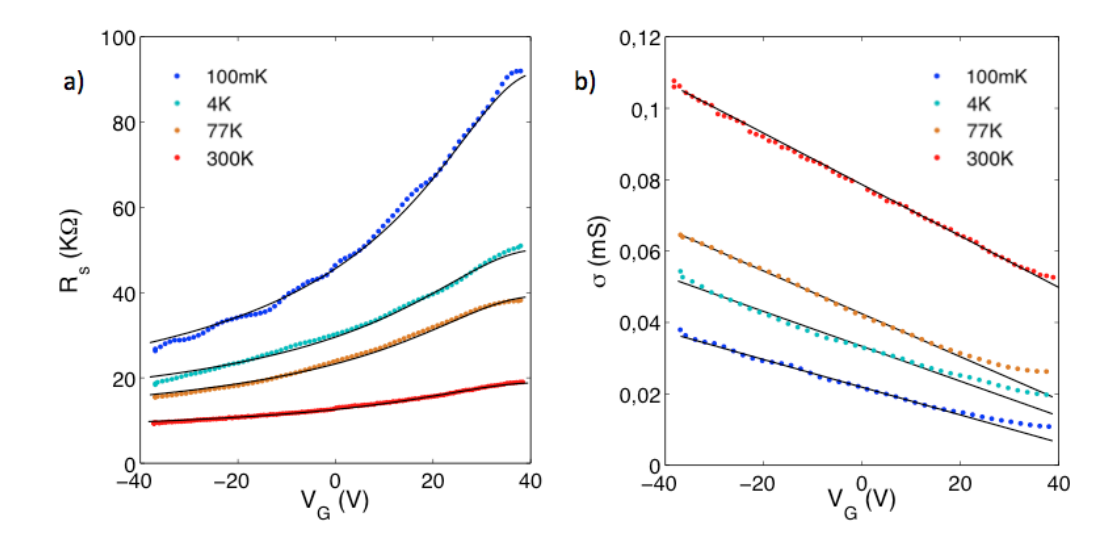


Figure 5.3: Fit of gate-dependent sheet resistance R_S at different temperatures using the models proposed by a) Dorgan *et al.* [42] and b) Adams *et al.* [50]. Experimental curves are represented by color dots and fitting curves, by solid lines.

By fitting the gate-voltage dependence of R_S with two models presented in Chapter 2, we extracted the field-effect mobilities and other parameters shown in Table 5.1. In both cases, the fits were performed by assuming that the capacitance per unit area of the dielectric C_{ox} is 11 nF/cm² and the Dirac point V_0 is 42 V. This assumption, as we will see with later, was confirmed by pushing the gate voltage up to 80V.

The first model we examined is the one of Dorgan *et al.* [42]. The fitting curves drawn with solid lines in Fig. 5.3a were obtained by combining Eq. (2.6) and Eq. (2.10), which gives the equation

$$R_S = \frac{L}{W} \frac{1}{e\mu\sqrt{n_{VG}^2 + 4n_0^2}} + R_a \tag{5.3}$$

Dorgan's model does not predict the additional term R_a , but we found that it was often impossible to obtain a valid fit without including this parameter. The origin of this term was not investigated but it could be due to the inhomogeneity of our sample. That being said, the values of R_a found are low compared to the contact resistance R_C that can be estimated by taking the difference between 4T and 2T resistance ($R_C \sim 40 \text{ K}\Omega$).

Dorgan's model allows to extract both field-effect mobility and the residual carrier density n_0 . At the outset, we note the very low mobility of our sample, even at room temperature. Compared to the best mobilities reported for CVD-grown graphene (Table 2.1), ours is approximately one order of magnitude lower. However, they are comparable with values reported for inhomogeneous CVD graphene [56] and purposely disordered exfoliated graphene [112, 113]. This is consistent with our previous observations. The very small width of the channel might also be responsible for the low mobility of our sample. It is worth repeating that the errors on the values presented in Table 5.1 are largely dominated by the inhomogeneity of the sample, yielding a relative error of approximately 33%. It can also be seen that the mobility decreases as temperature decreases, which again can be attributed to the emergence of localization. In contrast, the residual carrier density n_0 was found to be more or less independent of temperature, with an average of $(1.6\pm0.5)\times10^{12}~\mathrm{cm^{-2}}$. This value is comparable to those found in the literature for as prepared CVD samples [58], i.e. without post-cleaning process. It is, however, one order of magnitude larger than most pristine exfoliated graphene devices. According to Eq. (2.6), the residual carrier density comes from thermally generated carriers (n_{th}) and electrostatic spatial inhomogeneities (n^*) . The value of n_0 we obtained is so high that the thermal effect is negligible. Therefore, $n^* \approx 2n_0 = (3.2\pm1) \times 10^{12} \text{ cm}^{-2}$.

	T (K)	300	77	4	0.1
Dorgan's model [42]	$V_0(V)$	42	42	42	42
	$\mu (\mathrm{cm^2/Vs})$	460	110	100	50
	$n_0 \ (10^{12} \mathrm{cm}^{-2})$	1.2	1.8	1.6	1.5
	$R_a (K\Omega)$	9	7	4	7
Adam's model [50]	$\mu (\mathrm{cm^2/Vs})$	60	50	40	30
	$n_{imp} (10^{12} \text{cm}^{-2})$	1.7	2.0	2.5	3.1
	$\sigma_{res} (10^{-5} \mathrm{S})$	5	2	1	55

Table 5.1: Parameters extracted from the fits of the field-effect curves Fig. 5.3. $V_0=42~V$ was assumed for both models.

We further investigated our measurements with a second model proposed by Adam et al. [50] which predicts a linear relation between the conductivity and gate voltage when $n_{VG} > n = n_0$. According to Chen et al. [46], a residual conductivity term σ_{res} may be added to Eq. (2.9), though its physical significance is not well defined. Using Eq. (2.5) and the values of n_0 found with the first model, we fit Adam's model on our measurements as shown in Table 5.1. Away from the Dirac point, the conductivity indeed appears to scale linearly with V_G . In Table 5.1, values of the two fitting parameters, n_{imp} and σ_{res} , are presented. According to this model, the mobility can be calculated from n_{imp} . We immediately notice not only that the values of μ are much smaller for this model than the previous one, but that they also decrease with temperature. As we mentioned in Chapter 2, n_0 is approximately equal to $0.2n_{imp} \approx (4\pm1.3)\times10^{12}~{\rm cm}^{-2}$ which is in fairly good agreement with the results obtained from the first model. However, the very irregular values of residual conductivities clearly indicates a deficiency in the model. This flaw might come from the inaccurate modeling of the gate-voltage dependence of charge carriers. Indeed, this model does not take into account the residual carrier density when $n > n_0$. For this reason we employed Dorgan's model to study 2-terminal measurements, with $R_a =$ R_C in this case.

By extending the gate voltage up to 80 V, we were able to clearly observe the Dirac peak V_0 for the 2T resistance R_{12} at 100 mK (a). Knowing that charge carriers are mainly holes for $V_G < V_0$ and electrons for $V_G > V_0$, the mobility for both carriers can be extracted separately. The fitting parameters found using Dorgan's model are presented in Fig. 5.4. However, in the case of 2T measurements, the extracted mobility must be divided by the aspect ratio (W/L) which is unknown for this configuration but, certainly smaller than 1. This indicates that the graphene region probed in this configuration is much better quality, with a mobility higher than 100 cm²/Vs for both holes and electrons. The residual charge carrier densities extracted are also significantly lower than those of the 4T measurements. This is congruous with the fact that R_{XX} measured with contacts 1 and 2 is much lower than the one measured

with contacts 3 and 4 (Fig. 5.2a). Once again, the inhomogeneity of our sample manifests itself. We also note that the extracted contact resistance R_C is of the same order magnitude as the one we previously found by taking the difference between 4T and 2T measurements.

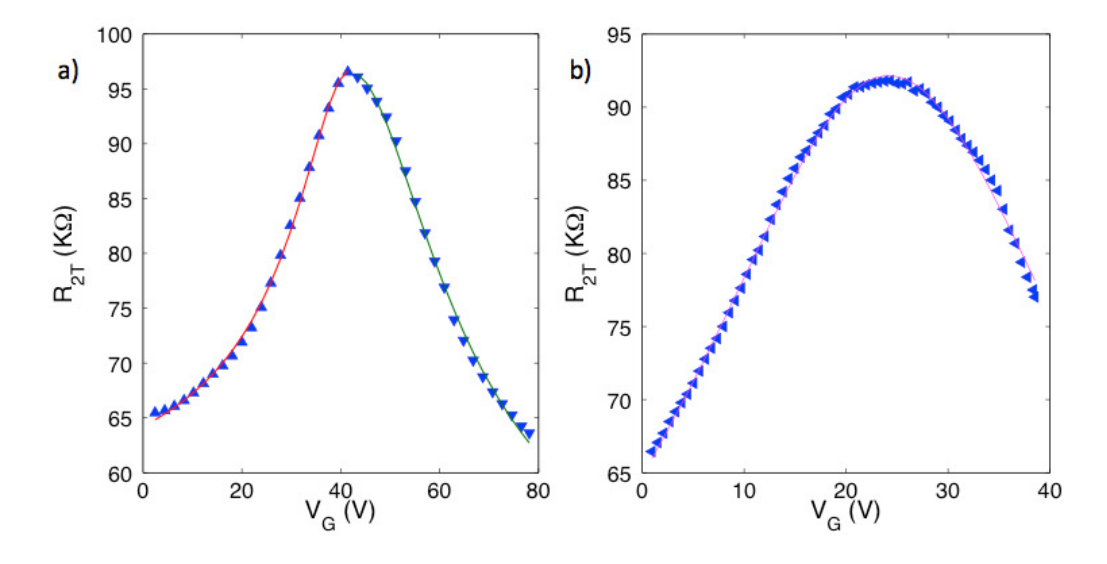


Figure 5.4: Fit of gate-dependent 2-terminal resistance for a) the Hall bar device between contacts 1 and 2 and b) the graphlocon transistor. Experimental curves are represented by blue triangles and fitting curves, by solid lines. Red and green curves in a) correspond to hole and electron charge carriers, respectively.

Finally, we performed a similar analysis for the 2T measurements of the graphlocon sample at 100 mK. The field effect resistance presented in Fig. 5.4b displays a Dirac peak at 24 V and the fit over the entire curve is plotted with a solid line. The fitting parameters shown in Table 5.2 are quite similar to those found for the Hall bar. Here again, the mobility is divided by an unknown aspect ratio factor which is surely smaller than 1. We also note that the contact resistance R_C of the graphlocon is considerably smaller than the one of the Hall bar which might be due the different fabrication technique (no plasma etching).

5.2.2 Magnetotransport

A complementary method for evaluating the charge carrier density and mobility in a sample consists of measuring the B-field dependence of the Hall resistance. Such

	HB hole	HB electron	Graphlocon
V_0 (V)	42	42	24
$\mu L/W (cm^2/Vs)$	200	100	60
$n_0 \ (10^{12} \mathrm{cm}^{-2})$	0.7	1.1	1.4
$R_C (K\Omega)$	54	39	16

Table 5.2: Parameters extracted from the fits of the field-effect curves of Fig. 5.4 (HB= Hall bar)

a measurement was performed on the Hall bar by flowing current between contacts 2 and 4 and measuring the voltage between contacts 1 and 3 while sweeping the magnetic field from -6 to 6 T, at $V_G = 0$ V. Using Eq. (5.2), we found that the asymmetric contribution of the Hall resistance varies linearly with the magnetic field (Fig. 5.5a). This slope, which corresponds to the Hall coefficient R_H , shows no clear indication of quantum Hall plateaus. By fitting R_{XY}^{asym} with a straight line, we obtained the Hall density $n_H = 1/eR_H = (6.25\pm0.04)\times10^{12} \text{cm}^{-2}$. This value corresponds to the difference between the electron and hole density at $V_G = 0$ V. In comparison, Eq. (2.5) predicts that $p - n = (3\pm1)\times10^{12} \text{cm}^{-2}$, which is close to the measured Hall density. The Hall mobility can be computed simply by $\mu = R_H/\rho_{XX} = 30\pm10 \text{ cm}^2/\text{Vs}$. This value is in good agreement with the field-effect mobility extracted with both models.

As discussed in Section 2.3, localization effects which can be detected in magnetoresistance (MR) measurements are good indicators of the presence of disorder in electronic systems. Depending on the amount of disorder, these effects vary from weak to strong localization, with an expected transition between these two regimes when $R_S=h/e^2$. To explore this quantum phenomenon, we measured the B-field dependence of R_{XX} in a VDP configuration (V_{34}/I_{12}) at 100 mK and extracted the R_{XX}^{sym} component using Eq. (5.2). In Fig. 5.5b, the raw R_{XX} curve as well as its symmetric and asymmetric components are shown for the sweep at $V_G=0$ V. The asymmetric contribution appears to be very small compared to the symmetric component since our contacts are lithographically well-defined. Most remarkably, the resistance drops by more for than 20% at 6T. This can be clearly seen in Fig. 5.6 where we also plotted

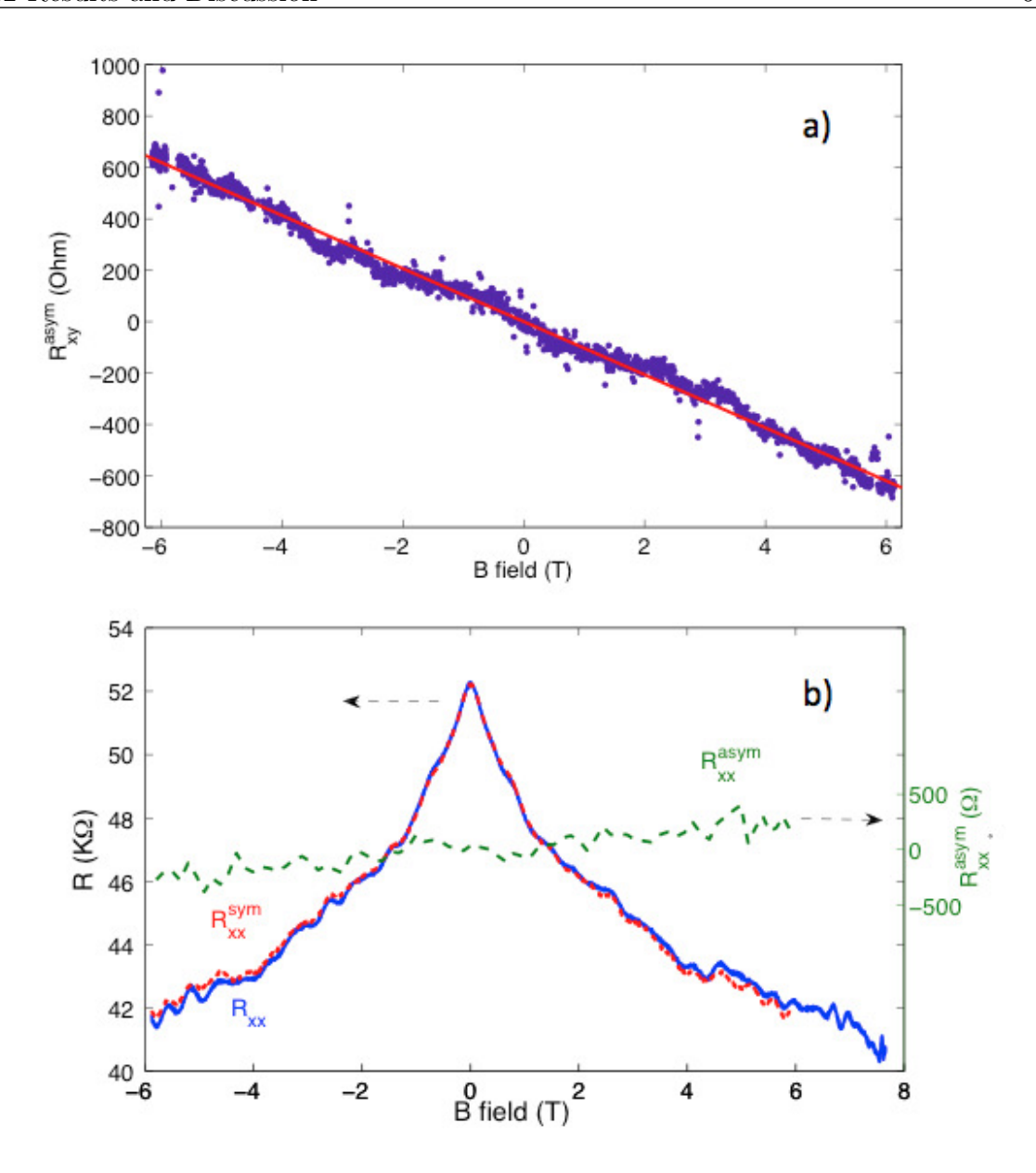


Figure 5.5: Magnetoresistance of the Hall bar at 100 mK. a) Asymmetric component of the Hall resistance (R_{XY}) as a function of B. The solid red line corresponds to the linear fit. B) B-field dependence of R_{XX} and its symmetric and asymmetric components.

the normalized MR at $V_G = 39$ V, close to the Dirac point. Such large MR (and even larger ones) was reported by Hong *et al.* [113] who studied weak and strong localization in fluorinated graphene.

We tried to fit these two curves with Eq. (2.12) proposed by McCann *et al.* for weak localization (dotted lines in Fig. 5.6), but we were unable to determine B_i and

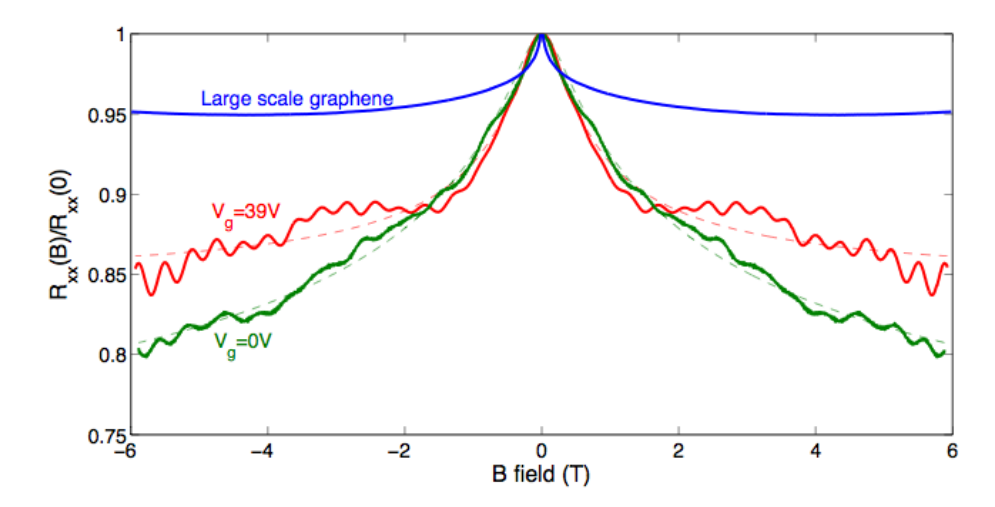


Figure 5.6: Normalized MR of sub-micron Hall bar (red and green curves) and a 1.5 mm size graphene sample (2T resistance of the microwave sample, blue curve). The green and red dotted lines are fits from McCanns model [62].

 B_{\star} properly. Indeed, the uncertainties associated with those fitting parameters were excessively large. This clearly indicates that McCanns model is not suitable for such large MR, and suggests that charge carriers are strongly localized. Nevertheless, the value of B_{ϕ} was determined with a low relative uncertainty (10%). Converted in dephasing scattering time τ_{ϕ} , we obtained 2 and 4 ps for the measurements at $V_G = 0$ V and 39 V, respectively. These values can be associated with a dephasing length L_{ϕ} assuming that transport is diffusive so that $L_{\phi}=\nu_F\sqrt{\tau\tau_{\phi}/2}$. For both gate voltage values, we calculated $L_{\phi}=25\pm3$ nm, which is about one order of magnitude smaller than the width of the Hall bar.

It is worth pointing out that McCann's model does not take into account the finite size of the sample. Yet, we know that the width of the Hall bar is comparable to the dephasing length of large graphene samples previously measured in our lab [114]. To look more closely into this possible size effect, we compare, in Fig. 5.6, the MR of our small scale device to the one of a typical large graphene sample. The magnitude of the MR appears to be much smaller and the localization peak, much more narrow for the large sample and in this case, McCann's WL theory can be used to describe the MR. This suggests that the dimension of the sample might play

a role in the localization effects seen in the Hall bar device. According to Datta [115], a phase-coherent conductor whose length is comparable to the localization length has a resistance greater than $\sim h/2e^2$ (12.5 k Ω). Such conductor is said to be in the regime of strong localization, which seems to be the case of our Hall bar. McCann's model fails to describe the strong localization regime. Therefore, the dephasing scattering time and length values extracted above most be considered with prudence. Notwithstanding this ambiguity, the analysis of the Hall bar MR reveals that the graphene sample is highly disordered, which is in line with our previous observations of low mobility and anisotropic resistance.

High Frequency Measurements

Due to its high mobility, graphene was proposed and demonstrated to be a promising material for high-speed electronic devices such as high-frequency transistors [14, 15], microwave switches [116], frequency multipliers [18] and mixers [117]. However, until very recently, very few studies focused on measuring and understanding the intrinsic response of graphene to microwave frequencies [118, 119], which is crucial in order to use graphene for fast electronic applications. This lack of attention can partly be explained by the unsuitability of small exfoliated samples for long-wavelength measurements, and by the experimental difficulties inherent to extracting significant broadband spectral information in this frequency range [120]. Recently, the microwave and terahertz impedance of large CVD-grown graphene was reported at room [121] and low [120] temperature, but only a weak, linear frequency dependence was found. In comparison, similar studies for a conventional two-dimensional electron gas (2DEG) reveal a wealth of exotic non-linear phenomena, such as microwave induced resistance oscillations (MIRO) [122] and edge-magnetoplamons (EMP) [123]. Analogous effects have been predicted for graphene [63] but experiments have yet to show these effects in the GHz frequency range. Our goal for this section of our masters thesis was therefore to search for these non-linear phenomena in graphene by exploring new phase spaces at high frequency, low temperature and high magnetic field.

Our approach in achieving this goal consisted in first probing the DC and AC response of graphene when irradiated by intense high frequencies at liquid nitrogen temperature. We further investigated the high frequency response of graphene by

inserting a sample in the dilution refrigerator and applying, in addition to microwaves, a magnetic field from -2 to 2 T at 100 mK.

6.1 Experimental Setup

6.1.1 4-Kelvin Microwave Probe

To implement this approach, we designed, with the great help of Richard Talbot, a probe able to simultaneously perform DC and high frequency measurements at cryogenic temperatures and high magnetic field. The high frequencies are produced and analyzed by an Anritsu, 37347A vector network analyser (VNA) which has a dynamic range of 100 dB and a frequency range of 40 MHz to 20 GHz. The VNA can output a power as high as 1 mW and measure the four scattering parameters (S-parameters) S_{ij} between two ports, where the source port is denoted by j and the receptor port is given by i. In this thesis, we focus on the parameter S_{21} corresponding to the transmission through the probe and the graphene device from port 1 to port 2. Measurements can be done either by sweeping the frequencies over a definite range or by selecting a single frequency (continuous wave mode).

As illustrated by Fig. 6.1, the VNA is connected to a 4-Kelvin microwave probe via coaxial cables with 2.4 mm connectors. The probe is also equipped with DC wires which are typically connected to Keithley source-meters. Vacuum inside the can of the probe (see Fig. 6.2), with pressure as low as 10^{-6} mBar, can be achieved by connecting the vacuum port to a diffusion pump. In order to accelerate the cool-down process an exchange gas (He) can be introduced in the probe through the vacuum port. The probe was designed to fit inside the He-3 cryostat available in our lab which contains a superconducting magnet. However, due to time constraints, we preferred using the dilution refrigerator to perform ultra-low temperature measurements instead of this cryostat. Nevertheless, this 4-K microwave probe was inserted in a liquid nitrogen bath to carry out measurements at 77 K.

In Fig. 6.2 we present the main features of the 4-K microwave probe and its end-piece. The probe consists of an insert, carrying the DC wires and coaxial cables.

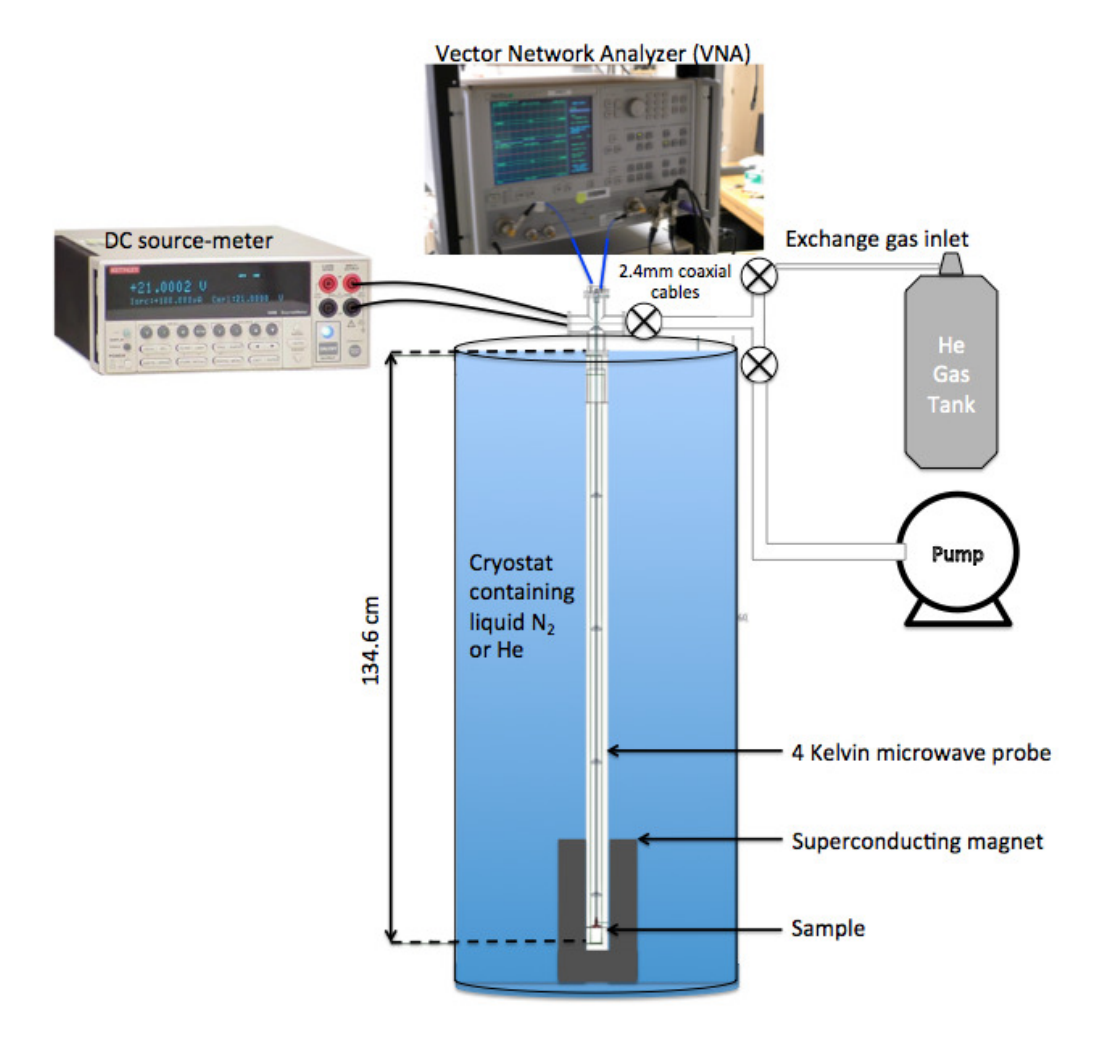


Figure 6.1: Schematic of the high frequency measurement setup using the 4-K microwave probe.

encompassed in a vacuum-tight can which can be loaded into the cryostat. The insert is made out of a stainless steel shaft fixed to a cross-shaped head sitting outside the cryostat. Two semi-rigid coaxial cables whose outer conductor is made of copper (UT-085C, Micro-coax) are fed through hermetic holes on top of the head. The DC wires connect to a 19-pin vacuum-thigh connector on a side opening of the head. The last opening serves as a vacuum port to which the pumping and gas exchange systems are connected.

Wires and coaxial cables go down the shaft across spacers employed to guide the insert inside the can and to insulate thermally the end of the probe. The probe end-piece is made of solid brass piece screwed to the extremity of the shaft. The

coaxial cables are connected to the end-piece by 2.4 mm connectors which have an uncovered central tip on their back. These tips provide a transition between the coaxial cables and the graphene high frequency device. A CERNOX temperature sensor (Cx-1050-AA, Lake Shore Cryotronics) is slotted into the brass piece and allows us to determine the temperature from 4 to 400 K by measuring its four-terminal resistance. To calibrate the sensor, we measured its resistance at 296 K and 77 K, and compared the values to the calibration curve of a similar sensor. Assuming that our sensor has the same calibration curve (up to a factor), we obtained the following fitting equation:

$$T(K) = 739.1 \exp(\frac{-T}{72.57}) + 103.1 \exp(\frac{-T}{691.08})$$
(6.1)

where T is the temperature in Kelvin and R is the thermometer resistance in Ω . A cartridge heater is inserted on the opposite side of the brass piece and provides 15 W at 24 V. The two DC wires of the heater as well as the four DC wires of the temperature sensor are soldered to the 19-pin connector.

6.1.2 High Frequency Graphene Device

Design

The 4-K microwave probe was specifically designed to hold and measure large samples with a flat sample-holding surface of 21.5 mm in diameter and 12 mm between the two microwave tips. To transmit the high frequency signal from the microwave tip to the graphene sample efficiently, we opted for a coplanar waveguide (CPW) geometry. The CPW was chosen over the microstrip because, as we will show later, the CPW allows for the 4-terminal DC measurement of the sample. A typical CPW consists of a central conducting strip flanked by two ground planes and another ground plane beneath a dielectric substrate of dielectric constant ϵ_r , as illustrated by Fig. 6.3.

Using a software called AppCAD, we optimized the geometrical parameters W and G for a 1 mm-thick glass (soda-lime glass) substrate and a 150 nm-thick metallic layer. To minimize the impedance mismatch and thus maximize the signal transmission

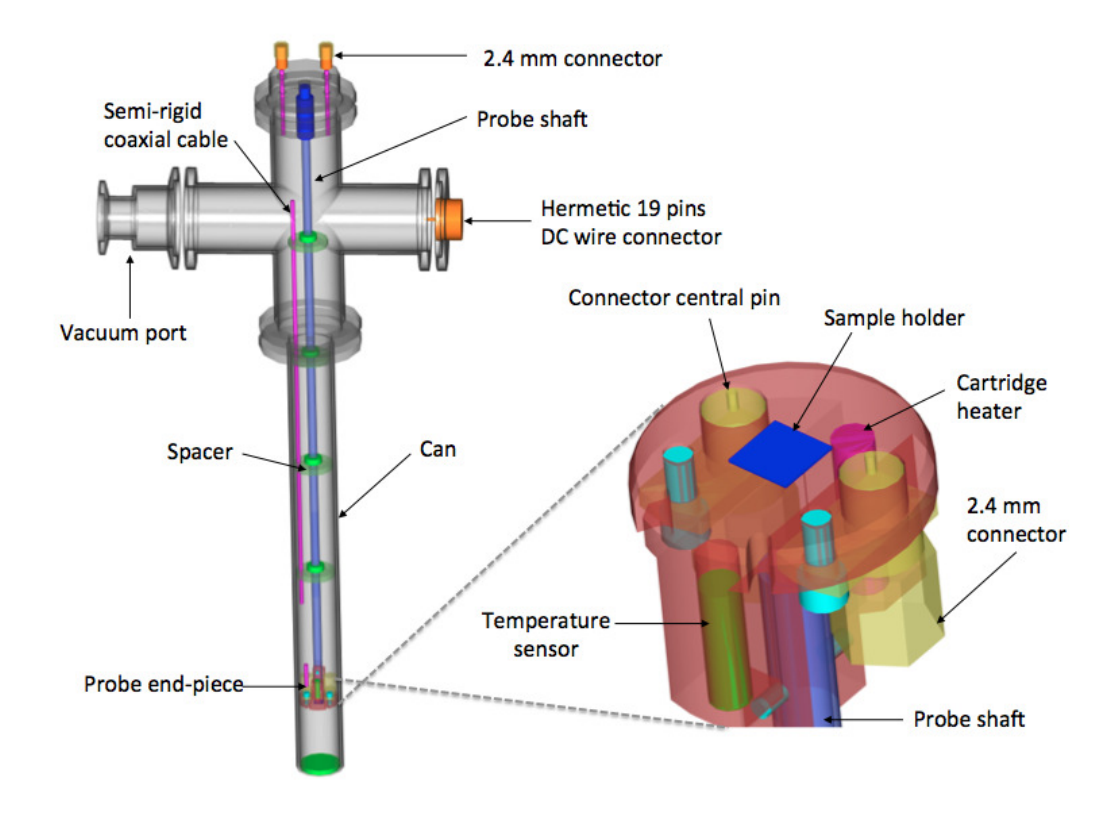


Figure 6.2: Schematic of the 4-K microwave probe (left) with a top view of the probe end-piece. Figure courtesy of R. Talbot.

through the CPW, we designed our device to have an impedance of 50 Ω like the rest of the microwave equipment. In general, a ratio W/G \sim 3 was found to yield such impedance. To compensate for possible miscalculations of the rather simplistic AppCAD software, we also designed CPWs with impedance of 40 and 60 Ω . The 5 designs which were printed on a lithography mask are presented in Table 6.1.

CPW number	$W (\mu m)$	$G(\mu m)$	$Z_0(\Omega)$
1	300	45	40
2	300	100	50
3	300	200	200
4	150	50	50
5	30	10	50

Table 6.1: Dimensions of the designed CPWs and their calculated impedance Z_0

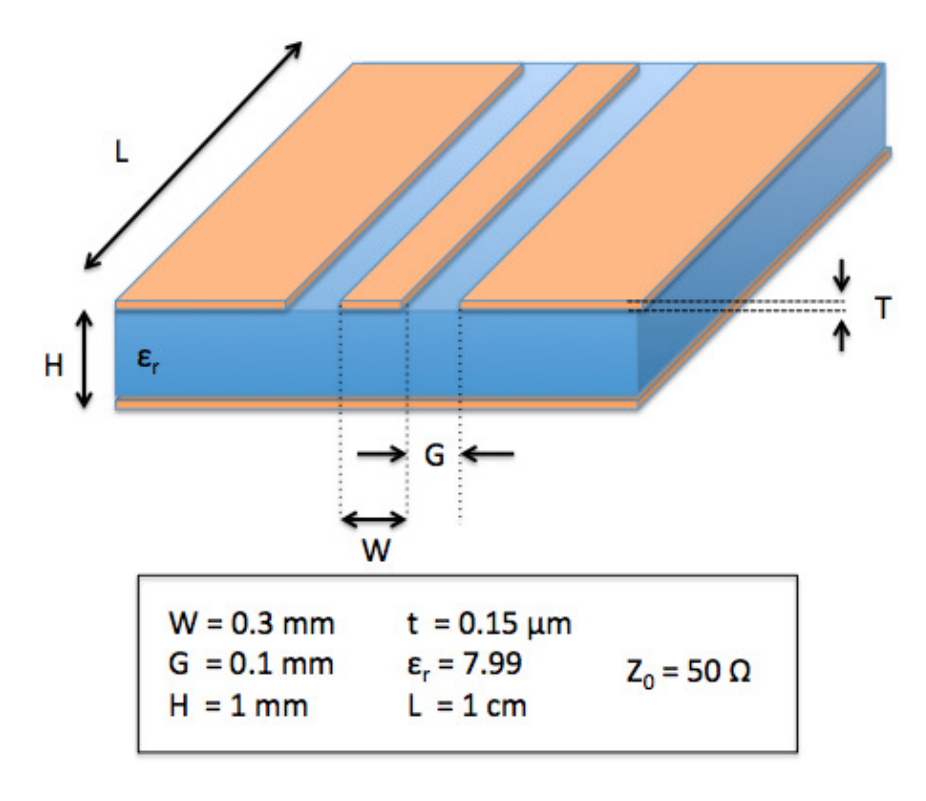


Figure 6.3: Schematic of a coplanar waveguide (CPW) as simulated by AppCAD. Dimensions corresponding to a 50 Ohm impedance on a soda-lime glass substrate are displayed in the box.

To probe the high frequency response of graphene, a graphene film is transferred onto the top of the CPW, as shown in Fig. 6.4. For each of the CPW designs presented in Table 6.1, 5 variants were made with different gap sizes in the middle of the central strip. One CPW configuration has no gap whereas the four others have a gap of 20, 100, 500 and 1500 μ m. This gap possibly provides better coupling between graphene and the electromagnetic field since the signal has to go through the graphene film to cross the gap.

Each CPW is given a length of 1.2 cm in order to fit between the two microwave tips. The connection between the tips and one of the CPW configurations is made by soldering a small drop of indium. To facilitate the soldering and avoid any short-contact between the ground planes and the central strip, the latter was widened on both ends, as shown on Fig. 6.4. In this figure, the second CPW configuration (gap = $20 \ \mu \text{m}$) is connected. DC wires can be soldered with tin/lead on every ground plane

in the desired configuration. In the configuration illustrated in Fig. 6.4, knowing the width of the graphene film allows us to estimate the sheet resistance. Two-terminal resistance between the two microwave tips can also be measured on the VNA. One advantage of this device design is that it allows for high frequency measurements with different gap sizes on the same graphene sample.

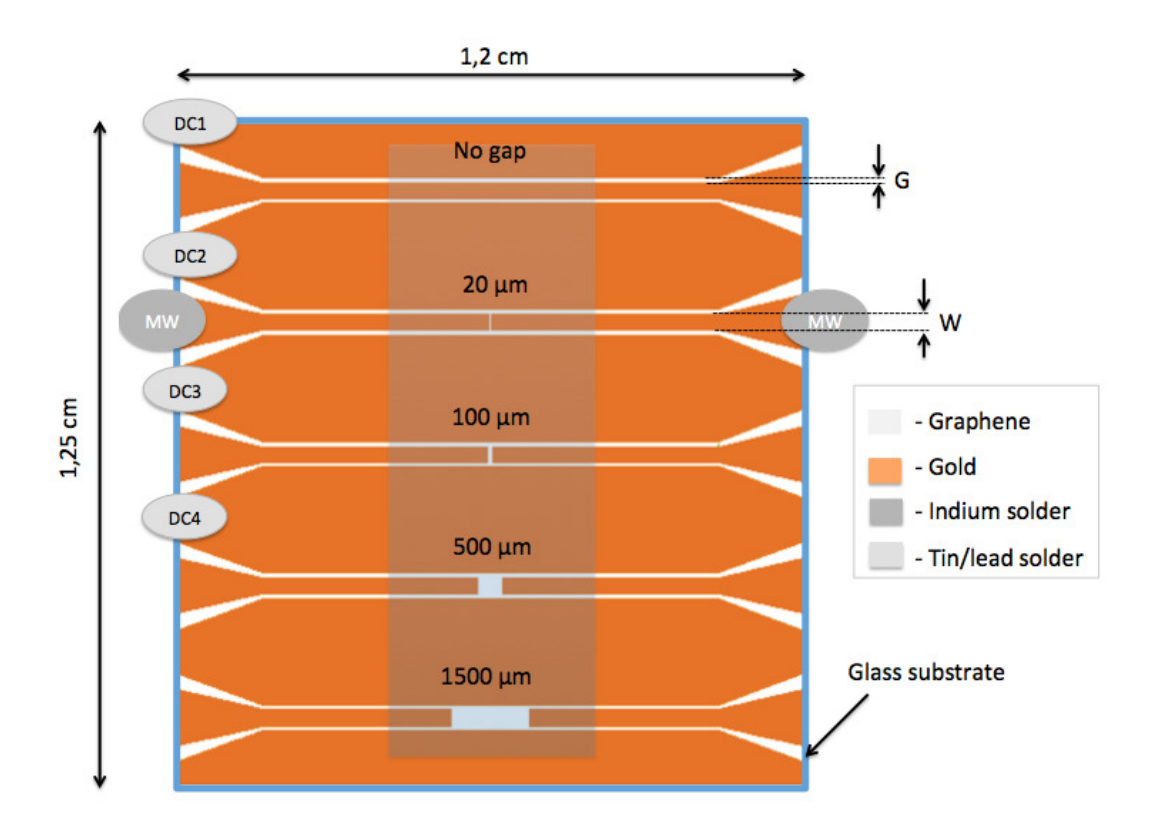


Figure 6.4: Schematic of a typical high frequency graphene device with 5 CPWs of different gap sizes. The graphene layer is deposited on top of the gold pads. Connections for the second CPW configuration (20 μ m gap) are displayed.

Fabrication

Our samples were produced by one-step photolithography on 3×2 -inch soda-lime glass (standard microscope glass) using the same recipe as the one described in Chapter 4 for the electrode deposition of the Hall bar. A metal film made of 10 nm of Ti and 150 nm of Au was deposited by e-beam evaporation and was followed by a lift-off. The resulting gold-plated glass is shown in Fig. 6.5a. This glass substrate was then cut

71

into 1.25×1.2 cm pieces with a diamond-cut pen and a graphene film was deposited in the middle of one of the pieces using the same transfer technique as the one presented in Chapter 4. One end of the DC wires was soldered to the gold ground planes with tin/lead and on the other end to a 4-pin low temperature connector (CMR/LM4), as shown in Fig. 6.5b. Lastly, the device was installed on the flat surface of the end-piece, between the two microwave tips. The desired CPW configuration was soldered with indium to the tips and the DC connector was inserted in one of the three available connectors. A picture of a sample mounted on the probe is shown in Fig. 6.5c.

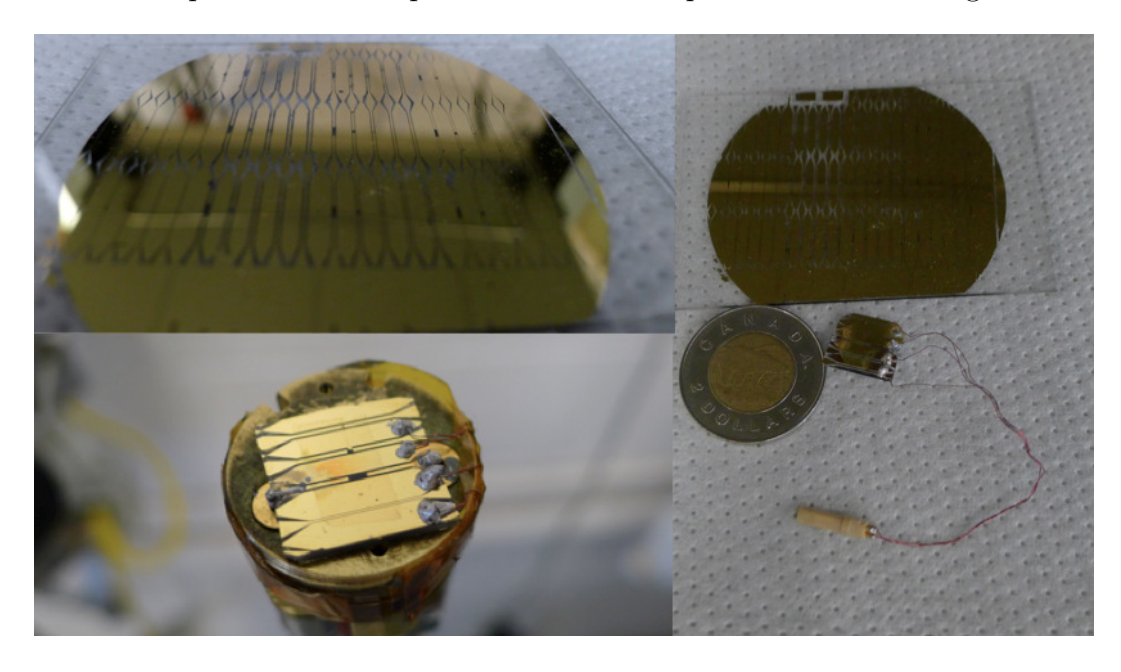


Figure 6.5: Pictures of the CPW graphene device. a) Array of CPWs on a glass plate after metal deposition and lift-off. a) High frequency device obtained after cutting the CPWs array (shown on top), soldering DC wires and transferring graphene. c) Top view of a sample mounted on the probe end-piece in the large gap (1500 μ m) configuration.

In order to characterize the performance of the probe and CPW design, we measured the transmission (S_{21}) and reflection (S_{11}) parameters of CPW3 without gap and prior to the deposition of graphene. It can be seen in Fig. 6.6a that the reflection and transmission parameters are of approximately the same magnitude at low frequency but that transmission becomes significantly lower at higher frequency. This suggests that at low frequency, a reasonably high intensity microwave field is applied to the CPW but that it might not be the case at high frequency. In general, the

transmission parameter shows a linear fall-off with frequency, which is characteristic of the loss in a coaxial cable. We noticed that inserting the probe in the can induce small transmission dips, especially at high frequency. Simple calculations suggest that these absorption peaks are due to the formation of standing waves between the end-piece and the bottom of the can. However, these unforeseen and undesirable features should not be too detrimental to our measurements since they are mostly located at high frequency where the transmission is low.

We can further characterize the probe by subtracting the contribution of the flexible coaxial cables that links the VNA to the probe. In Fig. 6.6b, the dotted line (S_{21} through) corresponds to the transmission through two consecutive flexible coaxial cables. We subtracted this curve from the total transmission curves of all five gap configurations of CPW3 and plotted the resulting ΔS_{21} . It can be seen that at low frequency, the CPW configurations with gap have a much weaker transmission than the continuous CPW. It also appears that the smaller the gap is, the weaker the transmission is. At higher frequency they all follow the same general linear fall-off.

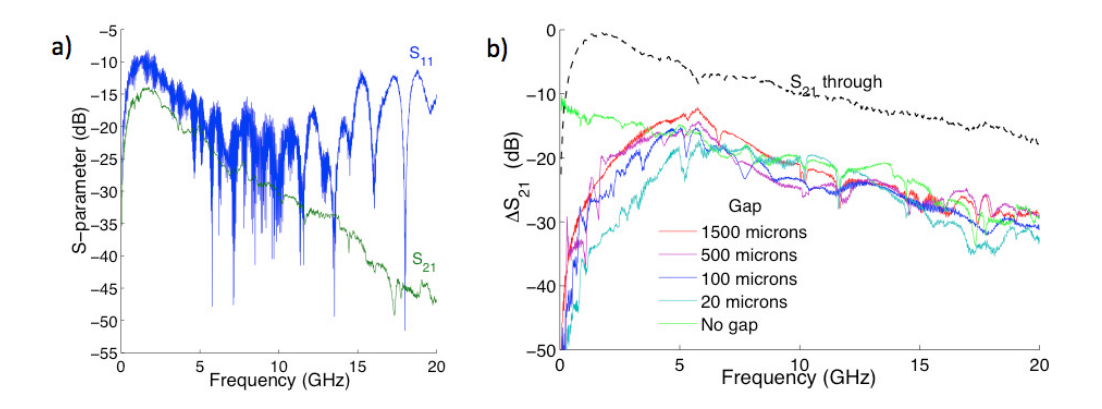


Figure 6.6: Characterization of the probe. a) Transmission (S_{21}) and reflection (S_{11}) spectra of CPW3 without gap. b) Transmission (ΔS_{21}) through the probe and CPW3 for all configurations (solid lines) compared to a through signal (dotted line).

6.2 Results and Discussion

Once the probe and CPW without graphene were characterized, a graphene layer was transferred onto the CPW as illustrated by Fig. 6.4. To achieve the transfer, the CPW had to be unsoldered from the microwave pins, and then resoldered. We noticed that the transmission spectrum changed significantly because of small changes in the microwave solders. This lack of reproducibility hindered the ability to measure the contribution of graphene. It is also worth mentioning that the pressure inside the can affects the resistance of graphene significantly. Variations up to 11% of the sheet resistance were measured when pumping down the probe. We ascribe this effect to the doping of the graphene layer by the surrounding gases, as it was previously demonstrated for graphene FET [124]. Therefore, to extract the contribution of graphene, we must compare measurements performed in the same temperature and pressure conditions.

6.2.1 High Frequency Transmission Through Graphene

We measured the transmission $S_{21}^{graphene}$ for sample CPW3 with graphene in various gap configurations at room temperature and pressure. The raw measurements are shown in the lower part of Fig. 6.7. To single out the effect of graphene, the transmission spectrum of CPW3 without graphene was subtracted from $S_{21}^{graphene}$ and the results are shown in the upper part of Fig. 6.7. It can be seen that in the configuration without gap, the graphene layer has hardly any effect on the transmission, with $\Delta S_{21} \sim 0$ dB. For configurations with gap, ΔS_{21} increases significantly at low frequency and decays at high frequency. The fluctuations in the spectrum are most likely due to changes induced by the re-soldering. The fact that ΔS_{21} falls to zero around 5 GHz suggests that graphene couples very weakly with the high frequencies in this geometry. This means that the frequency range available to probe the effect of microwaves on graphene with this CPW geometry is limited below 4 or 5 GHz. Measurements of other samples yield very similar results.

The general behavior of the transmission spectrum ΔS_{21} at low frequency can be

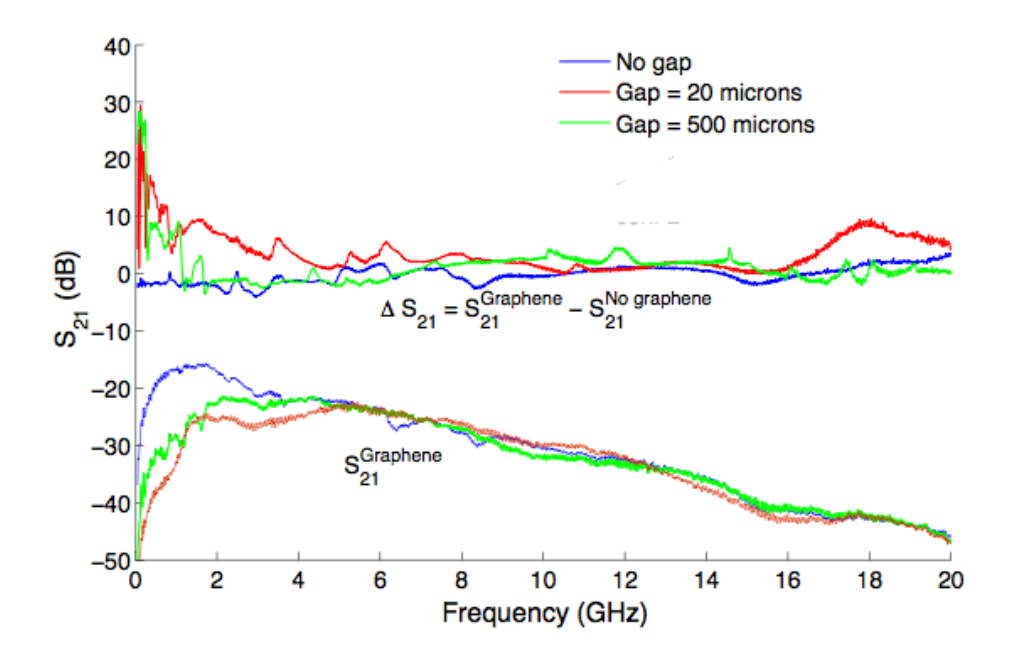


Figure 6.7: Contribution of graphene to the transmission spectrum. Total transmission spectrum ($S_{21}^{graphene}$) and transmission contribution of graphene (ΔS_{21}) in sample CPW3 for different gap configurations.

modeled by the characteristic impedance of a lossy transmission line which results from the telegrapher equation [125]

$$Z = \sqrt{\frac{R + j\omega L}{G + j\omega C}} \tag{6.2}$$

where R, L, G and C are respectively the resistance, inductance, shunt resistance and capacitance per unit length. If we consider the impedance of the CPW as the source impedance Z_0 and the graphene impedance as the load impdance Z_1 , the transmission of an incoming signal is given by the equation: $T=2Z_0/(Z_1+Z_0)$. In total, the transmitted wave encounters two graphene/CPW junctions, so the total transmission is $T_{tot} \approx |T|^2$ [123].

This model contains four fitting parameters (R, L, G and C) and is thus too ambiguous to extract any parameters with reasonable certainty. Some hypothesis must be made to reduce the number of fitting parameters. We thus supposed that L was negligible and that R and G were both geometrically related to the sheet resistance of graphene R_S . Furthermore, since the dimension of the graphene layer was not well defined, we estimated its length along the CPW to be about 2 mm. Fig. 6.8 shows the ΔS_{21} measured for CPW3 (Z_0 =60 Ω) with a gap of 20 μ m and the fit obtained with R_S =4 K Ω and C=6 nF/m. Considering the simplicity of the model, these fitting parameters are remarkably close to what can be found in the literature [121] and to our previous measurement of R_S for the Hall bar (\sim 10 K Ω). These values must, however, be considered with prudence since many assumptions were made to extract them. Nonetheless, this simple model provides some insight into the high frequency response of graphene in our CPW device. At low frequency, its resistive behavior dominates, whereas at high frequency, its capacitive response strongly reduces its impedance Z_1 .

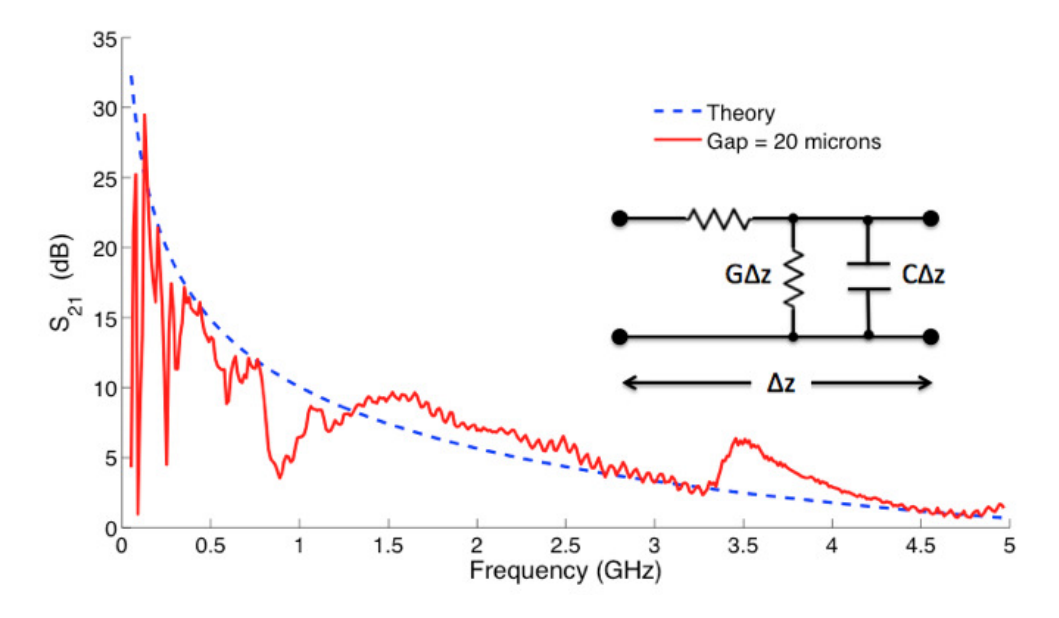


Figure 6.8: Measured (solid line) and calculated (dotted line) transmission through graphene at low frequency for sample CPW3 with a gap of 20 μ m. The electrical model employed for the calculation is shown.

6.2.2 Frequency-dependent DC Resistance

As a first approach to detect the effect of high frequency on graphene, we measured the DC resistance as a function of the applied frequency. Experimentally, this was done by selecting a frequency in the continuous wave mode and measuring accurately, i.e. with a long integration time, the DC resistance in 4T or 2T configuration, and repeating this process for the next frequency. Fig. 6.9 shows the results of such measurements performed on CPW2 (gap=500 μ m) at 300 and 77 K for three values of power attenuation (0, -10 and -20 dB). The 4T resistance (R=V₂₃/I₁₄, in Fig. 6.4) was measured while sweeping the frequency up and down. At 300 K, aside from a weak resistance change during the sweep up at 0 dB attenuation, hardly any frequency dependence can be seen. Only a constant drift in the DC resistance was recorded. By cooling the probe down to liquid nitrogen temperature, the situation changed significantly. A weak but reproducible frequency dependence appeared and the effect clearly decreased with power attenuation. Interestingly, we note that the variation in resistance has a frequency dependence somewhat similar to the one of S₂₁ (Fig. 6.7), suggesting a relation between the microwave transmission and the DC resistance.

As far as we are aware, no such frequency-dependent DC-resistance effect has been reported thus far. Preliminary inspection of this effect seems to point toward a dielectric heating, which is known to dominate when $\sigma \ll \omega \epsilon$. In the GHz frequency range, this condition is easily met considering $\epsilon_{graphene} \approx 2.4$ [126] and $\sigma = 1/R_S \approx 1$ mS. In this microwave heating picture, the microwave power irradiating graphene would lead to an increase of temperature ΔT in graphene. From Fig. 6.10a and previous measurements on Hall bar, we know that our CVD-graphene has a negative resistance temperature coefficient. Therefore, a microwave-induced temperature increase would result in a decrease in resistance, which is consistent with our observations.

To further support the microwave-heating interpretation, we investigated the microwave-power dependence of the DC resistance. Fig. 6.9b shows the 2T resistance between the microwave tips as a function of frequency at 77 K for small values of power attenuation. One striking feature of these curves is that they all display the same fluctuations and saturate around the same resistance value R_0 . This is consistent with our previous observation that graphene couples better with lower frequencies than higher ones. The reproducible fluctuations in resistance are most likely due to variations in the transmitted power S_{21} , which lead to temperature variations ΔT in

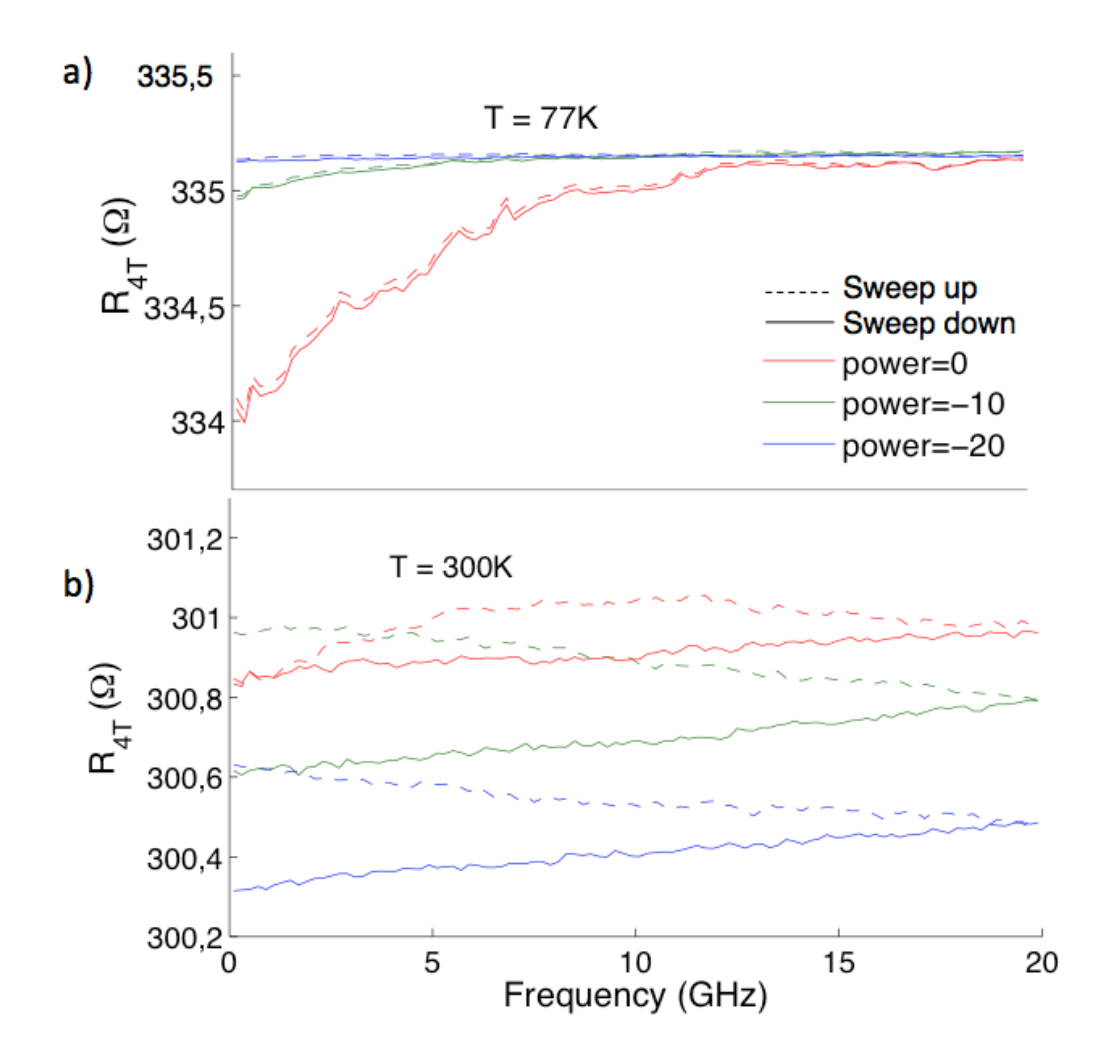


Figure 6.9: Frequency dependence of the 4T DC resistance of graphene at 300 K (a) and 77 K (b) and for different power attenuations. The measurements were performed by sweeping the frequency up (dotted lines) and down (solid lines).

graphene.

In Fig. 6.9c, we emphasized the relation between the microwave power at f=1 GHz and the relative resistance change. The values on the x axis correspond to the power input by the VNA: $P[mW]=10^{P[dB]/20}$. The relation between the microwave power and the resistance change combined with the temperature dependence of the DC resistance provide strong indications that microwave heating is occurring in graphene. The frequency-dependence of this heating effect is also consistent with our previous analysis of the high-frequency transmission through graphene.

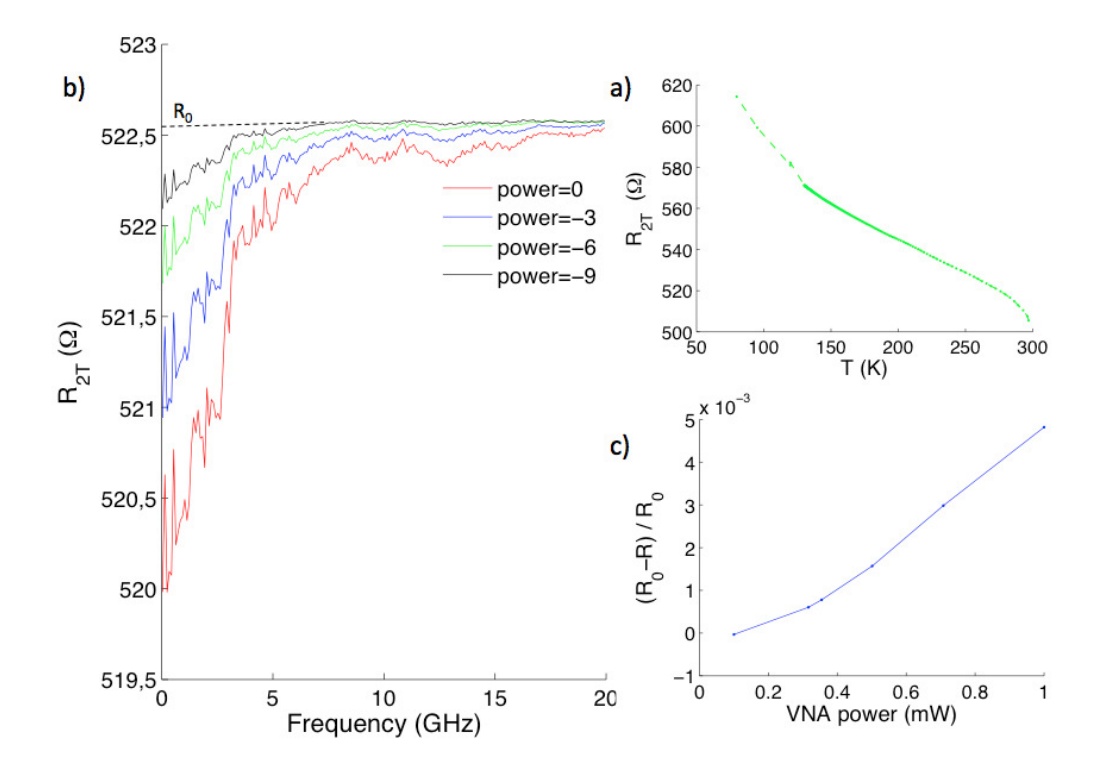


Figure 6.10: Microwave heating of graphene. a) Temperature dependence of the 2T resistance measured between 77 and 300 K. b) Frequency dependence of the 2T resistance at 77 K for small values of power attenuations. All curves saturate around R_0 at high frequency. c) Relative resistance change as a function of the power input by the VNA at 1 GHz.

6.2.3 Effect of Magnetic Field at Low Temperature

The preceding investigation of our high-frequency device indicates that we can apply and couple microwaves to graphene for frequencies ranging from 0.04 to ~5 GHz. However, within that frequency window, measurements at 300 and 77 K have only revealed weak common effects such as microwave heating and microwave scattering from impedance mismatching. In order to explore new possible phenomena such as EMPs, we introduced a sample (CPW3) in the dilution refrigerator. The microwave probe we employed for this purpose consisted of long coaxial cables guiding the microwave signal to a sample holder suspended next to the mixing chamber [123].

The microwave sample was cooled to 100 mK and microwave characterization yielded results very similar to those reported above, i.e. microwave scattering and heating at low frequency (see Fig. 6.11a). This weak temperature dependence of the

high frequency response was also reported by Liu et al. [120] who measured graphene impedance down to liquid helium temperature. Since there is no experimental study that investigated the effect of a magnetic field on the AC impedance, we explored this avenue by sweeping the magnetic field back and forth between -2 and 2 T while measuring the transmission spectrum. As one can see in Fig. 6.11b, the B-field does not seem to have any reproducible effect on the transmission spectrum since the variations in transmission are not consistent with the change in B-field (note that the range of the color bar goes from -2 to -2 T). We believe these variations are simply due to the warming up of the sample. In fact, only a B-field dependence for the DC resistance was measured, and in Chapter 5 we ascribed this dependence to weak localization (Fig. 5.6, large-scale sample).

In many regards, the absence of non-linear phenomena such as EMP can be justified and was, to some extent, predictable. Indeed, looking back at Fig. 2.5, we see that even with a large centimeter-size graphene sample, the EMP frequency only reaches the GHz range for charge carrier density n smaller than 10^{15} m⁻². In Chapter 5, we measured residual charge density which was at least one order of magnitude larger, so even at the Dirac point, the required charge density would not be attained. Furthermore, as we explained in Chapter 2, EMP vanishes unless the magnetic field is strong enough to achieve $\rho_{XY} \gg \rho_{XX}$ and based on the Drude model of conductivity this can be achieved when $\mu \gg B^{-1}$. Since the highest B-field we can apply with our setup is 9 T, the charge carrier mobility should be much larger than 1111 cm²/Vs to expect any EMPs to propagate along the edge of our sample. Based on the mobility values extracted for the hall bar samples, this requirement is far from being met. Low charge density and high mobility graphene samples could likely be obtained with an appropriate post-annealing (cleaning) process, as suggested by some recent papers [58]. More experimental work is needed to develop such cleaning processes.

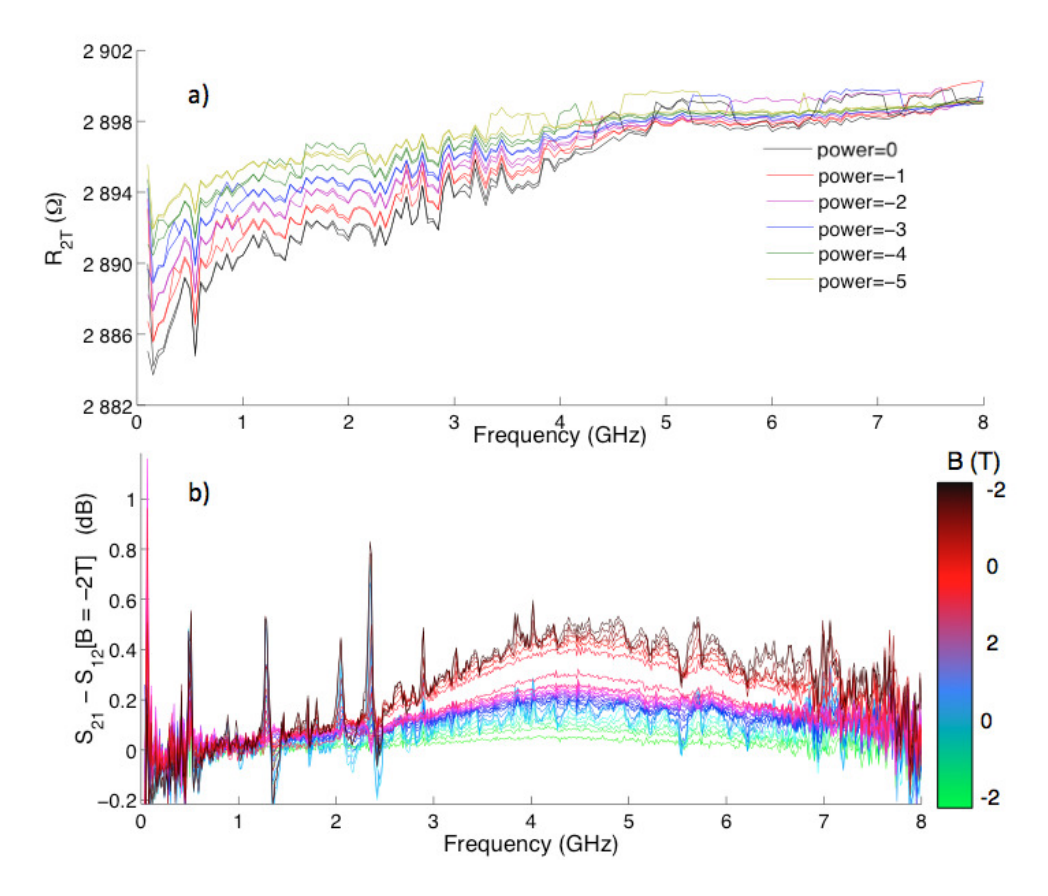


Figure 6.11: Microwave measurements at 100 mK. a) Frequency dependence of the 2T resistance for small values of power attenuations. b) Transmission spectrum at various value of B-field (see color bar). The transmission spectrum at B=-2 T was subtracted to emphasize the possible effect of B. Note that the range of the color bar goes from -2 to -2 T.

Conclusion

From the growth mechanism to the high frequency response, this thesis provides a comprehensive study of graphene grown by chemical vapour deposition and represents an important effort towards improving its electronic properties. The investigation of various growth parameters, in light of thermodynamic and kinetic models, procured a qualitative understanding of the CVD growth of graphene. We showed that growth at low methane on hydrogen ratios ($\chi \sim 0.7$) resulted in graphene of high quality, with low bilayer density and large grain size. We argued that using a copper enclosure considerably lowered this ratio and modified the growth kinetic, thus resulting in large dendritic graphene flakes with fractal dimension d \sim 1.77 that we named graphlocons. Our endeavors to improve the transfer of graphene from copper onto an insulating substrate with PMMA led to an optimized process which was employed to transfer graphlocons and centimeter-sized graphene. The quality of these samples was assessed using Raman spectroscopy, spectrophotometry and TEM imaging. The latter technique showed clear evidence of PMMA and Cu residues on the graphene film.

We developed new microfabrication processes for making graphlocon transistors and graphene Hall bars with a yield of $\sim 30\%$. Using a dilution refrigerator, we measured the electrical field effect in these devices down to 100 mK and based on two models, we extracted mobility values μ ranging from 30 to 460 cm²/Vs and a residual charge carrier density n_0 of $(1.6\pm0.5)\times10^{12}$ cm⁻². Measurement of the Hall resistance corroborated these values and showed no sign of quantum hall effect. Furthermore, we observed a very large negative magnetoresistance that the leading theory on weak localization failed to describe. All these electronic transport measurements indicate

82 **7** Conclusion

the presence of high disorder in our graphene devices which we attribute to transfer and fabrication process contamination.

High frequency measurements were performed at 77 and 300 K with a 4-K microwave probe designed specifically for large graphene samples. A CPW sample geometry allowed the coupling of the high frequency signal with graphene for frequencies up to 5 GHz. A frequency-dependent DC resistance was measured in this frequency range and we attributed this effect to microwave heating. High frequency measurements performed at 100 mK in a dilution refrigerator exhibited very similar effects and no B-field dependence was found. The absence of non-linear phenomena such as EMP was attributed to the low mobility and high density of the charge carriers, as indicated by our transport measurements.

Future work should therefore focus on 1) improving the cleanliness of the transfer and fabrication process and 2) developing post-annealing treatments to improve the electronic properties of the graphene device. A very recent work indicates that with such cleaning methods, CVD graphene mobility can match up to the one of typical exfoliated samples [58]. High-mobility large-scale graphene holds great promise for the observation of EMPs in the GHz range. Even more so, it would represent a major step towards the commercialization of scalable graphene-based high-frequency devices, and towards what might become the Age of carbon.

- [1] M. S. Dresselhaus and P. T. Araujo, "Perspectives on the 2010 Nobel Prize in physics for graphene.," *ACS nano*, vol. 4, pp. 6297–302, Nov. 2010.
- [2] P. Wallace, "The Band Theory of Graphite," Physical Review, vol. 329, 1947.
- [3] H.-P. Boehm, R. Setton, and E. Stumpp, "International union of pure and solid state chemistry. Nomenclature and terminology of graphite," vol. 66, no. 9, pp. 1893–1901, 1994.
- [4] N. D. Mermin, "DECEMBER 1968 Crystalline Order," vol. 176, no. 1, 1968.
- [5] A. K. Geim and K. S. Novoselov, "The rise of graphene.," *Nature materials*, vol. 6, pp. 183–91, Mar. 2007.
- [6] K. S. Novoselov, a. K. Geim, S. V. Morozov, D. Jiang, Y. Zhang, S. V. Dubonos, I. V. Grigorieva, and a. a. Firsov, "Electric field effect in atomically thin carbon films.," *Science (New York, N.Y.)*, vol. 306, pp. 666–9, Oct. 2004.
- [7] K. S. Novoselov, a. K. Geim, S. V. Morozov, D. Jiang, M. I. Katsnelson, I. V. Grigorieva, S. V. Dubonos, and a. a. Firsov, "Two-dimensional gas of massless Dirac fermions in graphene.," *Nature*, vol. 438, pp. 197–200, Nov. 2005.
- [8] K. Bolotin, K. Sikes, Z. Jiang, M. Klima, G. Fudenberg, J. Hone, P. Kim, and H. Stormer, "Ultrahigh electron mobility in suspended graphene," *Solid State Communications*, vol. 146, pp. 351–355, June 2008.
- [9] X. Du, I. Skachko, A. Barker, and E. Y. Andrei, "Approaching ballistic transport in suspended graphene.," *Nature nanotechnology*, vol. 3, pp. 491–5, Aug. 2008.

[10] J.-H. Chen, C. Jang, S. Xiao, M. Ishigami, and M. S. Fuhrer, "Intrinsic and extrinsic performance limits of graphene devices on SiO2.," *Nature nanotech*nology, vol. 3, pp. 206–9, Apr. 2008.

- [11] A. Balandin, S. Ghosh, W. Bao, I. Calizo, D. Teweldebrhan, F. Miao, and C. N. Lau, "Superior thermal conductivity of single-layer graphene.," *Nano letters*, vol. 8, pp. 902–7, Mar. 2008.
- [12] R. R. Nair, P. Blake, A. N. Grigorenko, K. S. Novoselov, T. J. Booth, T. Stauber, N. M. R. Peres, and A. K. Geim, "Fine Structure Constant Defines," vol. 320, no. June, p. 2008, 2008.
- [13] C. Lee, X. Wei, J. W. Kysar, and J. Hone, "Measurement of the elastic properties and intrinsic strength of monolayer graphene.," *Science (New York, N.Y.)*, vol. 321, pp. 385–8, July 2008.
- [14] Y. Lin, C. Dimitrakopoulos, K. Jenkins, and D. Farmer, "100-GHz Transistors from wafer-scale epitaxial graphene," *Science*, p. 100, 2010.
- [15] L. Liao, Y.-C. Lin, M. Bao, R. Cheng, J. Bai, Y. Liu, Y. Qu, K. L. Wang, Y. Huang, and X. Duan, "High-speed graphene transistors with a self-aligned nanowire gate.," *Nature*, vol. 467, pp. 305–8, Sept. 2010.
- [16] F. Schwierz, "Graphene transistors.," *Nature nanotechnology*, vol. 5, pp. 487–96, July 2010.
- [17] I. Meric, M. Y. Han, A. F. Young, B. Ozyilmaz, P. Kim, and K. L. Shepard, "Current saturation in zero-bandgap, top-gated graphene field-effect transistors.," *Nature nanotechnology*, vol. 3, pp. 654–9, Nov. 2008.
- [18] H. Wang, D. Nezich, J. Kong, and T. Palacios, "Graphene Frequency Multipliers," vol. 30, no. 5, pp. 547–549, 2009.
- [19] T. Mueller, F. Xia, and P. Avouris, "Graphene photodetectors for high-speed optical communications," vol. 4, no. March, pp. 297–301, 2010.

[20] F. Xia, T. Mueller, Y.-M. Lin, A. Valdes-Garcia, and P. Avouris, "Ultrafast graphene photodetector.," *Nature nanotechnology*, vol. 4, pp. 839–43, Dec. 2009.

- [21] F. Bonaccorso, Z. Sun, T. Hasan, and A. C. Ferrari, "Graphene photonics and optoelectronics," *Nature Photonics*, vol. 4, pp. 611–622, Aug. 2010.
- [22] S. Bae, H. Kim, Y. Lee, X. Xu, J.-S. Park, Y. Zheng, J. Balakrishnan, T. Lei, H. R. Kim, Y. I. Song, Y.-J. Kim, K. S. Kim, B. Ozyilmaz, J.-H. Ahn, B. H. Hong, and S. Iijima, "Roll-to-roll production of 30-inch graphene films for transparent electrodes.," *Nature nanotechnology*, vol. 5, pp. 574–8, Aug. 2010.
- [23] F. Schedin, A. K. Geim, S. V. Morozov, E. W. Hill, P. Blake, M. I. Katsnelson, and K. S. Novoselov, "Detection of individual gas molecules adsorbed on graphene.," *Nature materials*, vol. 6, pp. 652–5, Sept. 2007.
- [24] Y. Liu, X. Dong, and P. Chen, "Biological and chemical sensors based on graphene materials.," *Chemical Society reviews*, vol. 41, pp. 2283–307, Mar. 2012.
- [25] C. Berger, Z. Song, T. Li, X. Li, A. Y. Ogbazghi, R. Feng, Z. Dai, A. N. Marchenkov, E. H. Conrad, P. N. First, and W. A. De Heer, "Ultrathin epitaxial graphite: 2D electron gas properties and a route toward graphene-based nanoelectronics," *The Journal of Physical Chemistry B*, vol. 108, no. 52, p. 5, 2004.
- [26] K. V. Emtsev, A. Bostwick, K. Horn, J. Jobst, G. L. Kellogg, L. Ley, J. L. McChesney, T. Ohta, S. A. Reshanov, J. Röhrl, E. Rotenberg, A. K. Schmid, D. Waldmann, H. B. Weber, and T. Seyller, "Towards wafer-size graphene layers by atmospheric pressure graphitization of silicon carbide.," *Nature materials*, vol. 8, pp. 203–7, Mar. 2009.
- [27] D. A. Dikin, S. Stankovich, E. J. Zimney, R. D. Piner, G. H. B. Dommett, G. Evmenenko, S. T. Nguyen, and R. S. Ruoff, "Preparation and characterization of graphene oxide paper.," *Nature*, vol. 448, pp. 457–60, July 2007.

[28] S. Stankovich, D. A. Dikin, R. D. Piner, K. A. Kohlhaas, A. Kleinhammes, Y. Jia, Y. Wu, S. T. Nguyen, and R. S. Ruoff, "Synthesis of graphene-based nanosheets via chemical reduction of exfoliated graphite oxide," *Carbon*, vol. 45, pp. 1558–1565, June 2007.

- [29] K. S. Kim, Y. Zhao, H. Jang, S. Y. Lee, J. M. Kim, K. S. Kim, J.-H. Ahn, P. Kim, J.-Y. Choi, and B. H. Hong, "Large-scale pattern growth of graphene films for stretchable transparent electrodes.," *Nature*, vol. 457, pp. 706–10, Feb. 2009.
- [30] X. Li, W. Cai, J. An, S. Kim, J. Nah, D. Yang, R. Piner, A. Velamakanni, I. Jung, E. Tutuc, S. K. Banerjee, L. Colombo, and R. S. Ruoff, "Large-area synthesis of high-quality and uniform graphene films on copper foils.," *Science (New York, N.Y.)*, vol. 324, pp. 1312–4, June 2009.
- [31] X. Li, C. W. Magnuson, A. Venugopal, J. An, J. W. Suk, B. Han, M. Borysiak, W. Cai, A. Velamakanni, Y. Zhu, L. Fu, E. M. Vogel, E. Voelkl, L. Colombo, and R. S. Ruoff, "Graphene films with large domain size by a two-step chemical vapor deposition process.," *Nano letters*, vol. 10, pp. 4328–34, Nov. 2010.
- [32] C. Mattevi, H. Kim, and M. Chhowalla, "A review of chemical vapour deposition of graphene on copper," *Journal of Materials Chemistry*, vol. 21, no. 10, p. 3324, 2011.
- [33] A. Reina, X. Jia, J. Ho, D. Nezich, H. Son, V. Bulovic, M. S. Dresselhaus, and J. Kong, "Large area, few-layer graphene films on arbitrary substrates by chemical vapor deposition.," *Nano letters*, vol. 9, pp. 30–5, Jan. 2009.
- [34] P. W. Sutter, J.-I. Flege, and E. a. Sutter, "Epitaxial graphene on ruthenium.," Nature materials, vol. 7, pp. 406–11, May 2008.
- [35] P. Sutter, J. T. Sadowski, and E. Sutter, "Graphene on Pt(111): Growth and substrate interaction," *Physical Review B*, vol. 80, pp. 1–10, Dec. 2009.

[36] A. T N'Diaye, M. Engler, C. Busse, D. Wall, N. Buckanie, F.-J. Meyer zu Heringdorf, R. van Gastel, B. Poelsema, and T. Michely, "Growth of graphene on Ir(111)," *New Journal of Physics*, vol. 11, p. 023006, Feb. 2009.

- [37] D. R. Cooper, B. D'Anjou, N. Ghattamaneni, B. Harack, M. Hilke, A. Horth, N. Majlis, M. Massicotte, L. Vandsburger, E. Whiteway, and V. Yu, "Experimental Review of Graphene," *ISRN Condensed Matter Physics*, vol. 2012, pp. 1– 56, 2012.
- [38] A. H. Castro Neto, N. M. R. Peres, K. S. Novoselov, and A. K. Geim, "The electronic properties of graphene," *Reviews of Modern Physics*, vol. 81, pp. 109– 162, Jan. 2009.
- [39] Y. Zhang, Y.-W. Tan, H. L. Stormer, and P. Kim, "Experimental observation of the quantum Hall effect and Berry's phase in graphene.," *Nature*, vol. 438, pp. 201–4, Nov. 2005.
- [40] S. Das Sarma, S. Adam, E. Hwang, and E. Rossi, "Electronic transport in twodimensional graphene," Reviews of Modern Physics, vol. 83, pp. 407–470, May 2011.
- [41] S. Kim, J. Nah, I. Jo, D. Shahrjerdi, L. Colombo, Z. Yao, E. Tutuc, and S. K. Banerjee, "Realization of a high mobility dual-gated graphene field-effect transistor with Al₂O₃ dielectric," *Applied Physics Letters*, vol. 94, no. 6, p. 062107, 2009.
- [42] V. E. Dorgan, M.-H. Bae, and E. Pop, "Mobility and saturation velocity in graphene on SiO₂," *Applied Physics Letters*, vol. 97, no. 8, p. 082112, 2010.
- [43] F. Giannazzo and V. Raineri, "Transport Properties of Graphene with Nanoscale Lateral Resolution," Probe Microscopy in Nanoscience, pp. 247–285, 2011.

[44] Y. Zhang, V. W. Brar, C. Girit, A. Zettl, and M. F. Crommie, "Origin of spatial charge inhomogeneity in graphene," *Nature Physics*, vol. 5, pp. 722–726, Aug. 2009.

- [45] J.-H. Chen, W. Cullen, C. Jang, M. Fuhrer, and E. Williams, "Defect Scattering in Graphene," *Physical Review Letters*, vol. 102, pp. 1–4, June 2009.
- [46] J.-H. Chen, C. Jang, S. Adam, M. S. Fuhrer, E. D. Williams, and M. Ishigami, "Charged-impurity scattering in graphene," *Nature Physics*, vol. 4, pp. 377–381, Apr. 2008.
- [47] Q. Yu, L. A. Jauregui, W. Wu, R. Colby, J. Tian, Z. Su, H. Cao, Z. Liu, D. Pandey, D. Wei, T. F. Chung, P. Peng, N. P. Guisinger, E. A. Stach, J. Bao, S.-S. Pei, and Y. P. Chen, "Control and characterization of individual grains and grain boundaries in graphene grown by chemical vapour deposition.," *Nature materials*, vol. 10, pp. 443–9, June 2011.
- [48] M. I. Katsnelson and A. K. Geim, "Electron scattering on microscopic corrugations in graphene.," *Philosophical transactions. Series A, Mathematical, physical, and engineering sciences*, vol. 366, pp. 195–204, Jan. 2008.
- [49] K. I. Bolotin, K. J. Sikes, J. Hone, H. L. Stormer, and P. Kim, "Temperature-Dependent Transport in Suspended Graphene," *Physical Review Letters*, vol. 101, pp. 1–4, Aug. 2008.
- [50] S. Adam, E. H. Hwang, V. M. Galitski, and S. Das Sarma, "A self-consistent theory for graphene transport.," Proceedings of the National Academy of Sciences of the United States of America, vol. 104, pp. 18392–7, Nov. 2007.
- [51] Y.-W. Tan, Y. Zhang, K. Bolotin, Y. Zhao, S. Adam, E. H. Hwang, S. Das Sarma, H. L. Stormer, and P. Kim, "Measurement of Scattering Rate and Minimum Conductivity in Graphene," *Physical Review Letters*, vol. 99, pp. 10–13, Dec. 2007.

[52] C. R. Dean, a. F. Young, I. Meric, C. Lee, L. Wang, S. Sorgenfrei, K. Watanabe, T. Taniguchi, P. Kim, K. L. Shepard, and J. Hone, "Boron nitride substrates for high-quality graphene electronics.," *Nature nanotechnology*, vol. 5, pp. 722–6, Oct. 2010.

- [53] P. Avouris, "Graphene: Electronic and Photonic Properties and Devices.," Nano letters, pp. 4285–4294, Sept. 2010.
- [54] W. Gannett, W. Regan, K. Watanabe, T. Taniguchi, M. F. Crommie, and a. Zettl, "Boron nitride substrates for high mobility chemical vapor deposited graphene," *Applied Physics Letters*, vol. 98, no. 24, p. 242105, 2011.
- [55] O. V. Yazyev and S. G. Louie, "Electronic transport in polycrystalline graphene.," *Nature materials*, vol. 9, pp. 806–9, Oct. 2010.
- [56] Z. Luo, Y. Lu, D. W. Singer, M. E. Berck, L. A. Somers, B. R. Goldsmith, and A. T. C. Johnson, "Effect of Substrate Roughness and Feedstock Concentration on Growth of Wafer-Scale Graphene at Atmospheric Pressure," *Chemistry of Materials*, p. 110210120716054, Feb. 2011.
- [57] Y. Wang, Y. Zheng, X. Xu, E. Dubuisson, Q. Bao, J. Lu, and K. P. Loh, "Electrochemical delamination of CVD-grown graphene film: toward the recyclable use of copper catalyst.," *ACS nano*, vol. 5, pp. 9927–33, Dec. 2011.
- [58] J. Chan, A. Venugopal, A. Pirkle, S. McDonnell, D. Hinojos, C. W. Magnuson, R. S. Ruoff, L. Colombo, R. M. Wallace, and E. M. Vogel, "Reducing extrinsic performance-limiting factors in graphene grown by chemical vapor deposition.," ACS nano, vol. 6, pp. 3224–9, Apr. 2012.
- [59] A. Pirkle, J. Chan, A. Venugopal, D. Hinojos, C. W. Magnuson, S. McDonnell, L. Colombo, E. M. Vogel, R. S. Ruoff, and R. M. Wallace, "The effect of chemical residues on the physical and electrical properties of chemical vapor deposited graphene transferred to SiO₂," *Applied Physics Letters*, vol. 99, no. 12, p. 122108, 2011.

[60] X. Liang, B. A. Sperling, I. Calizo, G. Cheng, C. A. Hacker, Q. Zhang, Y. Obeng, K. Yan, H. Peng, Q. Li, X. Zhu, H. Yuan, A. R. H. Walker, Z. Liu, L.-M. Peng, and C. A. Richter, "Toward clean and crackless transfer of graphene.," ACS nano, vol. 5, pp. 9144–53, Nov. 2011.

- [61] N. W. Ashcroft and D. N. Mermin, *Solid State Physics*. Toronto: Thomson Learning, 1 ed., Jan. 1976.
- [62] E. McCann, K. Kechedzhi, V. I. Falko, H. Suzuura, T. Ando, and B. L. Altshuler, "Weak-Localization Magnetoresistance and Valley Symmetry in Graphene," *Physical Review Letters*, vol. 97, pp. 14–17, Oct. 2006.
- [63] S. A. Mikhailov, "Chapter 1 Edge and inter-edge magnetoplasmons in two-dimensional electron systems," 1985.
- [64] L. Ju, B. Geng, J. Horng, C. Girit, M. Martin, Z. Hao, H. A. Bechtel, X. Liang, A. Zettl, Y. R. Shen, and F. Wang, "Graphene plasmonics for tunable terahertz metamaterials," vol. 6, no. September, pp. 6–10, 2011.
- [65] Z. Fei, O. G. O. Andreev, O. W. Bao, L. M. Zhang, A. S. Mcleod, C. Wang, M. K. Stewart, Z. Zhao, G. Dominguez, M. Thiemens, M. M. Fogler, M. J. Tauber, A. H. Castro-neto, C. N. Lau, F. Keilmann, and D. N. Basov, "Infrared Nanoscopy of Dirac Plasmons at the Graphen/SiO₂ Interface," pp. 4701–4705, 2011.
- [66] J. Chen, M. Badioli, P. Alonso-gonzález, S. Thongrattanasiri, F. Huth, J. Osmond, M. Spasenović, A. Centeno, P. Godignon, A. Zurutuza, N. Camara, J. G. De, R. Hillenbrand, and F. Koppens, "Optical nano-imaging of gate-tuneable graphene plasmons,"
- [67] Z. Fei, A. S. Rodin, G. O. Andreev, W. Bao, A. S. Mcleod, M. Wagner, L. M. Zhang, Z. Zhao, and G. Dominguez, "Gate-tuning of graphene plasmons revealed by infrared nano-imaging,"

[68] H. Yan, Z. Li, X. Li, W. Zhu, and P. Avouris, "Magnetic field tuning of terahertz Dirac plasmons in graphene," 2012.

- [69] I. Crassee, M. Orlita, M. Potemski, a. L. Walter, M. Ostler, T. Seyller, I. Gaponenko, J. Chen, and a. B. Kuzmenko, "Intrinsic Terahertz Plasmons and Magnetoplasmons in Large Scale Monolayer Graphene.," Nano letters, Apr. 2012.
- [70] N. Kumada, S. Tanabe, H. Hibino, H. Kamata, K. Muraki, and T. Fujisawa, "Plasmon transport in graphene investigated by time-resolved measurement," pp. 2–12.
- [71] A. K. Geim, "Graphene: status and prospects.," *Science (New York, N.Y.)*, vol. 324, pp. 1530–4, June 2009.
- [72] A. Reina, X. Jia, J. Ho, D. Nezich, H. Son, V. Bulovic, M. S. Dresselhaus, and J. Kong, "Large area, few-layer graphene films on arbitrary substrates by chemical vapor deposition.," *Nano letters*, vol. 9, pp. 30–5, Jan. 2009.
- [73] A. T N'Diaye, M. Engler, C. Busse, D. Wall, N. Buckanie, F.-J. Meyer zu Heringdorf, R. van Gastel, B. Poelsema, and T. Michely, "Growth of graphene on Ir(111)," New Journal of Physics, vol. 11, p. 023006, Feb. 2009.
- [74] P. Sutter, J. T. Sadowski, and E. Sutter, "Graphene on Pt(111): Growth and substrate interaction," *Physical Review B*, vol. 80, Dec. 2009.
- [75] S. Kumar, N. McEvoy, T. Lutz, G. P. Keeley, V. Nicolosi, C. P. Murray, W. J. Blau, and G. S. Duesberg, "Gas phase controlled deposition of high quality large-area graphene films.," *Chemical communications (Cambridge, England)*, vol. 46, pp. 1422–4, Mar. 2010.
- [76] W. Wu, L. a. Jauregui, Z. Su, Z. Liu, J. Bao, Y. P. Chen, and Q. Yu, "Growth of single crystal graphene arrays by locally controlling nucleation on polycrystalline Cu using chemical vapor deposition.," *Advanced materials (Deerfield Beach, Fla.)*, vol. 23, pp. 4898–903, Nov. 2011.

[77] Z. Sun, Z. Yan, J. Yao, E. Beitler, Y. Zhu, and J. M. Tour, "Growth of graphene from solid carbon sources.," *Nature*, vol. 468, pp. 549–52, Nov. 2010.

- [78] G. Ruan, Z. Sun, Z. Peng, and J. M. Tour, "Growth of graphene from food, insects, and waste.," ACS nano, vol. 5, pp. 7601–7, Sept. 2011.
- [79] G. Cao, Nanostructures & Nanomaterials: Synthesis, Properties & Applications. Imperial College Press, 2004.
- [80] G. López and E. Mittemeijer, "The solubility of C in solid Cu," *Scripta Materialia*, vol. 51, pp. 1–5, July 2004.
- [81] X. Li, W. Cai, L. Colombo, and R. S. Ruoff, "Evolution of graphene growth on Ni and Cu by carbon isotope labeling.," *Nano letters*, vol. 9, pp. 4268–72, Dec. 2009.
- [82] J.-H. Park and T. S. Sudarshan, *Chemical vapor deposition*. Materials Park, Ohio: ASM International, 2001.
- [83] W. Zhang, P. Wu, Z. Li, and J. Yang, "First-Principles Thermodynamics of Graphene Growth on Cu Surfaces," *The Journal of Physical Chemistry C*, vol. 115, pp. 17782–17787, Sept. 2011.
- [84] S. Bhaviripudi, X. Jia, M. S. Dresselhaus, and J. Kong, "Role of kinetic factors in chemical vapor deposition synthesis of uniform large area graphene using copper catalyst.," *Nano letters*, vol. 10, pp. 4128–33, Oct. 2010.
- [85] I. Vlassiouk, M. Regmi, P. Fulvio, S. Dai, P. Datskos, G. Eres, and S. Smirnov, "Role of hydrogen in chemical vapor deposition growth of large single-crystal graphene," *ACS Nano*, vol. 5, no. 7, pp. 6069–6076, 2011.
- [86] H. Aspinall, M. E. Pemble, W. L. Gladfelter, B. Leese, R. A. Fischer, H. Parala,
 R. Kanjolia, R. D. Dupuis, S. E. Alexandrov, S. J. C. Irvine, R. Palgrave,
 I. P. Parkin, M. Ritala, J. Niinisto, S. Krumdieck, and P. Chalker, *Chemical*

Vapour Deposition: Precursors, Processes and Applications. The Royal Society of Chemistry, 2009.

- [87] V. Yu, "Optics and Chemical Vapour Deposition of Graphene Monolayers on Various Substrates," 2010.
- [88] L. Fan, Z. Li, Z. Xu, K. Wang, J. Wei, X. Li, J. Zou, D. Wu, and H. Zhu, "Step driven competitive epitaxial and self-limited growth of graphene on copper surface," AIP Advances, vol. 1, no. 3, p. 032145, 2011.
- [89] M. Regmi, M. F. Chisholm, and G. Eres, "The effect of growth parameters on the intrinsic properties of large-area single layer graphene grown by chemical vapor deposition on Cu," *Carbon*, vol. 50, pp. 134–141, Jan. 2012.
- [90] S. Nie, W. Wu, S. Xing, Q. Yu, J. Bao, S. Pei, and F. Kevin, "Growth from Below: Bilayer Graphene on Copper by Chemical Vapor Deposition," pp. 1–14.
- [91] Y. Zhang, Z. Li, P. Kim, L. Zhang, and C. Zhou, "Anisotropic Hydrogen Etching of Chemical Vapor Deposited Graphene," ACS Nano, vol. 6, pp. 126–132, Jan. 2012.
- [92] H. Wang, G. Wang, P. Bao, S. Yang, W. Zhu, X. Xie, and W.-J. Zhang, "Controllable Synthesis of Submillimeter Single-Crystal Monolayer Graphene Domains on Copper Foils by Suppressing Nucleation," *Journal of the American Chemical Society*, vol. 134, pp. 3627–3630, Feb. 2012.
- [93] G. H. Han, F. Güne, J. J. Bae, E. S. Kim, S. J. Chae, H.-J. Shin, J.-Y. Choi, D. Pribat, and Y. H. Lee, "Influence of Copper Morphology in Forming Nucleation Seeds for Graphene Growth," *Nano Letters*, vol. 11, pp. 4144–4148, Oct. 2011.
- [94] J. Gao, J. Yip, J. Zhao, B. I. Yakobson, and F. Ding, "Graphene Nucleation on Transition Metal Surface: Structure Transformation and Role of the Metal

Step Edge," Journal of the American Chemical Society, vol. 133, pp. 5009–5015, Apr. 2011.

- [95] X. Li, C. W. Magnuson, A. Venugopal, R. M. Tromp, J. B. Hannon, E. M. Vogel, L. Colombo, and R. S. Ruoff, "Large-area graphene single crystals grown by low-pressure chemical vapor deposition of methane on copper.," *Journal of the American Chemical Society*, vol. 133, no. 9, pp. 2816–9, 2011.
- [96] J. Y. Huang, F. Ding, B. I. Yakobson, P. Lu, L. Qi, and J. Li, "In situ observation of graphene sublimation and multi-layer edge reconstructions.," *Proceedings* of the National Academy of Sciences of the United States of America, vol. 106, no. 25, pp. 10103–10108, 2009.
- [97] P. Meakin, Fractals, scaling and growth far from equilibrium. Cambridge University Press, 1998.
- [98] P. Blake, E. W. Hill, A. H. Castro Neto, K. S. Novoselov, D. Jiang, R. Yang, T. J. Booth, and A. K. Geim, "Making graphene visible," Applied Physics Letters, vol. 91, no. 6, p. 063124, 2007.
- [99] X. Li, Y. Zhu, W. Cai, M. Borysiak, B. Han, D. Chen, R. D. Piner, L. Colombo, and R. S. Ruoff, "Transfer of large-area graphene films for high-performance transparent conductive electrodes.," *Nano letters*, vol. 9, pp. 4359–63, Dec. 2009.
- [100] W. Regan, N. Alem, B. Aleman, B. Geng, C. Girit, L. Maserati, F. Wang, M. Crommie, and A. Zettl, "A direct transfer of layer-area graphene," Applied Physics Letters, vol. 96, no. 11, p. 113102, 2010.
- [101] A. C. Ferrari, J. C. Meyer, V. Scardaci, C. Casiraghi, M. Lazzeri, F. Mauri, S. Piscanec, D. Jiang, K. S. Novoselov, S. Roth, and A. K. Geim, "Raman Spectrum of Graphene and Graphene Layers," *Physical Review Letters*, vol. 97, pp. 1–4, Oct. 2006.

[102] L. Malard, M. Pimenta, G. Dresselhaus, and M. Dresselhaus, "Raman spectroscopy in graphene," *Physics Reports*, vol. 473, pp. 51–87, Apr. 2009.

- [103] S. Bernard, E. Whiteway, V. Yu, D. G. Austing, and M. Hilke, "Experimental Phonon Band Structure of Graphene using C 12 and C 13 Isotopes," vol. 8, 2011.
- [104] L. Yang, J. Deslippe, C.-H. Park, M. Cohen, and S. Louie, "Excitonic Effects on the Optical Response of Graphene and Bilayer Graphene," *Physical Review Letters*, vol. 103, pp. 1–4, Oct. 2009.
- [105] C. Lee, J. Y. Kim, S. Bae, K. S. Kim, B. H. Hong, and E. J. Choi, "Optical response of large scale single layer graphene," *Applied Physics Letters*, vol. 98, no. 7, p. 071905, 2011.
- [106] Y.-C. Lin, C.-C. Lu, C.-H. Yeh, C. Jin, K. Suenaga, and P.-W. Chiu, "Graphene annealing: how clean can it be?," *Nano letters*, vol. 12, pp. 414–9, Jan. 2012.
- [107] G. Giovannetti, P. Khomyakov, G. Brocks, V. Karpan, J. van den Brink, and P. Kelly, "Doping Graphene with Metal Contacts," *Physical Review Letters*, vol. 101, pp. 4–7, July 2008.
- [108] F. Xia, V. Perebeinos, Y.-m. Lin, Y. Wu, and P. Avouris, "The origins and limits of metal-graphene junction resistance.," *Nature nanotechnology*, vol. 6, pp. 179–84, Mar. 2011.
- [109] Y. Ye, L. Gan, L. Dai, Y. Dai, X. Guo, H. Meng, B. Yu, Z. Shi, K. Shang, and G. Qin, "A simple and scalable graphene patterning method and its application in CdSe nanobelt/graphene Schottky junction solar cells.," *Nanoscale*, vol. 3, pp. 1477–81, Apr. 2011.
- [110] G. Kalita, L. Qi, Y. Namba, K. Wakita, and M. Umeno, "Femtosecond laser induced micropatterning of graphene film," *Materials Letters*, vol. 65, pp. 1569– 1572, June 2011.

[111] H. J. Park, J. Meyer, S. Roth, and V. Skákalová, "Growth and properties of few-layer graphene prepared by chemical vapor deposition," *Carbon*, vol. 48, pp. 1088–1094, Apr. 2010.

- [112] J. Moser, H. Tao, S. Roche, F. Alzina, C. M. Sotomayor Torres, and A. Bachtold, "Magnetotransport in disordered graphene exposed to ozone: From weak to strong localization," *Physical Review B*, vol. 81, pp. 2–7, May 2010.
- [113] X. Hong, S.-H. Cheng, C. Herding, and J. Zhu, "Colossal negative magnetoresistance in dilute fluorinated graphene," *Physical Review B*, vol. 83, Feb. 2011.
- [114] E. Whiteway, V. Yu, J. Lefebvre, R. Gagnon, and M. Hilke, "Magneto-transport of large CVD-grown graphene," vol. 8, 2010.
- [115] S. Datta, Electronic Transport in Mesoscopic Systems (Cambridge Studies in Semiconductor Physics and Microelectronic Engineering). Cambridge University Press, May 1997.
- [116] M. Dragoman, D. Dragoman, F. Coccetti, R. Plana, and A. A. Muller, "Microwave switches based on graphene," *Journal of Applied Physics*, vol. 105, no. 5, p. 054309, 2009.
- [117] H. Wang, S. Member, A. Hsu, J. Wu, J. Kong, and T. Palacios, "Graphene-Based Ambipolar RF Mixers," vol. 31, no. 9, pp. 906–908, 2010.
- [118] G. Deligeorgis, M. Dragoman, D. Neculoiu, D. Dragoman, G. Konstantinidis, A. Cismaru, and R. Plana, "Microwave propagation in graphene," Applied Physics Letters, vol. 95, no. 7, p. 073107, 2009.
- [119] P. Jiang, A. F. Young, W. Chang, P. Kim, L. W. Engel, and D. C. Tsui, "Quantum oscillations observed in graphene at microwave frequencies," *Applied Physics Letters*, vol. 97, no. 6, p. 062113, 2010.
- [120] W. Liu, R. V. Aguilar, Y. Hao, R. S. Ruoff, and N. P. Armitage, "Broadband microwave and time-domain terahertz spectroscopy of CVD grown graphene,"

Physics, vol. 21, no. Copyright (C) 2011 American Chemical Society (ACS). All Rights Reserved., p. 5, 2011.

- [121] H. S. Skulason, H. V. Nguyen, A. Guermoune, V. Sridharan, M. Siaj, C. Caloz, and T. Szkopek, "110 GHz measurement of large-area graphene integrated in low-loss microwave structures," *Applied Physics Letters*, vol. 99, no. 15, p. 153504, 2011.
- [122] M. A. Zudov and R. R. Du, "Shubnikovde Haas-like oscillations in millimeterwave photoconductivity in a high-mobility two-dimensional electron gas," *Physical Review B*, vol. 64, pp. 3–6, Oct. 2001.
- [123] A. Armstrong-Brown, Sub-nanosecond dynamics in low-dimensional systems, vol. 31. 2007.
- [124] P. L. Levesque, S. S. Sabri, C. M. Aguirre, J. Guillemette, M. Siaj, P. Desjardins, T. Szkopek, and R. Martel, "Probing charge transfer at surfaces using graphene transistors.," *Nano letters*, vol. 11, pp. 132–7, Jan. 2011.
- [125] L. Chen, C. Ong, C. Neo, V. Varadan, and V. Varadan, Microwave Electronics: Measurement and Materials Characterization. John Wiley and Sons, 2004.
- [126] M. C. Lemme, S. Member, T. J. Echtermeyer, M. Baus, and H. Kurz, "A Graphene Field-Effect Device," vol. 28, no. 4, pp. 282–284, 2007.